UNIVERSITY OF CALIFORNIA, SAN DIEGO

Photon Pairs from a Silicon Photonic Chip

A dissertation submitted in partial satisfaction of the
requirements for the degree
Doctor of Philosophy

in

Electrical Engineering (Photonics)

by

Ranjeet Kumar

Committee in charge:

Shayan Mookherjea, Chair
Julio T. Barreiro
Dimitri N. Basov
Joseph E. Ford
George Papen
Kartik Srinivasan

2016

The dissertation of Ranjeet Kumar is approved, and it is acceptable in quality and form for publication on microfilm and electronically:

_____

_____

_____

_____

_____

_____

Chair

University of California, San Diego

2016

EPIGRAPH

Those who are not shocked when they first come across quantum theory cannot possibly have understood it.

- Niels Bohr

TABLE OF CONTENTS

LIST OF FIGURES

LIST OF TABLES

ACKNOWLEDGEMENTS

First and foremost, I would like to thank my advisor, Prof. Shayan Mookherjea, who has been a constant source of inspiration for me. He is not only a very talented researcher but also a good teacher. He has always motivated me to think outside the box and look at the bigger picture. His passion for research has helped me to become a better researcher. Over the past few years, I received various helps and excellent advice from him, and I am thankful for all of them.

I am thankful to my doctoral committee: Prof. Julio Barreiro, Prof. Dimitri Basov, Prof. Joseph Ford, Prof. George Papen, and Dr. Kartik Srinivasan. I took Prof. Papen's Statistical Optics class, and it was one of the best class I took at UC San Diego. I am thankful for the opportunity to collaborate with Dr. Srinivasan. His help in setting-up the quantum photonics experiment at UC San Diego was the stepping stone for my PhD research work. I am grateful to Dr. Jun Rong Ong for device design, and Dr. Xianshu Luo and Dr. Guo-Qiang Patrick Lo (A*STAR – IME) for device fabrication.

For the past few years, I have been a part of MNP group and it gave me opportunities to interact and work with some very smart people, and that includes Dr. Jun Rong Ong, Dr. Ryan Aguinaldo, Dr. Marc Savanier, Mr. Peter Weigel, Ms. Hannah Grant, Mr. John Rechio, Mr. Craig Ives and Mr. Josh Wang. Jun Rong graciously shared his experimental setup with me, and helped me in setting-up the quantum experiment in our lab. Jun Rong was my constant companion in the lab from 2012–2014, and Marc has been since 2013. Marc was instrumental in the characterization of single microring resonators for photon pair generation. I am thankful to both of them for their insights and help in the lab. I benefited a lot through the scientific debates that I shared with Ryan, and it is indeed the best way to learn a subject. We worked on some of the data-center based measurements/devices together. I did not get a chance to work with Peter and Hannah but we used to have very lively discussions in the office, on topics ranging from science, photonics to food! John helped me with the tunable filters, which was an important part of the setup, and for that I am thankful.

I have had a very fulfilling experience in San Diego, not only on professional

but also on a personal level. I made some very good friends, who kept me going these past few years. I thank them all for their friendship – San Diego has been a home because of them.

Finally, I would like to thank my parents for their unconditional love and support. They taught me the value of hard work. I am here because of them, and I owe my entire accomplishments to them. I am also thankful to my brothers for their love and support.

Ranjeet Kumar
San Diego, CA
February 10, 2016

Chapter 2 contains material published in: Ranjeet Kumar, Jun Rong Ong, John Recchio, Kartik Srinivasan, and Shayan Mookherjea, "Spectrally-multiplexed and tunable-wavelength photon pairs at 1.55 μm from a silicon coupled-resonator optical waveguide" Optics Letters Vol. 38, Iss. 16, pp. 2969–2971 (2013). The dissertation author was the primary author of this paper.

Chapter 3 contains material published in: Ranjeet Kumar, Jun Rong Ong, Marc Savanier, and Shayan Mookherjea, "Controlling the spectrum of photons generated on a silicon nanophotonic chip" Nature Communications Vol. 5, art. 5489 (2014). The dissertation author was the primary author of this paper.

Chapter 4 contains material published in: Ranjeet Kumar, Marc Savanier, Jun Rong Ong, and Shayan Mookherjea, "Entanglement measurement of a coupled silicon microring photon pair source" Optics Express Vol. 23, Iss. 15, pp. 19318–19327 (2015). The dissertation author was the primary author of this paper.

Chapter 5 contains material published in: Marc Savanier, Ranjeet Kumar, and Shayan Mookherjea, "Photon pair generation from compact silicon microring resonators using microwatt-level pump powers" Optics Express Vol. 24, Iss. 4, pp. 3313–3328 (2016). The dissertation author was one of the primary author of this paper.

Chapter 6 contains material published in: Marc Savanier, Ranjeet Kumar, and Shayan Mookherjea, "Optimizing photon-pair generation electronically using a *p-i-n* diode incorporated in a silicon microring resonator" Applied Physics Letters Vol. 107, 131101 (2015). The dissertation author was one of the primary author of this paper.

Appendix A contains material published in: Ranjeet Kumar, Jun Rong Ong, Marc Savanier and Shayan Mookherjea "Controlling the spectrum of photons generated on a silicon nanophotonic chip" Nature Communications Vol. 5, art. 5489 (2014). The dissertation author was the primary author of this paper.

VITA

2005 - 2009	B.Tech., Indian Institute of Technology Delhi, India
2010 - 2012	M.Sc., University of Calgary, Alberta, Canada
2012 - 2016	Ph.D., University of California, San Diego

PUBLICATIONS

M. Savanier, R. Kumar, and S. Mookherjea, "Photon pair generation from compact silicon microring resonators using microwatt-level pump powers" Optics Express Vol. 24, Iss. 4, pp. 3313–3328 (2016).

M. Savanier, R. Kumar, and S. Mookherjea, "Optimizing photon-pair generation electronically using a *p-i-n* diode incorporated in a silicon microring resonator" Applied Physics Letters Vol. 107, 131101 (2015).

R. Kumar, M. Savanier, J. R. Ong, and S. Mookherjea, "Entanglement measurement of a coupled silicon microring photon pair source" Optics Express Vol. 23, Iss. 15, pp. 19318–19327 (2015).

R. Kumar, J. R. Ong, M. Savanier, and S. Mookherjea, "Controlling the spectrum of photons generated on a silicon nanophotonic chip" Nature Communications Vol. 5, art. 5489 (2014).

R. Kumar, J. R. Ong, J. Recchio, K. Srinivasan, and S. Mookherjea, "Spectrally-multiplexed and tunable-wavelength photon pairs at 1.55 μm from a silicon coupled-resonator optical waveguide" Optics Letters Vol. 38, Iss. 16, pp. 2969–2971 (2013).

J. R. Ong, R. Kumar, and S. Mookherjea, "Triply resonant four-wave mixing in silicon-coupled resonator microring waveguides" Optics Letters Vol. 39, Iss. 19, pp. 5653–5656 (2014).

J. R. Ong, R. Kumar, and S. Mookherjea, "Silicon micro-ring based wavelength converter with integrated pump and signal suppression" Optics Letters Vol. 39, Iss. 15, pp. 4439–4441 (2014).

J. R. Ong, R. Kumar, R. Aguinaldo, and S. Mookherjea, "Efficient continuous-wave four-wave mixing in silicon-on-insulator micro-rings with active carrier removal" IEEE Photonics Technology Letters Vol. 25, Iss. 17, pp. 1699–1702 (2013).

J. R. Ong, R. Kumar, and S. Mookherjea, "Ultra-high-contrast and tunable bandwidth filter using cascaded high-order silicon microring filters" IEEE Photonics Technology Letters Vol. 25, Iss. 16, pp. 1543–1546 (2013).

R. Kumar, E. Barrios, C. Kupchak, and A. I. Lvovsky, "Experimental characterization of bosonic creation and annihilation operators" Physical Review Letters Vol. 110, 130403 (2013).

R. Kumar, E. Barrios, A. MacRae, E. Cairns, E. H. Huntington, and A. I. Lvovsky, "Versatile wideband balanced detector for quantum optical homodyne tomography" Optics Communications Vol. 285, Iss. 24, pp. 5259–5267 (2012).

ABSTRACT OF THE DISSERTATION

Photon Pairs from a Silicon Photonic Chip

by

Ranjeet Kumar

Doctor of Philosophy in Electrical Engineering (Photonics)

University of California, San Diego, 2016

Shayan Mookherjea, Chair

Photon pair sources with the capability to tune the wavelength and correlation properties of the generated photons can be useful for quantum applications such as communication, sensing, and computing. Silicon devices based on the SOI (silicon-on-insulator) platform benefits from both tight modal confinement, due to high index contrast between core and cladding, and CMOS compatible manufacturing process, making it a suitable platform for such sources. In the present work, we discuss the possibility of using planar resonant silicon devices with bend radii of a few tens of microns as photon pair sources. We discuss that a silicon nanophotonic chip consisting of either a single microring or coupled microrings can be used to generate photon pairs around 1.55 μm. We discuss that the photons are generated in multiple pairs of wavelengths and can be tuned over several nanometers,

demonstrating the capability to generate wavelength division multiplexed photon pairs at freely chosen telecommunication-band wavelengths. Further on, we discuss the ease of control over the bi-photon spectrum of the generated photon pairs and its implication in controlling their correlation properties. Uncorrelated photon pairs can be used to herald a single photon, and correlated photon pairs can be used in various quantum applications such as communication and sensing. In the end, we discuss the design parameters of a single microring resonator based sources.

Chapter 1

Introduction

There is a growing need for a good source of single photons or photon pairs in the scientific and engineering community for various applications such as quantum computing [1], communication [2] and sensing [3, 4]. All these applications promise enhanced performance compared to their classical counterparts, e.g., quantum communication (quantum key distribution) promises unbreakable secure communication through the laws of quantum mechanics [2, 5]. Classical communication, which ensures security through mathematical complexity, such as RSA encryption, can in principle be broken [6]. Some of the possible applications of quantum key distribution may include secure energy grid controllers, space/satellite control network nodes and UAV portable ground control stations.

Source of Photons

Generation of photons can be classified into two categories: (1) Generation of single photons through *deterministic sources*, and (2) Generation of photon pairs through *probabilistic sources*. Deterministic sources such as Quantum dots [7,8] or Diamond NV centers [9,10] use deterministic processes to generate single photons on-demand. On the contrary, probabilistic sources use non-deterministic processes such as spontaneous parametric-down conversion (SPDC) [11, 12] or spontaneous four-wave mixing (SFWM) [13,14] to generate photon pairs in a probabilistic manner. Due to inherit non-deterministic nature, the exact emission time of photon

pairs are not known, but SPDC/SFWM ensures that the photons are always generated in pairs. This property can be utilized to "herald" a single photon from a pair, and a pair source can effectively be used as a single photon source [15, 16]. Examples include SPDC process in χ^2 non-linear materials such as periodically-poled KTP & $LiNbO_3$, and SFWM process in χ^3 non-linear materials such as glass & silicon.

Photons from pair sources also have the advantage of being non-classically correlated (entangled) under certain conditions. Quantum entanglement is a unique physical phenomenon under which the state of interacting particles cannot be described independently. Entanglement can happen in various degrees of freedom, such as polarization [17], energy-time [18] and orbital angular momentum [19]. Due to *photon-starved* nature of the modern communication systems, we always seek to use more degrees of freedom to encode information than simple on-off keying [20]. Hence, it is useful to maximize the number of bits per photon, and the entanglement based protocols can be useful for higher order encoding processes.

Due to different generation processes, the generated photons are also inherently different in their physical properties. In this dissertation, we are interested in the photon pairs that can be useful for quantum communication over existing optical networks such as ITU-T 100-GHz telecommunication grid [21], which restricts the wavelength of operation to be around 1550 nm.

Though bulk crystals and fiber optics have been the traditional go-to sources, semiconductor-based platforms have recently gained more interest as they can benefit from wafer-scale, low-cost, scalable manufacturing processes, in view of on-chip integration. In particular, the CMOS-compatible SOI (silicon-on-insulator) platform is advantageous because of the high refractive index contrast between silicon core and silica cladding, which increases the mode confinement, increases nonlinearity, and thus reduces the device size [22]. Numerous silicon photonic structures have been demonstrated to generate photon pairs and herald single photon at room temperature [23–31]. Among them the resonant devices such as ring based structures have the advantage to being more compact and power efficient, requiring only a few milliwatts or less of optical pump powers.

Chapter 2

Photon Pair Generation in Silicon

Photon pairs are generated inside silicon devices through spontaneous four-wave mixing via non-linear Kerr interaction [32]. Through this mechanism, two photons from a single optical pump beam at frequency ω_p are absorbed and photon pairs are created at frequency ω_s (signal) and ω_i (idler). Energy conservation requires that $2\omega_p = \omega_s + \omega_i$, and momentum conservation (phase matching) is also necessary for appreciable rate of pair production. The expression for pair generation rate (PGR) in a silicon waveguide can be written as [33]:

$$\mathrm{r} = \Delta\nu \left(\gamma \mathrm{P}_0 \mathrm{L}_{eff}\right)^2 \mathrm{sinc}^2 \left[\beta_2 \left(\Delta\omega\right)^2 \mathrm{L}/2 + \gamma \mathrm{P}_0 \mathrm{L}\right] \mathrm{e}^{-\alpha \mathrm{L}} \tag{2.1}$$

where $\Delta\nu$ is the bandwidth of photon-pair channel, γ is the waveguide non-linear coefficient, P_0 is the input pump power, L is the waveguide length and L_{eff} is the effective length after accounting for the propagation loss α, and $\mathrm{sinc}^2\left[\cdots\right]$ is the phase matching term with β_2 being the group-velocity dispersion coefficient & $\Delta\omega$ being the pump–signal/idler angular frequency separation. γ and L_{eff} in Eq. 2.1 are defined as:

$$\begin{aligned} \gamma &= \frac{2\pi}{\lambda} \frac{n_2}{\mathrm{A}_{eff}} \\ \mathrm{L}_{eff} &= \frac{1 - \mathrm{e}^{-\alpha \mathrm{L}}}{\alpha} \end{aligned} \tag{2.2}$$

where n_2 is the Kerr non-linear coefficient, which give rise to an intensity dependent

refractive index, and is approximated to be 5×10^{-18} m^2/W, λ is the pump wavelength, and A_{eff} is the effective mode of the light field inside the waveguide [34]. $(\gamma P_0 L_{eff})^2$ is the non-linear interaction term, where P_0^2 shows the quadratic dependence of pair generation rate on the pump power.

Periodically patterned silicon nanophotonic waveguides can have an effective non-linearity coefficient $\gamma_{\text{eff}} \approx 4,000$ $W^{-1}m^{-1}$ to $10,000$ $W^{-1}m^{-1}$ that is 5 to 6 orders of magnitude larger than that of Highly Non-Linear Fiber (HNLF) around a wavelength of 1.5 μm [35, 36], allowing for pair generation using only milliwatts or less of optical pump powers, in a regime where two-photon absorption and free-carrier generation losses may be small. γ_{eff} is defined in Section 2.2.

2.1 Coincidence-to-Accidental Ratio

Once the pairs are generated, they are characterized through a time correlation measurement. The generated photons are detected through two single-photon avalanche diodes (SPADs), followed by a time-correlator. Coincidence-to-accidental ratio (CAR) measures the correlation of the photon pair arrival times. "Accidentals" can result, e.g., from one photon of a pair being lost/absorbed. Fig. 2.1 explains the mechanics of CAR calculation, and Eq. 2.3 shows the expression for CAR, in the presence of detector dark counts.

$$\text{CAR} = \frac{\text{C}}{\text{A}} = \frac{\text{C}_{raw} - \text{A}_{raw}}{\text{A}_{raw} - \text{D}} \tag{2.3}$$

where C is the number of real coincidence counts, A is the number of real accidental counts, C_{raw} is the number of raw coincidence counts, A_{raw} is the number of raw accidental counts, and D is the number of coincidences due to detector dark counts. CAR can be compared with a much known metric: Signal-to-Noise (SNR) ratio. Having a signal at least one order of magnitude stronger than noise (i.e., CAR > 10) suggests a possible implementation for applications such as quantum key distribution (QKD). For example, Takesue et al. in [37] explicitly uses the value of CAR ~ 10 to numerically estimate a 5% error in QKD system using entangled photon pairs.

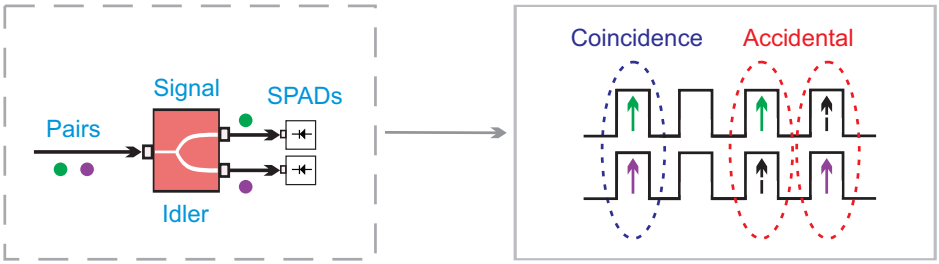

Figure 2.1: Mechanism of coincidence-to-accidental ratio (CAR) measurement. SPAD = Single photon avalanche diode and black dashed arrow is an indication of spurious clicks in the SPADs, generally due to unwanted photons or detector dark counts.

2.2 Straight Waveguide versus Planar Resonant Devices

The pair generation rate described in Eq. 2.1 is for straight waveguides, and for resonant devices the equation requires a modification: $\gamma \rightarrow \gamma_{eff}$ and γ_{eff} is defined as [39]:

$$\gamma_{eff}^2 = S_s S_i \left(\frac{S_p + 1}{2}\right)^2 \gamma^2 \tag{2.4}$$

where $S_{p,s,i}$ are the slowing factors at the pump (p), signal (s) and idler (i) wavelengths. Slowing factor incorporates the effect of resonant cavity, e.g., for a straight waveguide S = 1, and for resonators S > 1. Here, we are interested in the comparison of: (1) Straight waveguide, (2) Single microring resonator and (3) Chain of microring resonators or coupled resonator optical waveguide (CROW). In CROW, the light propagate from input to output through nearest-neighbor coupling, similar to tight-binding model of propagation in solid-state physics. The coupling of N resonators contribute via coherent superposition of each (Bloch) resonance, that is, these N resonances are the 'supermodes' of the combined structure, not N individual, uncoupled resonances. CROW forms an optical slow-light structure, whose dispersion relation exhibits reduced group velocity points [38], and these characteristics are similar to those of photonic crystals, but coupled microring chains are

easier to fabricate and couple light in and out.

In a perfect phase-matched condition, using Eq. 2.1 & 2.4, the pair generation rate (photon pair flux) can be written as [39]:

$$F\left[s^{-1}\right] = \Delta\nu \left(\gamma_{eff} \mathrm{P}_0 \mathrm{L}_{eff}\right)^2 \mathrm{e}^{-\alpha \mathrm{L}} \tag{2.5}$$

where γ_{eff}, $\Delta\nu$, α, and L_{eff} are defined previously with $\mathrm{L} = \mathrm{N}\pi\mathrm{R}$; N is the number of microring resonators. In Ong et al. [39] (Fig. 2), Eq. 2.5 has been evaluated numerically, which suggests, for an identical α, P_0 and $\Delta\nu$, a CROW with about 10 microrings surpasses both a single microring resonator and a waveguide in photon pair flux.

2.3 Coupled Resonator Optical Waveguide

Having gone through the mechanism of photon pair generation in resonant devices, let us look into a CROW with 11 microrings as a source of photon pairs. Fig. 2.2(a) shows a microscope image of a fabricated CROW with 11 microrings, cumulatively spanning a distance of 0.23 mm on the silicon chip with a bend radii of 10 μm. The device was fabricated using CMOS-compatible processes on SOI wafers with 220 nm silicon layer height, and singulated into chips for testing using edge-coupled waveguide-to-fiber tapers. The cross-section of the device is shown in Fig. 2.2(b). The implanted regions create a photo-diode which can monitor the optical power in the CROW, so that the pump wavelength can be aligned to the CROW resonances despite temperature variations – discussed for a single microring resonator in Chapter 6. The transmission spectrum of the device is shown in Fig. 2.2(c), with several passbands of about 1.75 nm in spectral width separated by the 7 nm free spectral range (FSR) of the constituent microrings.

2.4 Generation and Detection of Photon Pairs

The experimental setup is shown in Fig. 2.3. The insertion loss of each fiber-to-waveguide coupler was estimated as 4.3 dB, based on calibration measurements

on separate test sites. Light was transmitted through the CROW in a disorder-tolerant slow light regime, with a wavelength-dependent group index between 24 and 40 (greater values at the shorter wavelengths). The propagation loss was about 0.13 dB per ring including slow light enhancement of the loss, i.e., an insertion loss of about 1.4 dB for the microring section. SFWM process was excited, generating polarization-degenerate and frequency non-degenerate photon pairs. In view of the ripples in the transmission passbands (shown in Fig. 2.2(c)), the pump wavelength

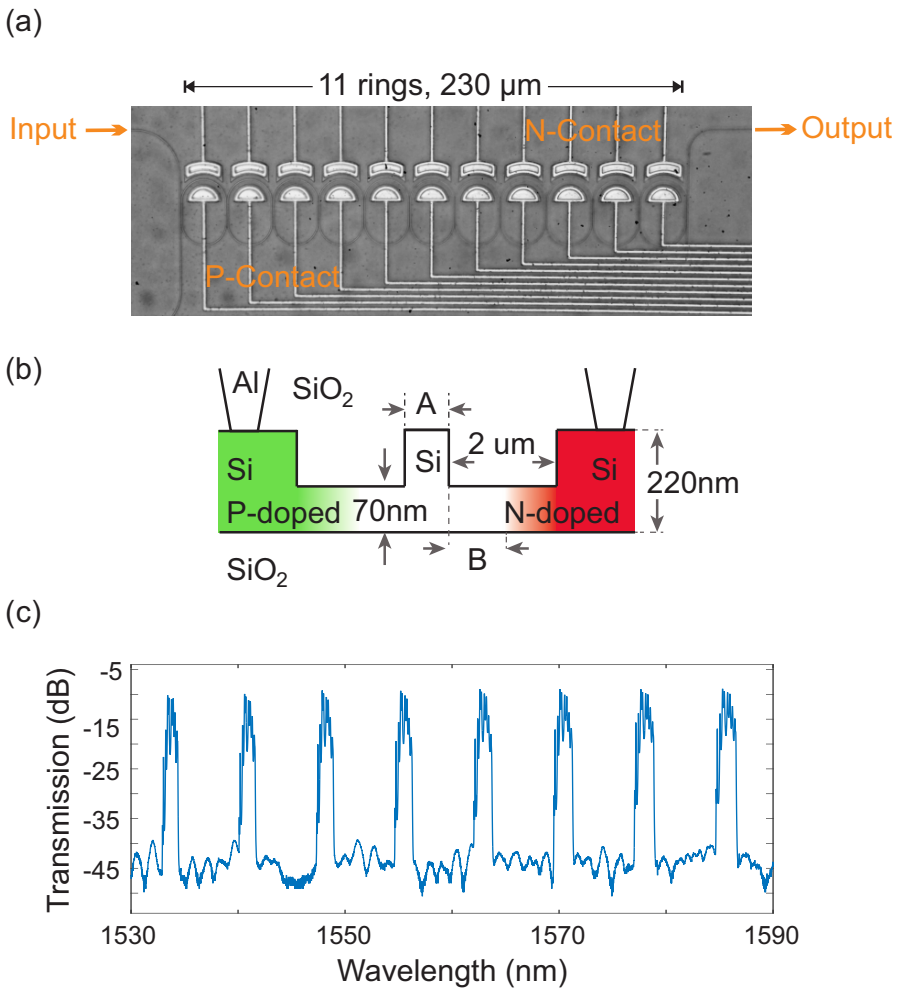

Figure 2.2: (a) Microscope image of CROW with 11 microring resonators. (b) Schematic of the cross-section with A = 650 nm and B = 900 nm. (c) Classical transmission spectrum of the 11-ring coupled-microring device showing a series of passbands and stopbands in a clean, single-mode family, with high passband-to-stopband contrast.

was initially chosen by optimizing the classical four-wave mixing conversion of a weak signal beam at the signal wavelength to the idler wavelength.

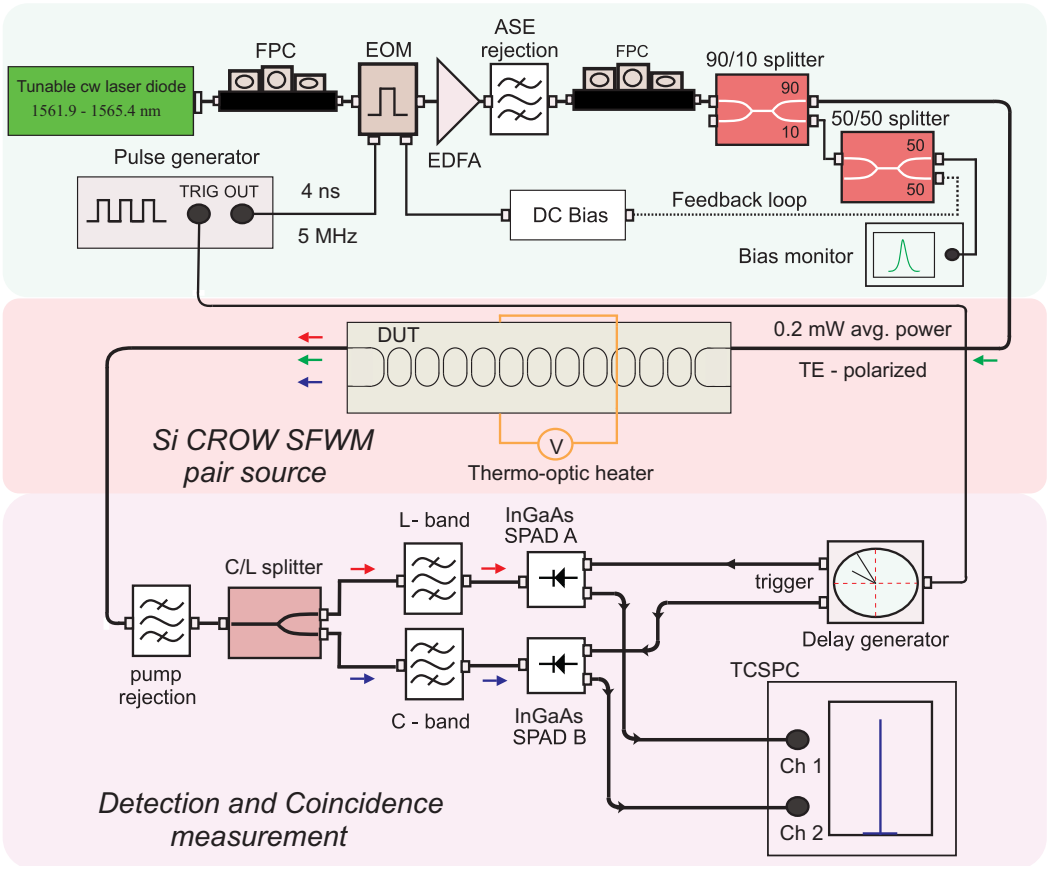

Figure 2.3: Photon pair generation using laser diode-pumped SFWM. EDFA = Erbium doped fiber amplifier, FPC = Fiber polarization controller, EOM = Electro-optic modulator, ASE = Amplified spontaneous emission, DUT = Device under test, TCSPC = Time-correlated single photon counting.

Transverse electric (TE) polarized light at $\lambda_p = 1562.6$ nm with 4 ns pulse width, 5 MHz repetition rate, 0.2 mW average power was used. The generated signal and idler photons were separated using a tunable set of narrowband filters with full-width at half-maximum (FWHM) of 0.6 nm for the C-band and 1.0 nm for the L-band, with insertion loss of 6.2 dB in each case, and passband-to-stopband contrast exceeding 150 dB. Photons were detected using InGaAs SPADs using a reverse bias voltage of 3.0 V, resulting in an estimated quantum efficiency of 10%. The SPADs were electrically gated with a window of 4 ns, synchronously with the optical pump repetition rate. The averaged detector dark count rates in the two

channels were measured to be 94 Hz and 195 Hz. The measured average singles count rates were 98 kHz for the signal photons in the C-band at $\lambda_s = 1547.9$ nm and 76 kHz for the idler photons in the L-band at $\lambda_i = 1577.6$ nm. The output of SPADs were connected to the time-correlator, which measures the coincidence events based on the arrival times of photons in SPAD A and B.

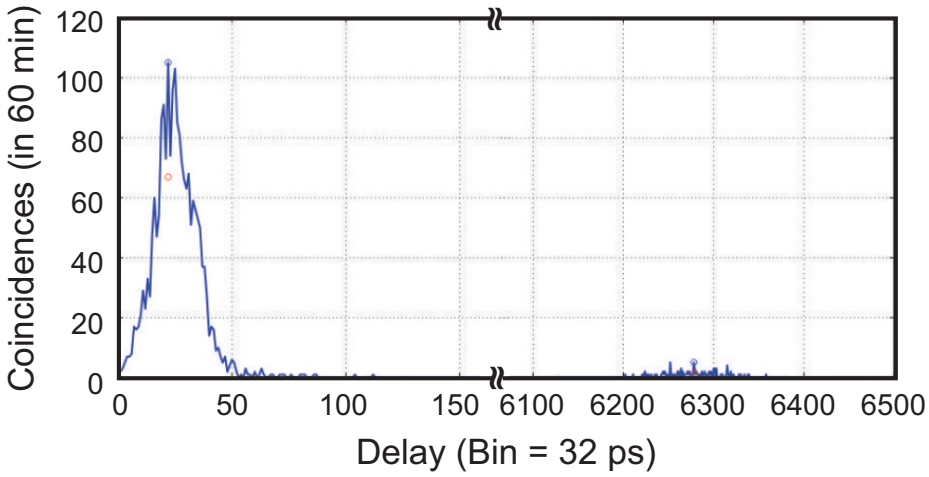

Figure 2.4: Representational TCSPC data – measured with a bin resolution of 32 ps.

Fig. 2.4 shows the representational measurement from the time-correlated single photon counting (TCSPC) module, with x- and y-axis being the delay in arrival times of photons and detected coincidences in 60 min, respectively. Both the generated photons in a given pair are expected to arrive at the same time, with close to zero delay and hence, the real coincidence data (C) should have zero delay on the x-axis. The coincidences detected after one/two/three$\cdots$ clock cycle/cycles represent the accidental data (A). Clock cycle of 200 ns (inverse of 5 MHz $\equiv \frac{1}{5\times10^6}$ sec $= 200 \times 10^{-9}$ sec) with a bin resolution of 32 ps was used for this measurement, and hence, the real and accidental data were separated by the multiples of $200/0.032 = 6250$ bins. Due to the jitter of about 500 ps in the InGaAs detectors, the coincidence data has FWHM of about 500 ps, as can be seen in Fig. 2.4. With an intention to collect the entire zero-delay data, an artificial offset of about 25 bins was introduced in the TCSPC. The accidental after one

clock cycle can be seen at about 6275 bins. Eq. 2.3 was used to calculate the value of CAR from a data similar to Fig. 2.4, where A_{raw} is the average accidentals of many clock cycles.

The CAR was calculated to be 80 ± 24 with pair generation rate of 1.64×10^4 per sec. The uncertainties in CAR come from fluctuations in the measured coincidence and accidental counts, and represent one standard deviation values. It should be noted that due to quadratic dependence on pump power, PGR increases with increase in pump power, but CAR decreases, mostly due to multi-photon pair generation [23–25, 28, 40].

2.5 Spectral Multiplexing and Wavelength Tuning

Now that we understand the generation and detection of photon pairs in silicon based CROWs, let us look into the following two features of resonant devices such as CROWs: (1) A device based on silicon microrings can generate multiple lines of signal and idler photon pairs coupled into the same output waveguide (spectral multiplexing), and (2) Generation of photon pairs in resonator-based devices, whose wavelengths can be tuned using electrical current-driven thermo-optic change of the refractive index of silicon.

2.5.1 Spectral Multiplexing

The wavelength of generated photons in the previous section correspond to Band 2 in Fig. 2.5, but based on energy conservation and phase matching, there are also other available bands for photon pair generation, such as Band 1, Band 3, etc. [41]. For one chosen pump wavelength at 1562.6 nm, photons were being generated in all the neighboring bands. The values of CAR and PGR are mentioned in Table. 2.1. The measured values are within the permissible range, which show the spectral multiplexing feature of CROW.

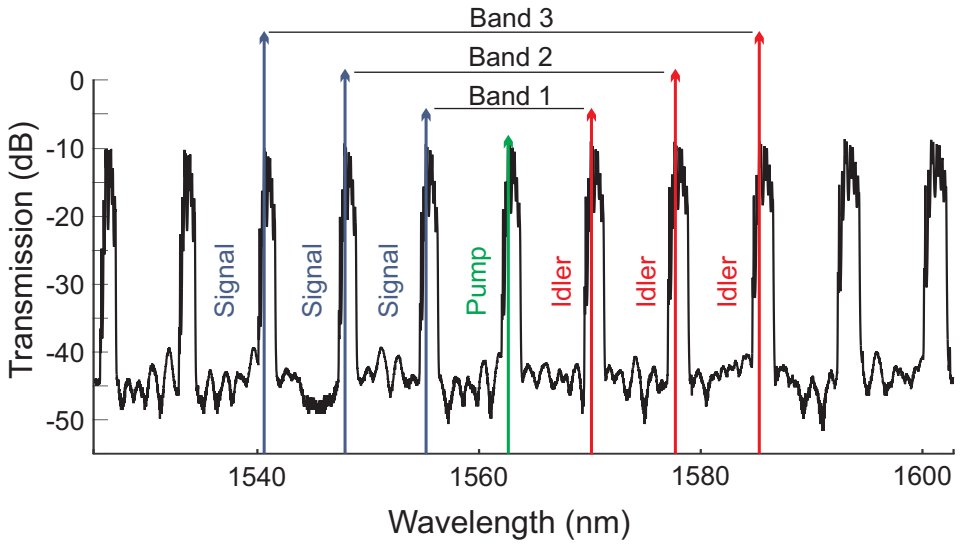

Figure 2.5: A classical transmission spectrum of the 11-ring coupled-microring device at room temperature (296.4 K) showing a series of passbands and stopbands in a clean, single-mode family, with high passband-stopband contrast. Using a single pump, multiple sets of photon pairs were generated, as indicated.

Table 2.1: Simultaneous pair generation from three bands as indicated in Fig. 2.5 at room temperature (296.4 K), using a fixed pump wavelength at 1562.6 nm with 0.2 mW average power.

Band	CAR	PGR (/sec)	PGR (/pump pulse)
Band 1	55±11	6.75×10^{3}	1.4×10^{-3}
Band 2	80±24	1.64×10^{4}	3.3×10^{-3}
Band 3	65±16	1.13×10^{4}	2.3×10^{-3}

2.5.2 Wavelength Tuning

When the chip was thermally heated or cooled using an external current-driven thermo-electric controller (TEC) module, the spectrum shifted cleanly, and without loss of contrast. As shown by the insets to Fig. 2.6, both the signal and the idler wavelengths at which pairs were generated shifted smoothly, in accordance with the predictions of energy and momentum conservation, to longer wavelengths upon heating, without significant change in their spectral separation ($\lambda_{\text{signal}}-\lambda_{\text{idler}}$).

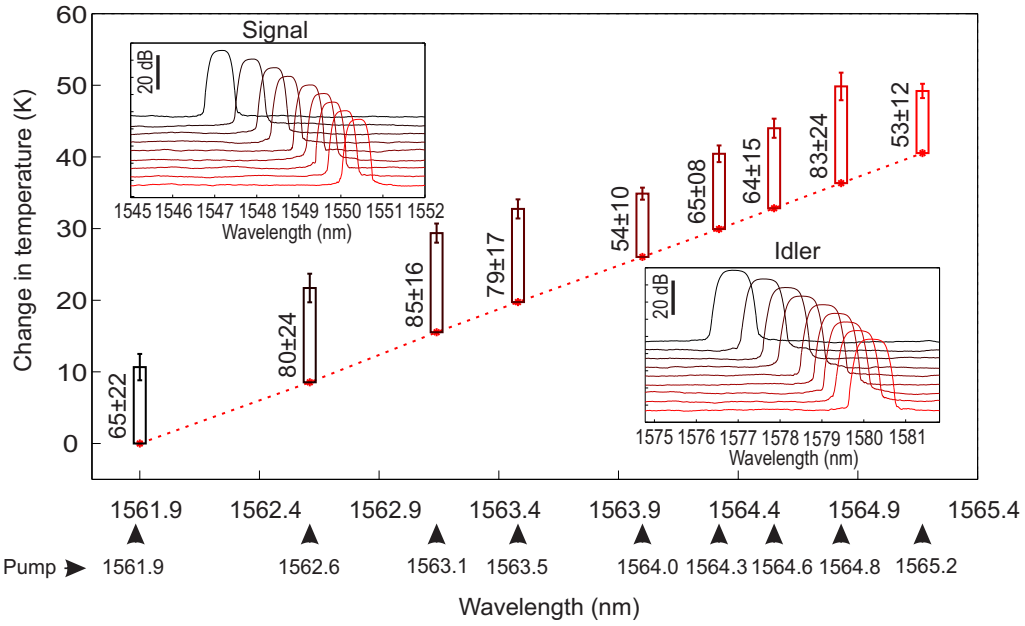

Figure 2.6: Changing the temperature of the chip changes the wavelengths of the signal and idler photon pairs, and requires a linear tuning of the input pump wavelength. The height of the bars is proportional to the measured CAR between the photon pairs. Insets: Peak pair generation wavelengths for signal (top - left) and idler (bottom - right) are shown here by tuned filtering channels, in front of the wavelength insensitive SPADs.

Thus, in this device, photon pairs can be generated at any wavelength, e.g., aligned to a grid of lambdas prescribed by a fiber network, if the free spectral range of the constituent microrings is also compliant with this grid. Table 2.2 shows the pair generation rate for Band 2 (indicated in Fig. 2.6) at several different temperatures; Bands 1 and 3 have similar temperature tuning behavior. Fig. 2.6 shows that the wavelength shift is linear with temperature, and a high CAR value is maintained while tuning.

Temperatures were estimated using a measurement of resistance and a thermistor equation:

$$R_T = R_{T0} \exp\left[\beta \left(T_0 - T\right) / T T_0\right] \tag{2.6}$$

where R_T is the resistance at a temperature T, $\beta = 3900$ was the specified material constant of the thermistor, and $R_{T0} = 10$ kΩ was the resistance at $T_0 = 298.2$ K.

Table 2.2: Coincidence measurements of generated pairs from Band 2 at different temperatures; wavelength shifts with temperature are described in Fig. 2.6.

Temp.(K)	CAR	PGR(/sec)	PGR(/pump pulse)
287.9	65±22	1.27×10^{4}	2.5×10^{-3}
296.4	80±24	1.64×10^{4}	3.3×10^{-3}
303.4	85±16	1.12×10^{4}	2.2×10^{-3}
307.6	79±17	8.59×10^{3}	1.7×10^{-3}
313.9	54±10	1.16×10^{4}	2.3×10^{-3}
317.8	65±08	1.44×10^{4}	2.9×10^{-3}
320.7	64±15	1.39×10^{4}	2.8×10^{-3}
324.2	83±24	1.17×10^{4}	2.3×10^{-3}
328.4	53±12	1.23×10^{4}	2.5×10^{-3}

2.6 Summary

In summary, this chapter discusses the photon pair generation in silicon photonic devices, along with the experimental setup to measure the time-correlation of generated photons. In the later section, this chapter demonstrates the photon pair generation from a comb of frequencies produced by a coupled-microring resonator device pumped by a single wavelength, and its capability of tuning, via electric current, the wavelength of the generated pairs. This demonstration is a step towards realization of compact, electrically-tunable wavelength-division multiplexed quantum light generating devices made using CMOS-compatible fabrication and silicon photonics.

Chapter 2 contains material, reproduced in part with permission, from Ranjeet Kumar, Jun Rong Ong, John Recchio, Kartik Srinivasan, and Shayan Mookherjea, "Spectrally-multiplexed and tunable-wavelength photon pairs at 1.55 μm from a silicon coupled-resonator optical waveguide" Optics Letters Vol. 38, Iss. 16, pp. 2969–2971 (2013). Copyright 2013, Optical Society of America. The dissertation author was the primary author of this paper.

Chapter 3

Control over Bi-Photon Spectrum

In the previous chapter, the discussion was about the generation of photon pairs in silicon devices such as CROWs. CROWs generate photon pairs in multiple passbands, and while the discussion, in part, was about the spectral multiplexing over different bands, the spectra of photons within individual passbands were not explored. The bi-photon spectrum within the individual passbands can provide the information about their bandwidth and correlation properties.

Due to 'photon starved' nature of the modern communication systems, we always seek to use more degrees of freedom than simple on-off keying [20]. Some of the common methods to encode information includes polarization-bin encoding [17], time-bin encoding [42], and frequency-bin encoding [18]. However, the quantum equivalent of manipulating the spectrum of the source has not been demonstrated. Though directly-modulated semiconductor lasers are widely used and well understood, demonstrating a similar concept in quantum optics is not simple because a number of issues have to be simultaneously addressed. These include the following: showing a photon source using semiconductor technology which can be easily manufactured, designing internal degrees of freedom in the architecture of the source which can be externally manipulated by a user to generate different quantum spectra, and developing a measurement procedure for the different photon spectra, rather than simply counting photons (as discussed in the previous chapter).

The bi-photon state $|1\rangle_s|1\rangle_i$ of the photon pairs generated inside a CROW

through SFWM can be written as:

$$|\psi\rangle \propto \iint d\omega_s \, d\omega_i \left[\Phi\left(\frac{\omega_s+\omega_i}{2}\right)\right] \overbrace{\phi_{\mathrm{PM}}(\omega_s,\omega_i)t(\omega_s)t(\omega_i)}^{\Psi(\omega_s,\omega_i)} |1\rangle_s|1\rangle_i \tag{3.1}$$

where Φ is the pump spectral envelope – generally taken as a Gaussian function [43], ϕ_{PM} is the phase matching function, and t is the transfer function (amplitude transmission) of the device. Eq. 2.1 described the $\phi_{\mathrm{PM}} = \mathrm{sinc}\left[\beta_2 \left(\Delta\omega\right)^2 \mathrm{L}/2 + \gamma \mathrm{P}_0 \mathrm{L}\right]$ (approximation of $\mathrm{sinc}\left[\Delta\beta\,\mathrm{L}/2 + \gamma \mathrm{P}_0 \mathrm{L}\right]$ for $\Delta\omega \ll \omega$) as the phase matching term for straight waveguides, which under low input pump power can be approximated as $\mathrm{sinc}\left[\beta_2 \left(\Delta\omega\right)^2 \mathrm{L}/2\right]$. $\Delta\beta$ is the deviation from the perfect phase-matching, and in devices such as CROW, the expression for $\Delta\beta$ is more complicated compared to a straight waveguide, involving a discrete set of wavenumbers and terms that describe the reduction of group velocity (slow light effects) at these wavelengths [38].

The bi-photon spectrum or Joint Spectral Amplitude (JSA), which is a product of Φ and Ψ in Eq. 3.1, can be measured experimentally through Joint Spectral Intensity (JSI), which is given by the magnitude-squared of the JSA. The shape of the JSI in the $\omega_s - \omega_i$ plane depends concurrently on the linewidth and wavelength of the pump, the phase-matching points and the transmission functions $t\left(\omega_s\right)$ and $t\left(\omega_i\right)$ in the passbands of the two generated photons. The JSI has been widely used in SPDC experiments for distinguishing between separable, correlated and anti-correlated two-photon states, and quantifying entanglement [44–56]. The manipulation of JSI is an active field of research in SPDC, and it is mostly done through the manipulation of pump pulse [57]. Control over the JSI can be useful in creating a versatile SFWM pair source, whose emission properties can be adapted to the target application; e.g., for a heralded single photon source, uncorrelated photon pairs are needed [54–56, 58], whereas for an entangled photon source using the spectral degree of freedom, the photon pairs may need to be highly correlated [59]. Shaping the JSI of photon pairs after generation reduces their spectral brightness significantly, and it is beneficial instead to modify the optical density of states at the source [60].

3.1 JSI in CROW

Eq. 3.1 suggests that the simultaneous energy conservation and phase matching determine the JSI of the two-photon state generated by a pump beam of a particular frequency or wavelengths. Fig. 3.1(a) represents an idealized map of Ψ in terms of the quantity defined in the integrand of Eq. (3.1), i.e., the product of the two-dimensional phase matching points for $N = 5$ coupled microresonators and the transfer functions at the two passbands of the generated photon pair. Along the horizontal and vertical axis, the transmission spectra at the ω_s and ω_i passbands are plotted, showing the five supermode transmission resonances. In real CROW, the separation between the resonances are not constant, but for simplicity it is shown to have a constant separation. The number of transmission resonances in each band is equal to the number of resonators (five), and together, they form $5 \times 5 = 25$ phase-matching points in the two-dimensional plane at which photon-pair generation can be efficient. When the pump frequency is fixed, the equation $2\omega_p = \omega_s + \omega_i = \text{constant}$. In the two-dimensional $\omega_s - \omega_i$ plane shown in Fig. 3.1(a), this equation defines the JSI to be one of the diagonally-oriented boxes shown with dotted white lines. Different choices of ω_p result in the selection of different regions and correspondingly different JSIs, e.g., the regions marked by the labels 'b', 'c' and 'd' correspond to the JSIs shown in Figs. 3.1(b), 3.1(c) and 3.1(d), respectively. Other choices are also possible, corresponding to the unmarked diagonals in Fig. 3.1(a).

The width (along the short axis) of the regions indicated by white dotted lines in Fig. 3.1(a) is given by the spectral width of the pump pulses, which in our experiment was less than 300 MHz, and therefore, only one narrow strip (one band of resonances) was selected. The length (along the long axis) of the regions indicated by white dotted lines in Fig. 3.1(a) is given by the lesser of two quantities: either the spectral extent of phase matching (which was quite wide in our device, exceeding several nanometers [35]), or the extent of the transmission band, that is, the end-to-end span of the supermode resonances (which is determined by the strength of the inter-resonator coupling coefficient [61]). In our device, the latter quantity was the smaller one, and therefore, depending on the pump frequency,

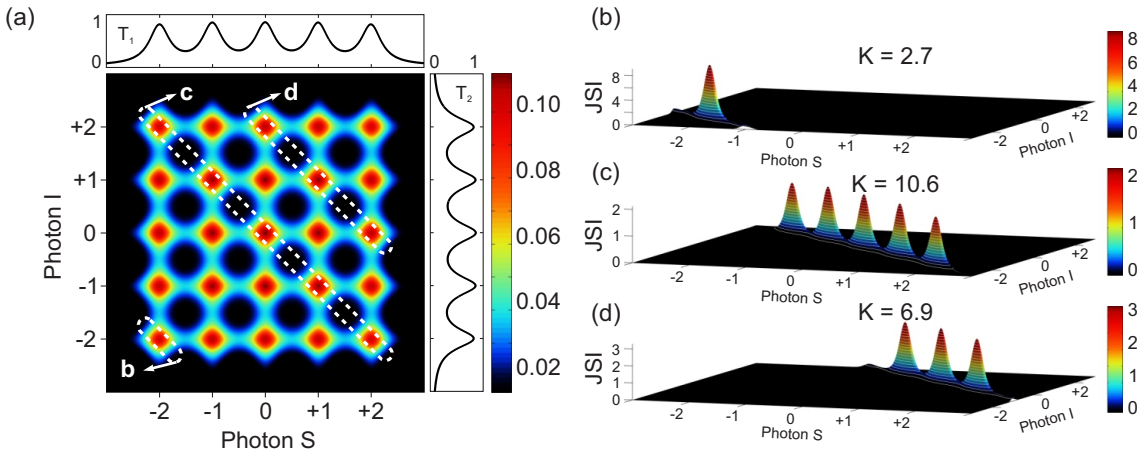

Figure 3.1: (a) This two-dimensional plot obtained by numerical simulation shows the contours of the function Ψ defined in Eq. 3.1 as a function of the wavelengths of the two generated photons, relative to the band center. Shown to the top and the right are the transmission amplitudes in the two bands. The wavelength of the pump determines which diagonally-oriented slices of this phase-matching diagram comprise the joint-spectral intensity (JSI) of the photon pair, with three particular possibilities for the JSI marked by regions 'b', 'c' and 'd'. (b) The JSI of the two photon state when the pump wavelength is positioned at the edge of its transmission band, showing a state with one major peak in the JSI. Such a state is suitable for heralding [46,58]. (c) The JSI when the pump wavelength is positioned in the middle of its transmission band, showing a state with 5 distinct peaks, which is suitable for an entangled pair source [46,59]. (d) The JSI when the pump is tuned to another resonance in its transmission band, with three peaks as an intermediate case. In each figure, the horizontal axes are in units of normalized wavelength (one unit equals the separation between adjacent peaks) measured relative to the band center, and the vertical axes and color scales are normalized so that the area under the JSI is unity. The K values represent the Schmidt numbers, i.e., the dimensionality of the singular-value decomposition of the JSI.

the number of peaks in the JSI could be varied from approximately one (in Fig. 3.1 (b)), when the pump was positioned at supermode resonance located at the edge of its own transmission band) to the total number of resonators in the chain (5 in Fig. 3.1(c), when the pump was positioned at the center of its transmission band).

Fig. 3.2(a) shows the construction of the JSI using the calculated transfer function of an 11-ring coupled resonator structure, which models the device that was fabricated. The peaks are not of the same size and strengths because near the band-edges, the resonances are sharper and the transmission magnitude decreases

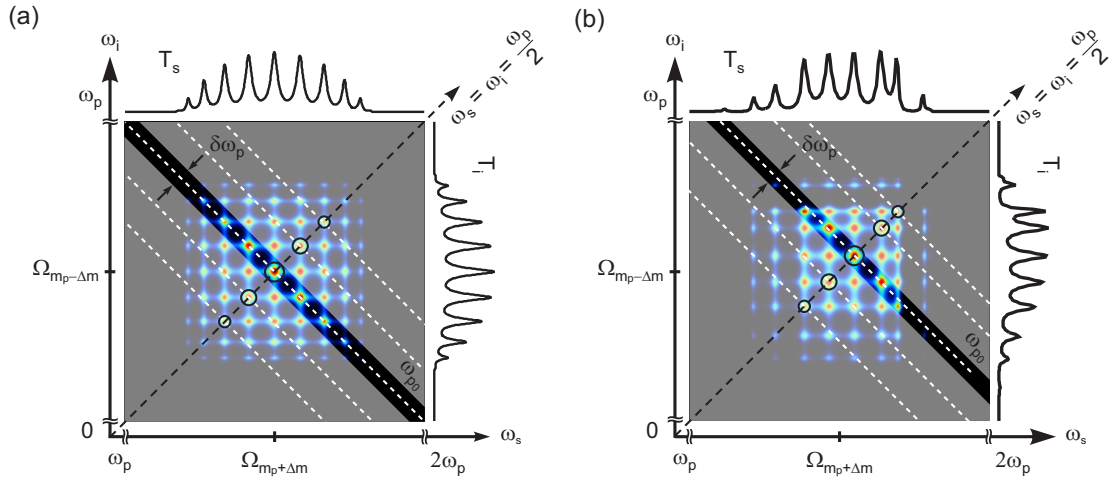

Figure 3.2: (a) The JSI can be interpreted as the section of the $N \times N$ array of phase-matching points in the $\omega_s - \omega_i$ plane which are selected by the input pump (of a particular energy ω_{p0}) based on the principle of energy conservation to lie along the diagonal regions shown by dotted white lines. The width of the selected region which defines the JSI is given by the spectral width of the pump envelope $\delta\omega_p$. The pump itself must be resonant with one of the supermodes in its transmission band; the possible choices of the pump frequency are shown by the black circles along the diagonal line, defined by $\omega_s = \omega_i = \omega_p/2$. The JSI consists from 1 up to N peaks; here N was taken as 11 in this representative calculation of the device used in the experiment, which consisted of 11 coupled silicon microring resonators. The horizontal axis represents the optical frequency of the 'signal' photon, and the vertical axis represents the optical frequency of the 'idler' photon; in both cases, the (ideal) transmission of one passband is shown to the top and right edges of the plot, respectively. (b) Due to fabrication disorder that affects the precise coupling coefficients between the resonators, the experimentally measured transmission spectrum at the signal and idler passbands shows lower transmission at some of the band-edge resonances compared to the band-center. Correspondingly, the calculated JSI shows about five peaks should have higher brightness than the others.

(see Fig. A.1). The JSI expected from the measured transmission at the signal and idler wavelengths is shown in Fig. 3.2(b); this figure differs from the ideal because of at least two possible reasons: (i) the increased loss at band edges due to the increase in the slowing factor near the band-edge, (ii) errors in fabrication resulting in a different coupling coefficient than intended between the feeder waveguides and the first / last microring resonators (i.e., imperfect apodization). These issues can

be addressed with improved fabrication, but for the present device, the JSI should vary between one and five peaks. The JSI can consist of any number of peaks ranging from 1 to N if the pump spectral width is narrow, and upto N^2 if the pump spectral width can be changed. Chains of upto $N = 235$ coupled silicon microring resonators have been demonstrated with an end-to-end spectral width of the transmission band of only about 5 nm [61], but those structures are not suitable for pair-generation, because although the propagation loss per ring was quite low (about 0.08 dB/ring), the total transmission loss was not low enough for such long chains.

3.2 Schmidt Number

Schmidt number K is a widely used measure of entanglement, representing the number of orthogonal modes in the singular-value decomposition (SVD) of the magnitude of JSA [44]. In this chapter, it is calculated as the square root of the measured JSI under the assumption of flat spectral phase. A bi-partite state is entangled if the number of non-zero eigenvalues is more than one. The Schmidt number can equal the Shannon number for a communications system, which reflects the number of independent communication channels between source and receiver [62] and is related to the "entanglement entropy" [45]. As shown in Figs. 3.1(b) – 3.1(d), K can take on a wide range of values for the different JSIs. In the most general case, K can be continously varied by changing the inter-resonator coupling coefficients [63]; however, this is difficult to realize in practice. Here, we show the selection of different values of K from a discrete set of alternatives, achieved by two different ways: either by changing the temperature of the chip, so that the transmission bands shift with respect to the (fixed) pump frequency, ω_p, or alternatively, by changing the pump frequency while holding the chip temperature constant. Fig. 3.3 shows the zoomed-in transmission spectrum of the device used in this chapter – CROW with 11 microring resonators.

In conventional SPDC experiments, the pump beam is shaped by bulk optics components in order to fine-tune the spectral correlations [46,54–56], but the ability

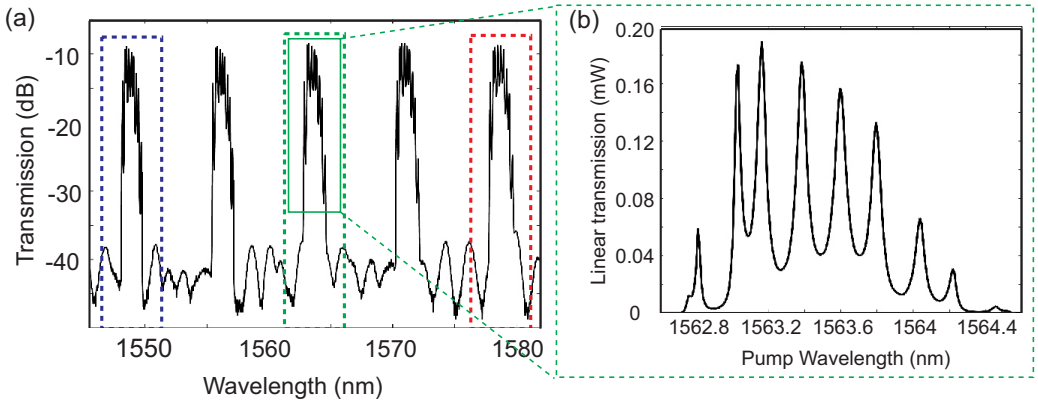

Figure 3.3: (a) The bands indicated by the blue, green and red dashed-line boxes denote the passbands for the signal, pump and idler beams. (b) The transmission in a single passband is magnified, to show the individual transmission peaks (Bloch mode resonances). Unlike the idealized transmission calculated for an $N = 11$ coupled-resonator waveguide, shown in Fig. A.1, the transmission spectrum for the experimentally-fabricated device shows peaks of unequal height because of the enhanced loss near the band-edges and fabrication imperfections.

to select manifestly different JSIs with vastly different K's is a unique aspect of this type of lithographically-fabricated, multi-component structure that has not been demonstrated before, for any other photon pair source.

3.3 Experimental Details

The experimental conditions for generating photon pairs and measuring coincidences are similar to the last chapter, showing good coincidence-to-accidentals ratio for a wide range of temperatures and pump wavelengths. Light was coupled between optical fibers and the on-chip waveguides using inverted tapers on the waveguides, and lensed tapered single-mode polarization maintaining fibers. The insertion loss of each fiber-to-waveguide coupler was estimated as 3 dB, based on the calibration measurements on seperate test sites. SFWM generated polarization-degenerate and frequency-nondegenerate photon pairs, and the wavelengths of the pump and the generated photons were in the telecommunications band near 1.55 μm. The required pump power was about 0.2 mW after coupling to the on-chip waveguide from the input fiber. The pump wavelength was aligned with one

of the transmission passbands of the coupled-resonator device near 1.55 μm. The continuous-wave pump light was carved into pulses of duration approximately 4 ns at repetition rate 60 MHz using an electro-optic modulator. For measurement, the photons were filtered using a tunable set of narrowband filters with full-width at half maximum of 0.6 nm for the C-band and 1.0 nm for the L-band, insertion loss of 6 dB, and passband-to-stopband contrast exceeding 150 dB. SPADs were used at an estimated quantum efficiency of 10%. The average detector dark count rates in the two channels were measured to be 1.53 and 2.5 kHz. The electrical "clicks" from the SPADs were processed using a fast AND gate (7,400 series TTL logic integrated circuit) and a frequency counter to measure the number of coincidences in a given time window.

3.4 Deconvolution of the Filter PSF

The rapid measurement of JSI is a non-trivial problem. The peaks and valleys which distinguish one JSI from another are separated by a frequency interval of about 20 GHz (about one-tenth of a nanometer), and whereas classical optical spectrum analyzers are capable of providing such a high resolution, they are not sensitive at the single photon level. On the other hand, quantum photon detectors such as SPADs are not wavelength-selective. While two-dimensional arrays of SPADs now being developed [64, 65] will be beneficial in the future, here, we use high-contrast tunable telecommunications-grade optical filters in front of the SPADs, as shown in Fig. 3.4(a), to measure the JSI by scanning over the two-dimensional frequency grid. The measured data, of which two examples are shown in Fig. 3.4(c) and 3.4(g), represent the convolution of the actual JSI and the point-spread function (PSF) of the filters shown in Fig. 3.4(b). There are a number of different ways of deconvolving blurred images and as a representative method, we used the Richardson-Lucy (RL) algorithm [66]. The RL deconvolution is an iterative procedure for recovering, in a maximum-likelihood sense, a latent image that has been blurred by a known PSF. The end-point of the iteration generally needs to be determined by the user, and we use our prior knowledge of typical JSIs

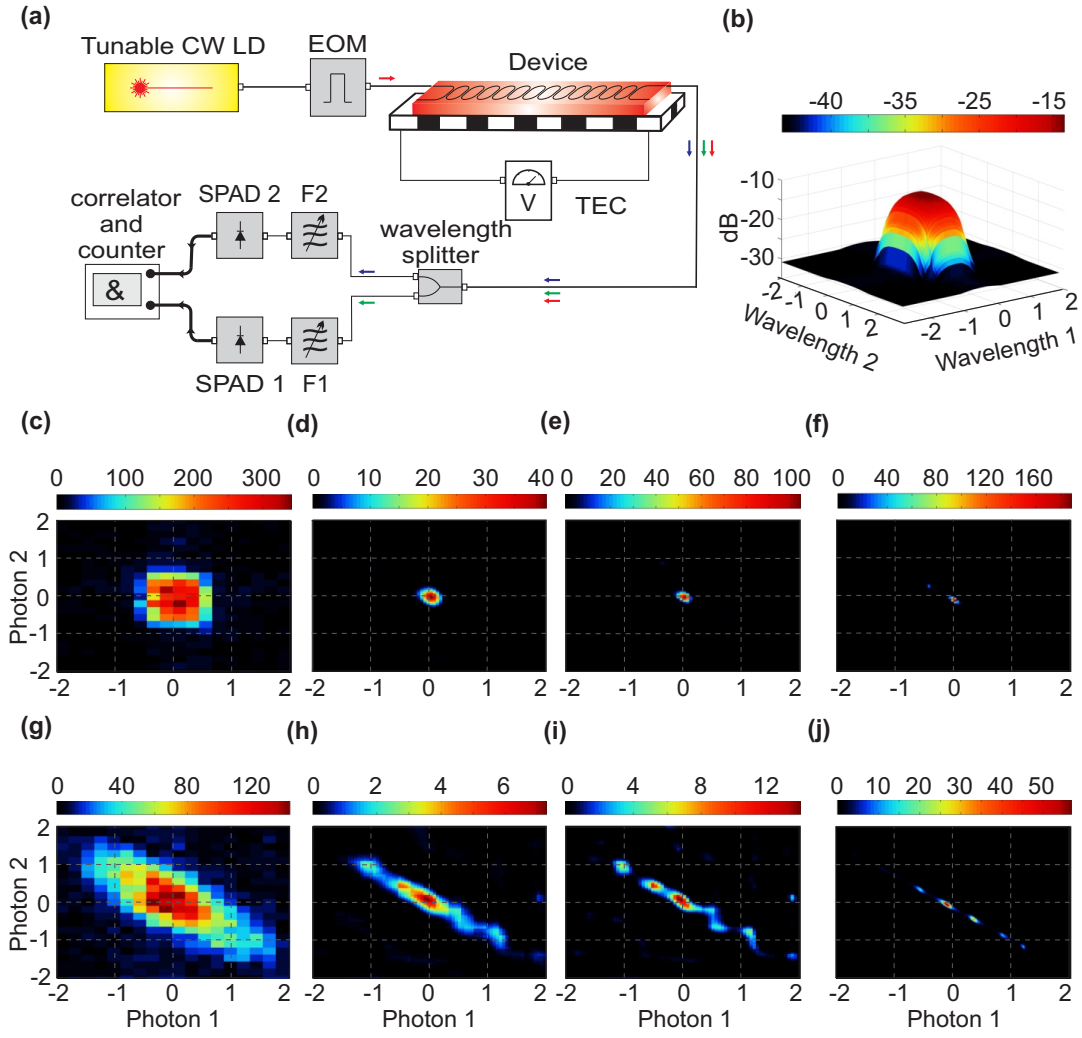

Figure 3.4: (a) Photon pair generation using laser diode-pumped SFWM. The device temperature was controlled using a thermo-electric controller (TEC). Tunable filters were used in front of the SPADs to measure the JSI. (b) The filter point-spread function (PSF) had a full-width at half-maximum of 0.6 nm along the axis for photon S and 1.0 nm along the axis for photon I, which resulted in the measurement of a blurred JSI. The colorbar represents transmission in dB. (c) & (g) Examples of two different raw (blurred) JSIs, which were deconvoluted from the PSF using the iterative Richardson-Lucy algorithm, with (d) & (h) 20 iterations and with (e) & (i) 50 iterations. (f) & (j) A classical four-wave mixing experiment was performed to identify the phase-matching points. Each JSI was normalized to unit area, consistent with its definition as a probability density. In panels (c)-(j), the horizontal axes are in units of normalized wavelength (one unit equals 0.6 nm), measured relative to the respective band centers ('Photon S' : 1548.8 nm, 'Photon I' : 1578.7 nm).

(as shown in Fig. 3.1) as a guideline, and confirm our choice by a classical four-wave mixing experiment [53]. In Figs. 3.4(d), and 3.4(e), we show the results of deconvolution on the measured data (Fig. 3.4(c)) for 20 and 50 iteration steps, respectively. Similarly, for the measured data shown in Fig. 3.4(g), we show the results of deconvolution with 20 and 50 iteration steps in Figs. 3.4(h) and 3.4(i), respectively. In each case, we stopped at 50 iterations, because the general shape and "sharpness" of the JSI was then similar to the phase-matching function measured by a classical four-wave mixing experiment, shown in Figs. 3(f) and 3(j) for the two cases.

3.5 Measurement of the JSI

Fig. 3.5 shows that different JSIs were obtained experimentally from a CROW with 11 microrings (transmission spectrum shown in Fig. 3.3). In Fig. 3.5(a) –3.5(c), the optical pump wavelength was kept constant at $\lambda_p = 1563.61$ nm, and the chip temperature was tuned from 27.7 °C (Fig. 3.5(a)) to 30.2 °C (3.5(b)) and to 37.3 °C (3.5(c)). This range of temperature variations can be achieved by conventional thermo-electric controllers, such as those incorporated within commercial semiconductor lasers [20]. In Fig. 3.5(d)–3.5(f), the chip temperature was kept constant at 30.2 °C and the pump wavelength was tuned from 1563.03 nm (Fig. 3.5(d)) to 1563.61 nm (Fig. 3.5(e)) and to 1563.79 nm (Fig. 3.5(f)). This range of wavelength variation required of the pump is comparable to the range of tunability offered in compact commercial tunable semiconductor lasers [20], which can therefore be conveniently used to pump the silicon chip. Other different JSIs can also be obtained; however, we limit our study to these three examples because each frame shown in Fig. 3.5 took many hours to acquire since the optical filters were individually scanned over the two-dimensional grid.

In the next section we show a measurement example in which the de-blurring algorithm was not needed, e.g., to decide between three distinct JSI alternatives, where the measurement took only 30 seconds. In Fig. 3.5(a) and Fig. 3.5(c), the JSI showed a single peak, but because of the elliptical shape of the peak, the

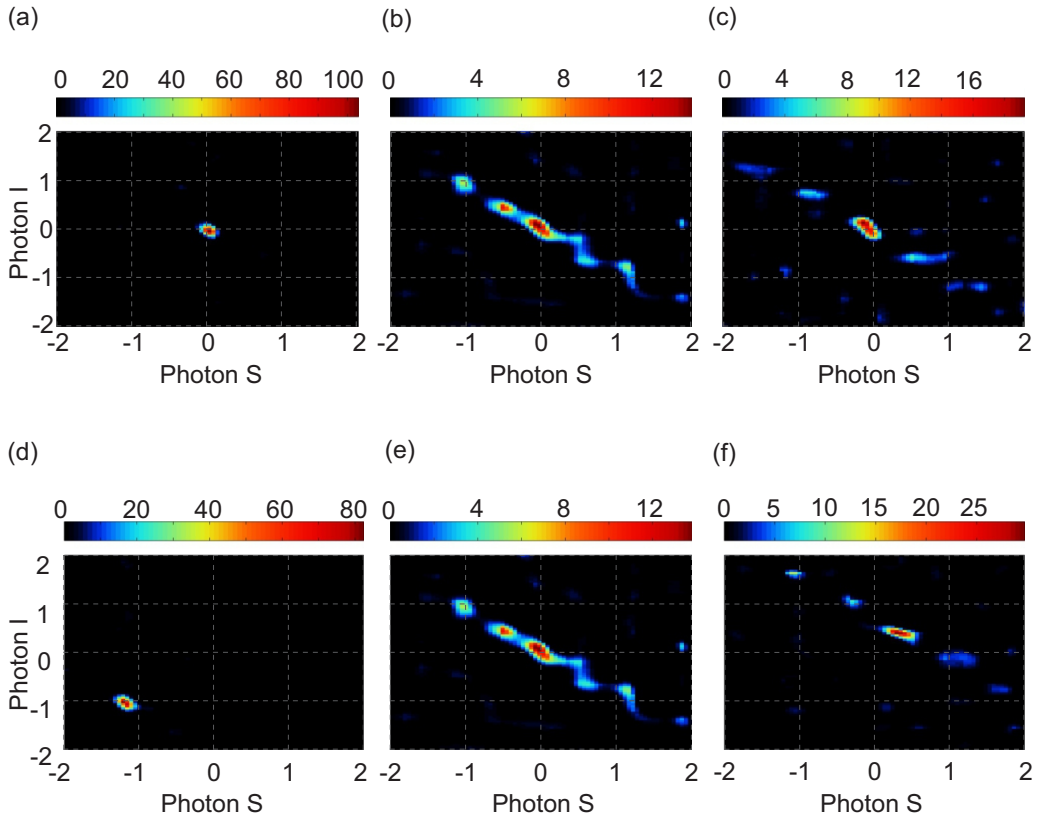

Figure 3.5: Experimentally generating photon pairs with different JSIs. Distinctly different JSIs can be obtained by tuning either the chip temperature or the pump wavelength. (a), (b) & (c) Three JSIs measured with a fixed pump wavelength (1563.61 nm) while tuning the TEC controlling the chip temperature to 27.7 °C (a) to 30.2 °C (b) and to 37.3 °C (c). (d), (e) & (f) Three JSIs measured with a fixed TEC temperature setting of 30.2 °C while tuning the pump wavelength to be 1563.03 nm (d), 1563.61 nm (e), and 1563.79 nm (f). In each case, the range of wavelengths over which data was acquired was the same. The Richardson-Lucy algorithm was used to deconvolve the point spread function of the filters in front of the SPADs with 50 iterations. The Schmidt numbers are $K = 1.95$ (a), 5.72 (b), 7.02 (c), 1.88 (d), 5.72 (e) and 5.47 (f). In each panel, the horizontal axes are in units of normalized wavelength (one unit equals a wavelength separation of 0.6 nm) measured relative to the respective band center, which for 'Photon S' was 1548.8 nm and for 'Photon I' was 1578.7 nm. The vertical axes and color scales are normalized so that the area under each JSI is unity, reflecting the fact that JSI is a probability density.

Schmidt number K is greater than 1. To reduce K without shaping the pump pulse, the device design should be adjusted to support a slightly broader spectral envelope for the pump pulse. The results of Fig. 3.5 show that temperature tuning

and pump wavelength tuning result in similar effects, and either method of selecting different JSIs can be adopted in practice. The peak coincidence rates are estimated as (from panels a to f in sequence): 72 kHz, 30 kHz, 18 kHz, 61 kHz, 30 kHz, and 20 kHz. These rates are calculated from the measured coincidence rates at the detectors after factoring out the chip-to-fiber coupling loss (3 dB), off-chip filter losses (6 dB) and detector quantum efficiencies (10%).

3.6 Rapid Differentiation of the JSIs

Measurement of JSI is a slow process, as described in the previous section, but for some applications, it may not be necessary to wait for the full acquisition, e.g., a choice between a finite number of JSI alternatives can be made significantly faster.

Fig. 3.6 shows the result of a representative experiment in which the silicon chip transmits photon pairs with different JSIs encoded in different time slots, thereby encoding information in the quantum spectrum of the photon pair. We choose the three alternatives for JSI shown in Fig. 3.5(d), (e) and (f) as the possible choices at the transmitter. The receiver, which consists of the tunable filters and SPADs, measures a wide two-dimensional wavelength spectrum sufficient to cover all possible choices of the JSI. In the interest of making a faster measurement, we did not measure the full 2.4 nm $\times$ 2.4 nm span shown in Fig. 3.4 and limited our measurements instead to a smaller 0.6 nm $\times$ 1 nm window which was sufficient to distinguish between the three particular JSIs under consideration.

The tall coincidence peaks shown in Fig. 3.6(a) correspond to the cases where the filter settings at the detector were correctly matched to the JSI that was transmitted. Coincidence counts were accumulated for a duration of 150 s for each of the 9 entries. The low off-diagonal peaks represent cases where the detector's JSI measurement was not matched to that of the transmitted JSI.

The dominant diagonal entries of the matrix of values showed that measurement over 150 s was sufficient to clearly distinguish at the receiver which JSI was transmitted. A further speed up can be achieved, to about 30 s. In Fig. 3.6(b), we

show the results of a timed experiment, in which the pair-source was programmed to transmit the three JSIs shown in Fig. 3.5(d), (e) and (f) in sequence. In each case, the diagonal entry of the matrix was the dominant one, showing that the correct JSI could be identified.

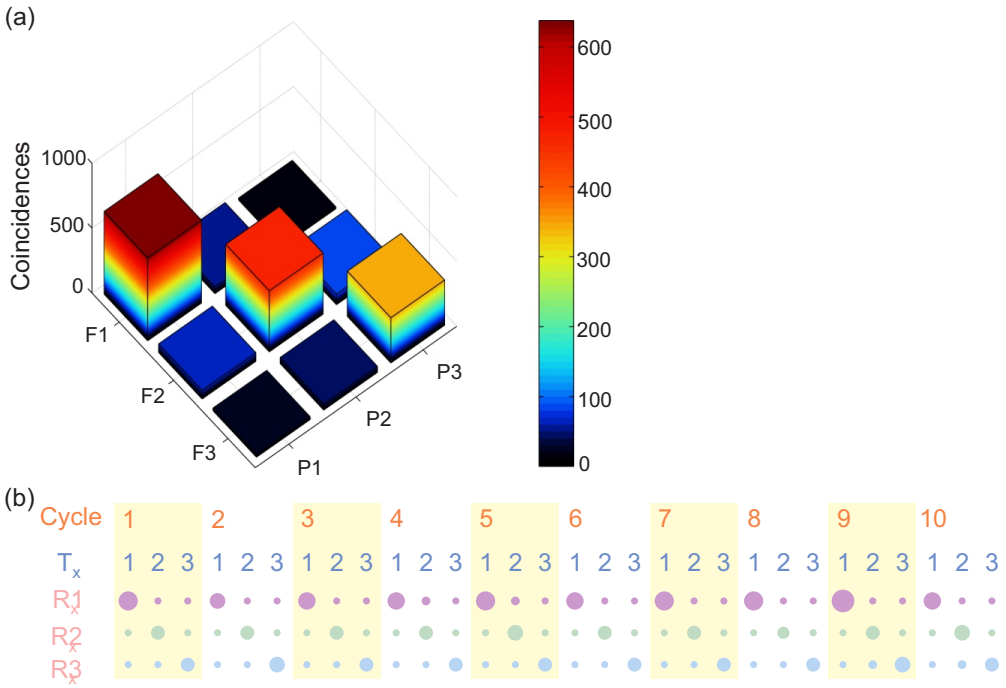

Figure 3.6: Distinguishing between JSIs more rapidly. (a) Photon pairs were generated in one of the three JSIs shown in panels Fig. 3.5(d), 3.5(e) and 3.5(f) , and labeled P1, P2 and P3 respectively. By counting coincidences with three different filter settings (labeled F1, F2 and F3), the detector independently attempted to infer the JSI. Correct alignment, i.e., F1 to P1, or F2 to P2, or F3 to P3, resulted in the largest number of measured coincidences as shown by the tall bars on the diagonal, compared to the small number of mis-matched counts in the off-diagonal entries. The colorbar indicates measured coincidences in a duration of 150 s. (b) The transmitter cycled through the "P1-P2-P3" pattern 10 times, each of duration 30 s. At the receiver, the diameter of the circles is proportional to the number of measured coincidences in the time interval. Since the diagonal entry in each case is the largest, the receiver can correctly identify which JSI was transmitted among the three alternatives within each time slot.

3.7 Discussion

These results show the rich diversity of JSIs that can be generated by exploiting the degrees of freedom offered by chip-based lithographically-fabricated photon-pair sources, as contrasted with their bulk crystal or fiber counterparts. In addition to the simple tuning schemes shown here, the individual resonator frequencies or coupling coefficients can be tuned, to realize even more interesting JSI shapes.

Exploitation of higher-dimensional states for communication is of considerable research interest but the most widely-studied examples of spatially-encoded or polarization-encoded states are generally not robust to transmission over conventional optical fiber or realistic atmospheric channels. One example of utilizing the frequency degree of freedom to overcome these limitations is time-frequency coding [67], where the ability to achieve high values of K without requiring a large frequency bandwidth can relax the timing constraints on detectors. Since there is a strong trade-off between detector speed and efficiency of single-photon detectors at the present time, the ability to generate strong spectral correlations over a narrow band has been desired [67], so that the arrival-time coincidences can be stretched over a long enough period to be resolved by detectors. Unlike the elliptical JSIs generated by SPDC, the JSIs discussed here use the two-dimensional frequency space more fully, and can achieve large Schmidt numbers in a bandwidth of only a few nanometers.

3.8 Summary

In summary, these results have demonstrated control over the bi-photon spectrum using compact, chip-scale photon pair sources, made using conventional planar lithography on silicon wafers with CMOS-compatible fabrication procedures. Such devices combine the high nonlinearity of the silicon material with internal degrees of freedom resulting from the design of the optical circuit in which the photons are generated. We have demonstrated that the JSI of the two generated photons can be controlled by either selecting different pump wavelengths,

or different chip temperatures, and additional ways of programming the chip can be envisioned. The potential for high density of information encoding in the spectrum of the photon pairs will lead to advances in both regular and quantum optical communications.

Chapter 3 contains material, reproduced in part with permission, from Ranjeet Kumar, Jun Rong Ong, Marc Savanier, and Shayan Mookherjea, "Controlling the spectrum of photons generated on a silicon nanophotonic chip" Nature Communications Vol. 5, art. 5489 (2014). Copyright 2014. The dissertation author was the primary author of this paper.

Chapter 4

Proof of Entanglement

In the previous chapter, we discussed the mechanism to control the biphoton spectrum, and its usefulness. Pairs with $K = 1$ are supposed to be uncorrelated and with $K > 1$ are supposed to be non-classically correlated, or entangled – where K is the Schmidt number. Though this a generally accepted metric, it has been argued that just Schmidt number calculation is not sufficient to prove the non-classical correlation between pairs, mostly due to its mathematical construct and vulnerabilities toward numerical artifacts. In quantum community, a generally accepted norm for the proof of entanglement is the violation of Bell's inequality [68]. The violation of Bell's inequality implies the correlation between the particles cannot be explained using *local hidden variables*, and therefore, they are non-classically correlated. The original Bell's inequality was derived for spin/polarization degree of freedom but in 1989 J. D. Franson rederived the inequality for energy-time degree of freedom [69].

The wave-function of quantum states collapse with measurements, and hence, leaving them of no further use. So, unlike a classical object, a quantum object requires extreme care, while being probed. In SFWM process, through energy conservation ($2\omega_p = \omega_s + \omega_i$), we know the combined energy of the generated photons, but we do not know the energy of the individual photons, unless we measure it or in other words, collapse their wave-functions. In the time-domain, this means, it is known that the photons were generated within the two-photon coherence time but we do not know the exact emission time [70]. Here we used a Franson

type experiment to investigate the energy-time entanglement [69, 70]. For silicon photonics, such measurements have been shown recently for the (single) microring resonator [40, 71, 72] and the photonic-crystal coupled cavity waveguide [73]. In this chapter, we performed a similar experimental test of entanglement on photon pairs generated by our coupled-microring structure.

4.1 Experimental Details

The device, fabricated in the same batch as the one described in the previous chapters, was pumped for SFWM with a TE-polarized light with an average power of few mWs (typically 3 - 5mW) in the waveguide (wavelength $\lambda_p \approx 1561.5$ nm, pulse width = 8 ns and repetition rate = 15 MHz). Figure 4.1 describes the experiment, which is a coincidence measurement setup in which the arrival times of the simultaneously generated photons are analyzed using two independent interferometers [69]. Due to reasons explained later in the chapter, pump pulse width has to be longer than the path-length imbalance of the interferometers, which in turn has to be longer than the timing jitter of the detectors. The generated energy-time correlated signal (photon 1) and idler (photon 2) pairs are at $\lambda_s \approx 1546.5$ nm and $\lambda_i \approx 1576.5$ nm, respectively (generation probability = 6.7×10^{-4} pairs/pump pulse). The chip temperature was stabilized at 30.2 °C. Photons at the output of the chip were spectrally separated using a three-port add/drop filter. After further filtering for pump rejection, the filtered bandwidths of the photons were about 0.6 nm (76 GHz) for λ_s and about 1.0 nm (122 GHz) for λ_i. Note that it would have been preferable to use two filters of same bandwidth, wide enough to capture the entire photons spectra, but despite extensive search, we were unable to find telecom components complying with our requirements. In both the arms, collective insertion loss from cascaded filters was about 6 dB each.

The photons were input into two separate Mach-Zehnder interferometers (MZIs). One arm of each MZI was made of polarization maintaining fiber (long arm) and the other of free-space polarization-maintaining optics elements (short arm), with an optical path-length difference ΔL = 56.55 cm. Equivalently, the

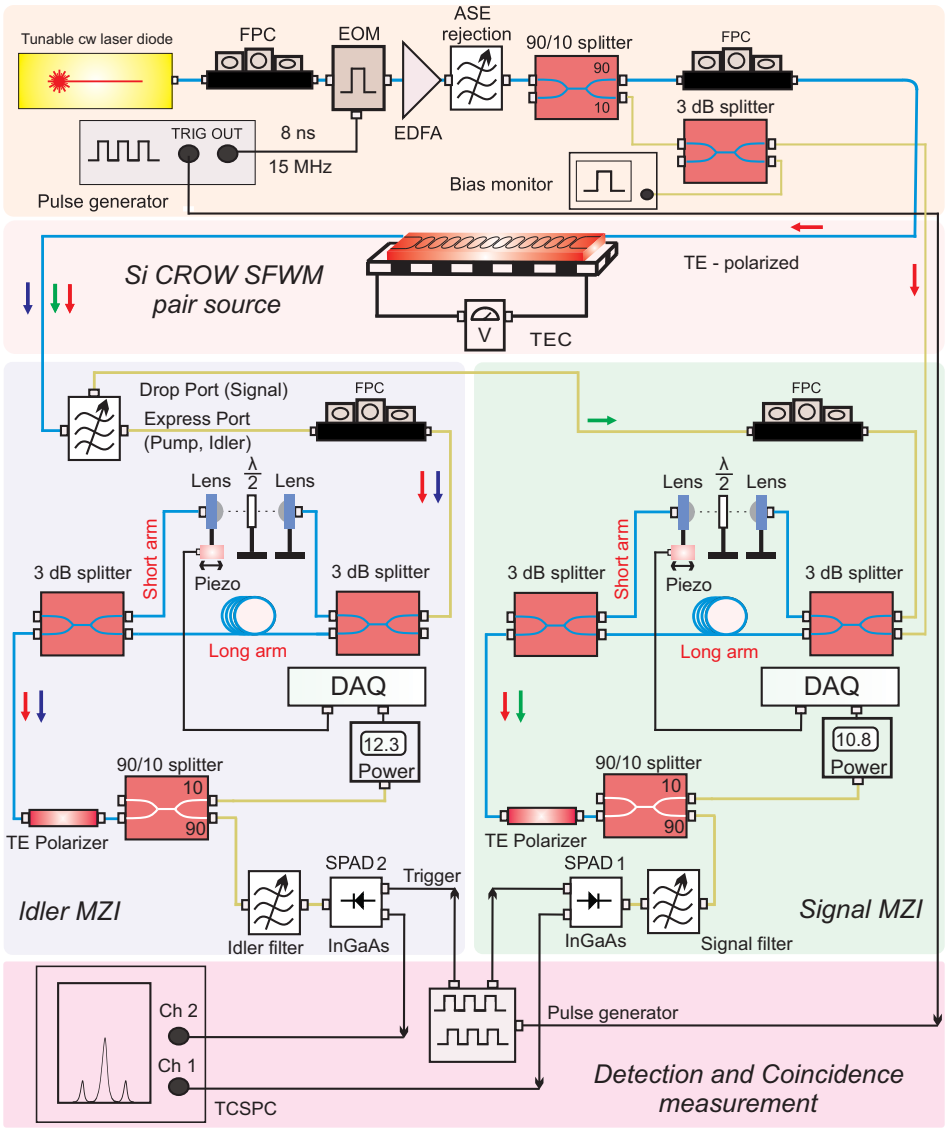

Figure 4.1: Photon pair generation using diode-pumped SFWM and entanglement characterization measurement through Franson interferometry. Two separate Mach-Zehnder interferometers (MZIs) were constructed, and separately stabilized using feedback based on transmission of the classical pump light. Blue lines refer to polarization-maintaining single-mode fiber and green lines to non-polarization-maintaining single-mode fiber.

path-length difference corresponds to a time delay $\Delta\tau = 1.88$ ns, which is indeed greater than the typical timing jitter (0.5 ns) of the off-the-shelf InGaAs SPADs used here. The two MZIs were matched carefully: the *difference* between the (long arm – short arm) imbalances of the two interferometers was less than 0.16 cm,

verified by time-of-flight measurements.

Each free-space path-length was actively (and separately) stabilized by using a piezo-actuated positioner under computer control using feedback from a power-level measurement of the classical pump light which was fed through the interferometers. Using error propagation calculations on the dependence of MZI output power with the arm imbalance (phase difference), the stability of the MZI was calculated to be about ± 0.1 radian, indicating that the length of the MZI variable arm was stabilized within about ± 25 nm relative to the fixed arm. During the measurements of visibility, the *signal* MZI was scanned, whereas the *idler* MZI was held stationary.

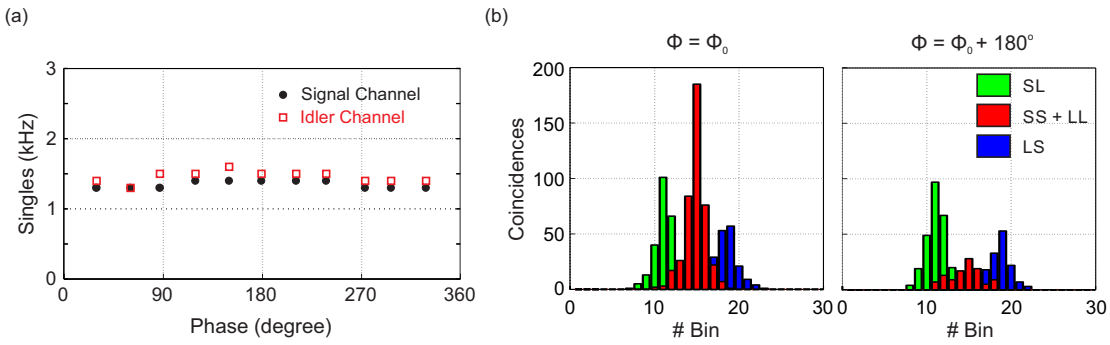

Figure 4.2: Full Franson Interferometer: (a) Singles from SPAD 1 (Signal) and SPAD 2 (Idler). (b) Output of the TCSPC for three gate configurations (corresponding to the SL, SS+LL and LS events) for two different interferometer phases ($\Phi = \Phi_0$ and $\Phi = \Phi_0 + 180°$). Each bin represented here is of 400 ps in width and the measurement time was 900 seconds for each events.

The insertion loss of each MZI was 7 and 8 dB respectively, including ~1dB excess loss at each of the input and output ports of the 50%/50% splitters, ~3 dB loss at the fiber collimators, ~1.5 dB excess loss at the fiber TE polarizer and ~1 dB excess loss at the output 90%/10% coupler. In order to maintain a good signal-to-noise ratio for our coincidence measurements, we matched the singles rate of the two SPADs by balancing their respective quantum efficiencies in order to compensate for the insertion loss difference, as seen in Fig. 4.2(a). These loss values could be reduced in the future using an on-chip interferometric structure; however, the timing jitter of the InGaAs SPADs required that the MZI arm-length imbalance had to be about 56.55 cm (in air), and would require very low loss waveguides on

chip (e.g., 0.5 dB/cm loss in waveguides with refractive index approximately 4). In this experiment, we did not attempt to make such waveguides, although the state-of-art in silicon waveguide fabrication is already not too far off this goal, and the requirements are eased if the timing jitter of the SPADs can be reduced [74].

Photons were detected using InGaAs SPADs with an estimated 15% quantum efficiency and a gate width of 2.5 ns. The measured dark counts were 310 Hz and 115 Hz, for detector 1 and 2, respectively. Coincidence measurements were performed with a TCSPC board (TimeHarp 260 PICO) over a period of 900 seconds, by cumulatively adding the contributions of 10 bins of width 100 ps.

4.2 Results and Discussion

In each MZI, a photon (labeled '1' or '2') can take two equally-probable paths, short (S) or long (L), leading to four possible scenarios for the coincidence events measured at the TCSPC: $|S_1L_2\rangle$, $|S_1S_2\rangle$, $|L_1L_2\rangle$, and $|L_1S_2\rangle$. In the case of $|S_1L_2\rangle$ and $|L_1S_2\rangle$, since the two photons have acquired a relative time lag larger than the two photon correlation time, they are distinguishable from each other as well as from $|S_1S_2\rangle$ and $|L_1L_2\rangle$. For the remaining two processes, the intrinsic uncertainty in the emission time of a photon pair within the duration of a pump pulse makes them indistinguishable from each other – pump pulse width larger than the path length imbalance also ensures indistinguishability of the detected photons. Thus, the bi-photon state $|\Psi\rangle$ reaching the detectors can be written as $|\Psi\rangle = \frac{1}{\sqrt{2}}\left(|S_1S_2\rangle + |L_1L_2\rangle\right) = \frac{1}{\sqrt{2}}\left(|S_1S_2\rangle + e^{i\Phi}|S_1S_2\rangle\right)$, where $\Phi = \phi_1 + \phi_2$, with ϕ_1 and ϕ_2 being the phases of *signal* and *idler* MZI, respectively. The associated coincidence rate should exhibit an interference pattern, which should go from constructive to destructive for a phase change $\Delta\Phi = \pi$, as verified in Fig. 4.2(b). The incomplete disappearance at $\Delta\Phi = \pi$ is attributed towards the background accidentals count. The path-length imbalance of the interferometers greater than detector's timming jitter ensures distinct SL, SS+LL, LS peaks.

There are several factors that contribute towards the accidentals counts, as observed in other reports [23, 25, 26, 28, 40, 71–73, 75–78], such as the amplified

spontaneous emission of the pump leaking through the filters, the detector dark counts and the propagation losses encountered by the photon pairs in propagating from the output of the chip to the detectors via the filters and interferometers, which can cause broken pairs and thereby result in start-stop pair counting between separated time slots, rather than coincidences. We operated our device at a pair-generation rate of approximately 10 kHz (without scaling for the duty cycle of the pump pulses, or approximately 83 kHz after multiplying by the duty cycle of the pump).

The path imbalance $\Delta\tau \gg \tau_{\mathrm{p}}$ (single-photon coherence time) ensures no single-photon interference events [69, 70]. Here, the single photon coherence time was estimated through the bandwidth ($\Delta\nu$) of the detection filter: $\Delta\nu \approx 0.8$ nm at 1550 nm implies $\tau_{\mathrm{p}} \approx 10$ ps $\ll 1.88$ ns. Fig. 4.2(a) confirmed the absence of single-photon interference through the independence of the singles rate on Φ for both the SPADs. We also verified the independences of $|\mathrm{S_1L_2}\rangle$ and $|\mathrm{L_1S_2}\rangle$ coincidence counts over the same variation.

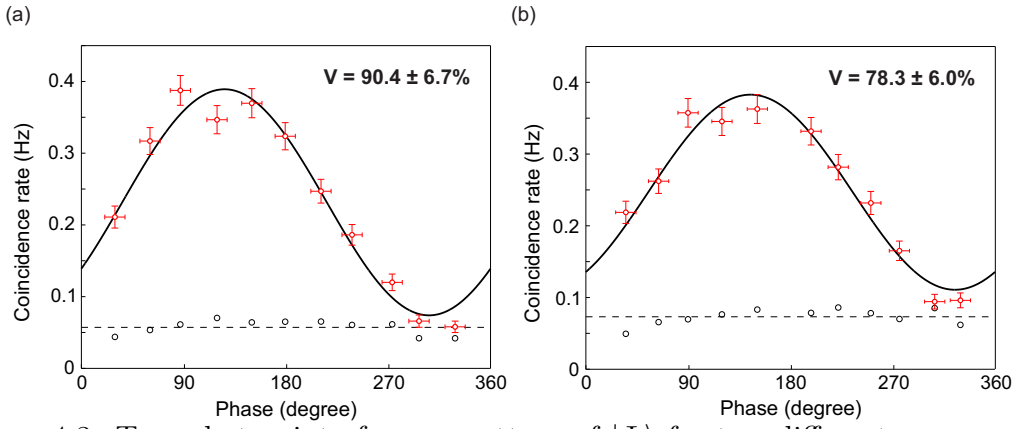

Figure 4.3: Two photon interference pattern of $|\Psi\rangle$ for two different pump wavelengths: (a) 1561.64 nm, (b) 1561.86 nm. These wavelengths correspond to adjacent transmission resonances within a single passband of the device. Red circles = experimental coincidence data, Black solid curve = Fit to the experimental data, Black dashed line = Average accidentals, Black circles = Individual accidentals.

The cumulative value of the counts under the central peak shown in red in Fig. 4.2(b) was measured as the MZI phase of the *signal* interferometer was varied. The measured data were assumed to have an error bar of magnitude $\sqrt{\mathrm{N}}$, N being the number of coincidences measured during 900 seconds. The phase

(horizontal axis) was inferred from the transmission of the classical pump light beam, using the standard power-versus-phase-imbalance relationship of a MZI. A fitting procedure, based on the Levenberg-Marquardt non-linear least-square curve fitting algorithm, confirmed the sinusoidal variation of coincidences with phase, as shown in Fig. 4.3. Each set of measurements took about 4 hours, over which time we could maintain the stability of both the MZIs, and of the input pump pulse-train in power and polarization, and both input and output chip-fiber couplings. An average value of accidentals, averaged over all the phase values, was subtracted from the measured coincidences, as shown by the dotted lines. A two-photon interference pattern fringe visibility $V \geq 70.7\%$ implies that the generated pairs are quantum-mechanically correlated, i.e., entangled [79], without necessarily providing a test of local realism. In Fig. 4.3, we show V in excess of this threshold value for two adjacent spectral peaks in the transfer function of the device after subtracting the accidentals (the raw V without subtracting accidentals are 68.1±5% and 55.1±4.2% for Fig. 4.3(a) and Fig. 4.3(b), respectively).

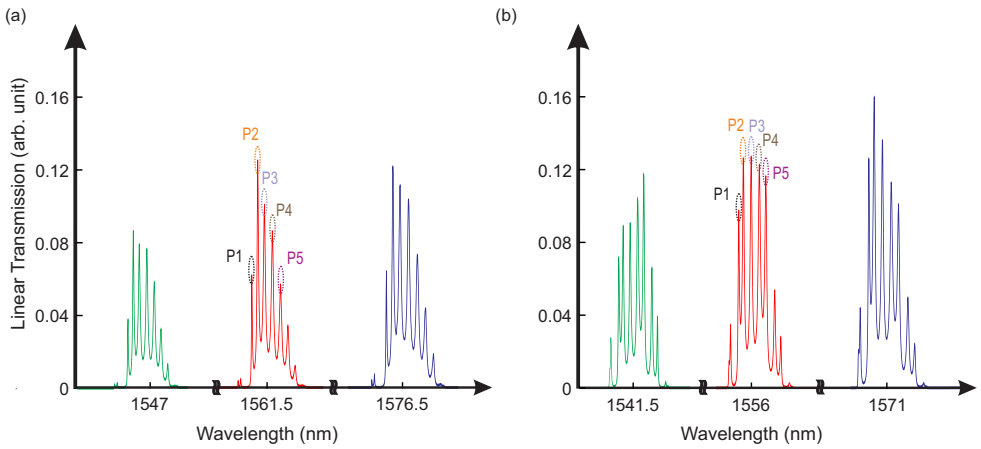

Figure 4.4: Classical transmission for 11 ring CROW. Signal, Idler, and Pump passbands are shown in green (left), blue (right), and red (center), respectively. The most prominent central five peaks are labeled as P1 - P5. (a) Chip used for full Franson measurement. (b) Chip used for folded Franson measurement.

In Fig. 4.3, the pump wavelength was aligned to two adjacent peaks of the transmission spectrum which were separated by 0.2 nm. This range of wavelength tuning is equivalent to varying the chip temperature by 7°C. The presence of

multiple transmission peaks in the passband of the coupled-resonator structure makes it possible to vary the pair generation properties by tuning to a nearby peak that is only 0.2 nm away. In contrast, a single microring device would have to tune by at least one-half of the FSR, which corresponds to changing the chip temperature by more than 40°C [75] before encountering another resonance.

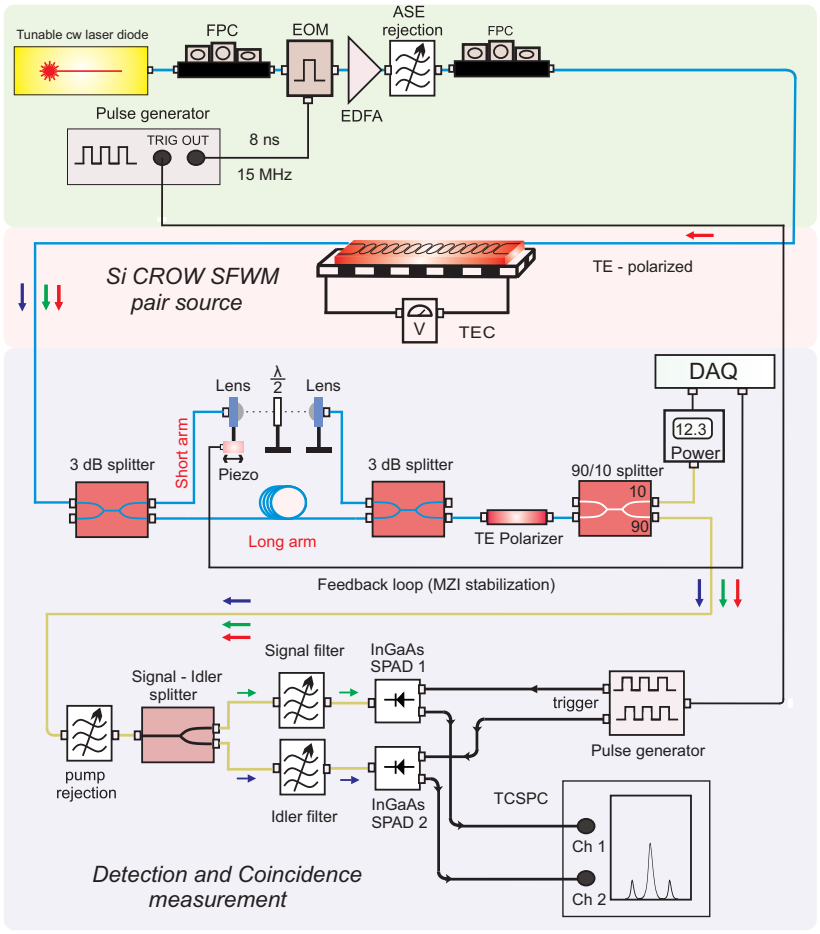

Figure 4.5: Photon pair generation using diode-pumped SFWM and entanglement characterization measurement through a folded Franson interferometry. Notice the simpler apparatus for stabilizing the interferometer, compared to Fig. 4.1.

The neighboring spectral peaks in the transmission spectrum are also expected to be useful in generating entangled photon pairs with visibilities $V \geq 70.7\%$. To confirm this, we used a folded Franson interferometer [80]: a simplified experimental setup, where both the photons go through a single MZI, as represented in Fig. 4.5. This experimental configuration is simpler to use and stabilize,

enables all the spectral filtering to be performed after the interferometer, and would

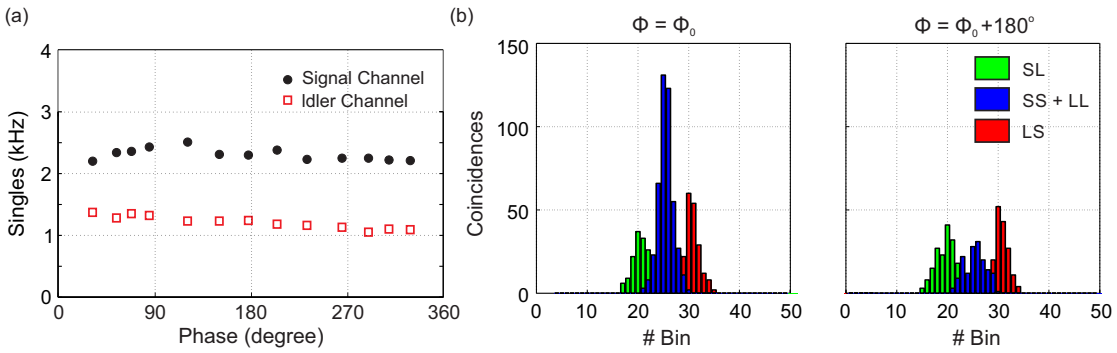

Figure 4.6: Folded Franson Interferometer: (a) Singles from SPAD 1 (Signal) and SPAD 2 (Idler). (b) Output of the TCSPC for three gate configurations (corresponding to the SL, SS+LL and LS events) for two different interferometer phases ($\Phi = \Phi_0$ and $\Phi = \Phi_0 + 180°$). Each bin represented here is of 300 ps in width and the measurement time was 900 seconds for each events.

occupy less space on a chip when integration is attempted in the future. The relative group delay shift accumulated between the 'signal' and 'idler' photons, separated in wavelength by about 30 nm, in propagating through a few meters of SMF-28e fiber was ignored in comparison to the SPAD timing jitter. The singles-versus-phase plot and coincidence binning plots for this set-up are shown in Fig. 4.6; in this case, the singles counts were not intentionally balanced as in the previous case. Because of mechanical damage to the chips during repeated and prolonged testing, we had to use a different device in these additional measurements, which had a similar, but not identical, transmission spectrum (Fig. 4.4). Nevertheless, when the pump wavelength was aligned within the passband to the same transmission peaks as used in Fig. 4.3, the measurement of interference patterns in the folded Franson interferometer shown in Fig. 4.7(c) and (d) resulted in values of V similar to those reported in Fig. 4.3. Since this experiment was easier to operate, involving one feedback-stabilized interferometer, rather than two, we also measured V for two other transmission resonances of the pump, as shown in Fig. 4.7(a) and (b). We believe that there is a relationship between the two-photon interference visibilities, V, and the two-photon JSIs measured in previous chapter [81], but have not fully investigated the connection yet.

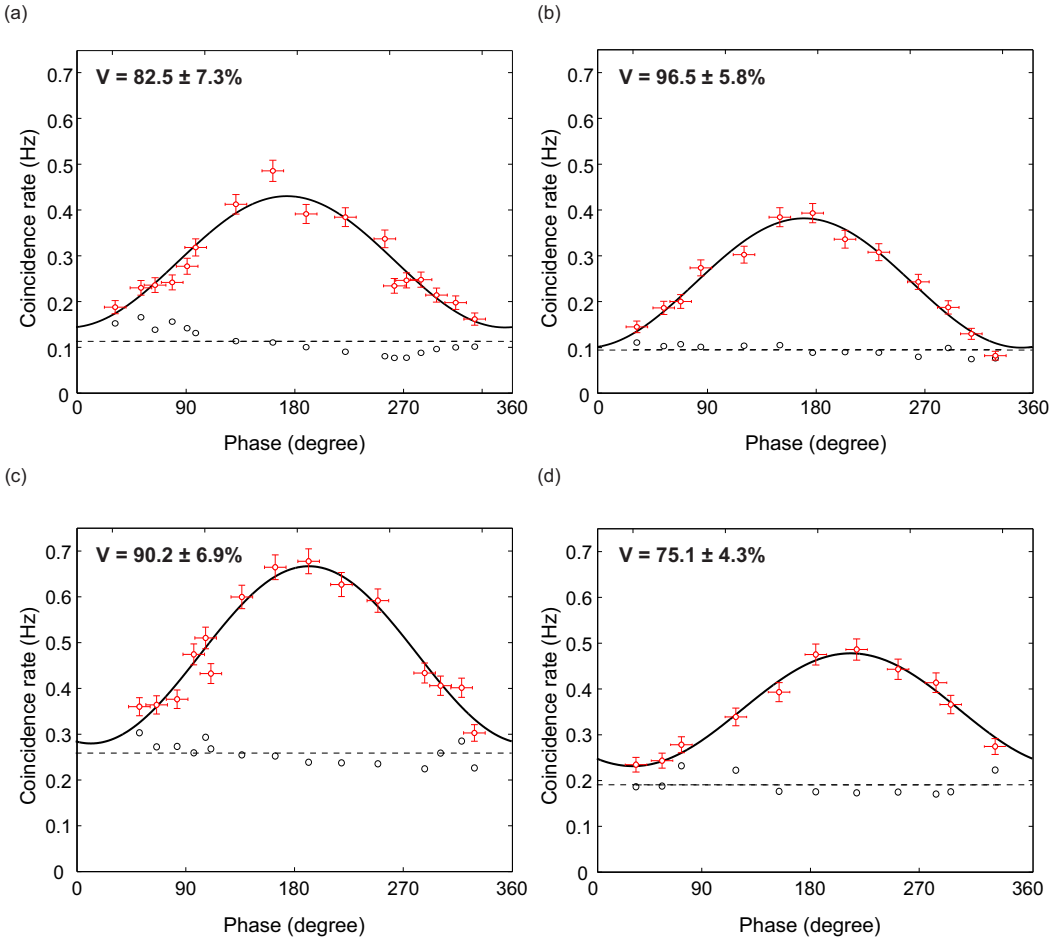

Figure 4.7: Two photon interference pattern of $|\Psi\rangle$ for four different pump wavelengths: (a) 1555.66 nm, (b) 1555.99, (c) 1556.21 nm, and (d) 1556.39 nm. These wavelengths correspond to transmission resonances within a single passband of the device. Red circles = experimental coincidence data, Black solid curve = Fit to the experimental data, Black dashed line = Average accidentals, Black circles = Individual accidentals.

4.3 Summary

In summary, this chapter shows the two-photon (Franson) interference of spectral lines of photon pairs generated using a silicon photonic chip at room-temperature, pumped by only a few milliwatts of optical pump power, and using commercially-available thermo-electrically cooled InGaAs SPADs at 234K. We have reported measurements of time-energy entangled photons using both unfolded

and folded Franson interferometers. Taken together, these results suggest it may be possible to realize an inexpensively-fabricated, chip-scale entangled photon pair source with low tuning power consumption, integrated with an entanglement monitor operating at a modest cooling budget, which may be useful for practical applications.

Chapter 4 contains material, reproduced in part with permission, from Ranjeet Kumar, Marc Savanier, Jun Rong Ong, and Shayan Mookherjea, "Entanglement measurement of a coupled silicon microring photon pair source" Optics Express Vol. 23, Iss. 15, pp. 19318–19327 (2015). Copyright 2015, Optical Society of America. The dissertation author was the primary author of this paper.

Chapter 5

Photon Pair Generation in Microring Resonators

CROW promises to be a better device, both in terms of pair generation rate and ease of control over the bi-photon spectrum, compared to a single microring resonator; but unlike a single microring, CROW is a more complicated device to design and fabricate. One such example was discussed in Chapter 3 for CROW with 11 microring resonators (Fig. 3.3). Error in fabrication results in different coupling coefficient than intended between the feeder waveguides and the first/last microring resonators (that is, imperfect apodization). Single microring resonator based sources also have smaller footprints on the chip. This matters more when it is required to multiplex several pair sources. For example, a few dozen multiplexed non-deterministic sources with heralding detectors, used concurrently with an active optical switching networks has the potential to operate as a quasi-deterministic single photon source with high emission probability [82].

5.1 Pair Generation: Theoretical

Unlike in straight waveguide, once the light enters a microring resonator, it circulates for multiple round-trips before exiting. In a traveling-wave picture, due to circulation of the fields in a microring resonator, non-linear optical interactions between modes coherently build up intensities over an increased interaction length,

which can also be seen as the resonator length multiplied by the number of round trips made by the resonant photons – dictated by the 'photon lifetime' in the resonator. Using the transfer matrix model of propagation for a waveguide-coupled microring resonator [83], ring resonator can be "unfolded" into a straight waveguide, and can be shown that both the interaction length and circulating optical powers are scaled by the resonator finesse ($\mathcal{F}$). Hence, Eq. 2.1 can be modified to include the effect of finesse such that the pair generation rate in microring becomes:

$$r = \Delta\nu \left[\gamma \mathrm{P}_0^{res}(\lambda)\mathrm{L}_{eff}^{res}\right]^2 \mathrm{sinc}^2\left[\beta_2 \left(\Delta\omega\right)^2 \frac{\mathrm{L}^{res}}{2} + \gamma \mathrm{P}_0^{res}\mathrm{L}_{eff}^{res}\right] \tag{5.1}$$

where $\Delta\nu$ is the resonance line-width, defined as $\Delta\nu = c/(\lambda_p Q)$, Q is the quality factor of the resonator, $\gamma,\ \Delta\omega$ & β_2 are defined in Chapter 2, and the superscript res indicates the resonantly enhanced following quantities:

$$\begin{aligned} \mathrm{P}_0^{res}(\lambda) &= \mathrm{P}_0 \times \frac{\mathcal{F}}{\pi} \times \frac{\left(\lambda_p/2Q\right)^2}{\left(\lambda - \lambda_p\right)^2 + \left(\lambda_p/2Q\right)^2} \\ \mathrm{L}^{res} &= \mathrm{L} \times \frac{\mathcal{F}}{\pi} \\ \mathrm{L}_{eff}^{res} &= \frac{1 - e^{-\alpha \mathrm{L}}}{\alpha} \times \frac{\mathcal{F}}{\pi} \end{aligned} \tag{5.2}$$

where $\mathcal{F} = Q\lambda_p/(n_g \mathrm{L})$, n_g & α are defined in Chapter 2 and $\mathrm{L} = 2\pi\mathrm{R}$, where R is the radius of the ring resonator. The monochromatic pump wavelength λ is assumed to be positioned close to the ring resonance wavelength λ_p. It is apparent from Eq. 5.1 and Eq. 5.2 that the Q is an important parameter for pair generation in a ring resonator. Q combines the contribution of two loss mechanism: (1) propagation loss and (2) coupling to the bus waveguide. The loaded Q of the ring can be expressed as [84]:

$$\begin{aligned} Q_L &= \frac{\pi}{2\sin^{-1}\left(\frac{1-a\tau}{2\sqrt{a\tau}}\right)} \frac{n_g \mathrm{L}}{\lambda} \\ &\underset{a\tau \to 1}{\approx} \frac{\pi\sqrt{a\tau}}{1 - a\tau} \frac{n_g \mathrm{L}}{\lambda} \end{aligned} \tag{5.3}$$

where $a = \exp(-\alpha \mathrm{L}/2)$ is the round-trip field attenuation, and $\tau^2 = 1 - |\kappa|^2$ is the (path-integrated) coupler intensity transmission coefficient, with $|\kappa|^2$ being the

path-integrated coupling coefficient which appears in the popular matrix formulation of the waveguide-ring model [83].

For an isolated resonator ($\tau = 1$), the unloaded Q is dominated by loss and represents the intrinsic Q limit. In the low-loss regime, it can be expressed as:

$$Q_U = \frac{2\pi n_g}{\lambda\alpha}. \tag{5.4}$$

In the case where the loaded quality factor is dominated by the coupling coefficient in the low-$|\kappa|^2$ limit, Q is given by:

$$Q_{\text{cpl}} = \frac{2\pi n_g L}{\lambda|\kappa|^2}. \tag{5.5}$$

It should be noted that n_g, α, and the GVD coefficient (β_2) depend on the waveguide cross-section, and $|\kappa|^2$ depends on the gap between input bus waveguide and the microring.

5.1.1 Design Parameters

The silicon waveguide, with a cross-section that is approximately 525 nm wide and 226 nm tall [85], supports a single optical mode in the transverse electric (TE) and transverse magnetic (TM) polarizations, and the latter can be excluded from participating in the transmission resonances not only by injecting the optical input in the TE polarization, but also by relying on the higher bend loss of the TM mode compared to the TE mode [86]. Though making waveguides narrower can help remove unwanted modes, but this results into higher group-velocity dispersion (4400 ps/nm-km) [85], and incurs a significant optical propagation loss (typically 2–4 dB/cm) [86, 87], both of which can negatively impact pair generation.

Our waveguide cross-sections, shown in Fig. 5.1(b) have a more favorable GVD coefficient, calculated to be -1040 ps/nm-km (B = 220 nm) or -110 ps/nm-km (B = 340 nm) at a wavelength of 1550 nm. Test waveguides similar to those used to form the microring resonator were measured using an atomic force microscope to have a root-mean-squared sidewall roughness of 2.6 nm, and, using an optical cutback method, to have a propagation loss of -0.74 dB/cm (B = 220 nm) and -1.23 dB/cm (B = 340 nm) at 1550 nm.

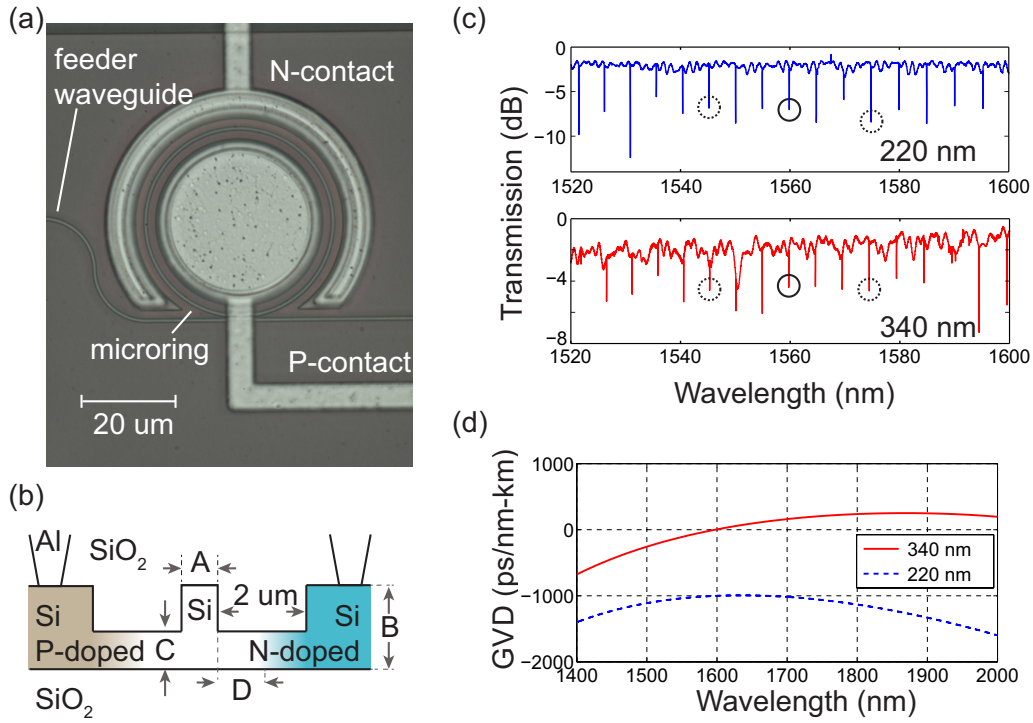

Figure 5.1: (a) Microscope plan view of a microring resonator with embedded *p-i-n* junction across the waveguide. (b) Cross-section schematic drawing; measured devices have A = 650 nm, B = 220 nm or B = 340 nm, C = 70 nm, D = 900 nm. (c) Transmission spectrum for B = 220 nm and B = 340 nm microring resonators (the solid circles indicate the chosen pump wavelengths, and the dotted circles the measured signal-idler wavelengths). (d) Group velocity dispersion (calculation) for the lowest-order TE modes of waveguides with the cross-section shown in panel (b).

Through standard microring theory [88], the resonant enhancement in a ring can be quantified through its quality factor (Q). In the absence of waveguide-ring coupling loss, the upper limit on the un-loaded Q has been estimated as $Q_U = 9.2 \times 10^5$ (B = 220 nm) and $Q_U = 5.6 \times 10^5$ (B = 340 nm). From the transmission measurement performed at low input power to prevent thermo-optic effect, our fabricated microring resonators were seen to have a (loaded) quality factor around 1×10^5 e.g., B = 220 nm microring with radius 20 μm: $Q_L \approx 9.5 \times 10^4$ and B = 340 nm microring with radius 20 μm: $Q_L \approx 2.5 \times 10^5$.

Eq. (5.3) shows the dependence of loaded Q on the experimentally accessible parameter: propagation loss α and the coupling coefficient $|\kappa|^2$. While α shall be as low as possible to increase the intrinsic Q_U, $|\kappa|^2$ can be selected by the designer

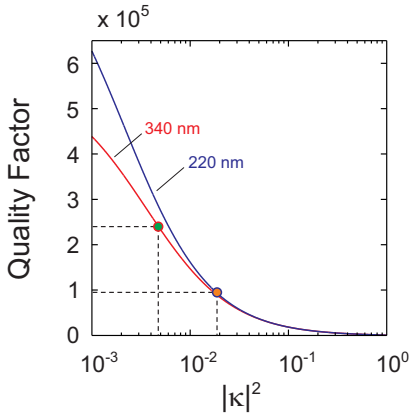

Figure 5.2: Nonlinear relationship between the loaded quality factor Q and the coupling coefficient $|\kappa|^2$, calculated using Eq. (5.3) and the parameters specific to the two structures studied here (B = 220 nm: blue, B = 340 nm: red). The $|\kappa|^2$ values for the fabricated devices are estimated from the measured loaded Q's (dots and dashed lines)

during the design stage. Fig. 5.2 explicitly shows the relation between Q_L and $|\kappa|^2$ for the microring devices presented above, based on the measured value of α and the simulated n_g (Lumerical software package). From $Q_L = 9.5 \times 10^4$ (B = 220 nm) and $Q_L = 2.5 \times 10^5$ (B = 340 nm), we inferred the respective coupling coefficients $|\kappa|^2 \approx 0.018$ and $|\kappa|^2 \approx 0.005$.

5.1.2 Microring-Waveguide Coupling Coefficient

The value of $|\kappa|^2$, the path-integrated coupling coefficient of the waveguide directional coupler formed between the feeder waveguide and the microring resonator [83], is determined by the width of the waveguides, the separation between them, and the length of the coupling region. It may not be easy to fabricate couplers such as shown in Fig. 5.1 accurately, and this can be a bigger problem when the desired value of $|\kappa|^2$ is very small, as is required for a high-Q resonator. When using waveguides that have a significant GVD with higher pump powers, small variations in $|\kappa|^2$ may cause large changes in the measured PGR.

Fig. 5.3 shows calculations of the PGR using Eq. (5.1) for different values of $|\kappa|^2$. Since we are especially interested in small values of $|\kappa|^2$, the horizontal axis is plotted on a logarithmic scale. For these numerical calculations, we have used

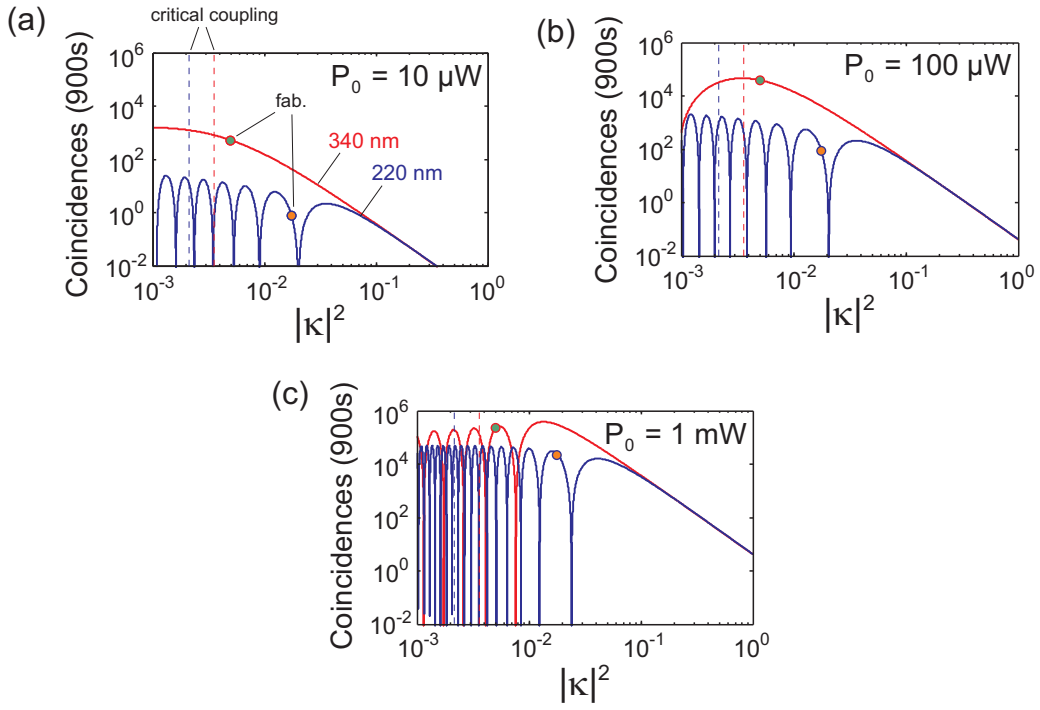

Figure 5.3: The appropriate choice of the coupling coefficient $|\kappa|^2$ is guided by numerical calculations of the coincidences counted in 900 s. A study of two cross-sections (B = 220 nm and 340 nm – blue and red curves, respectively) with increasing pump powers: (a) 10 μW, (b) 100 μW and (c) 1 mW, shows the critical role of GVD and self-modulation on the coincidences counts, through the SFWM phase-mismatch.

values for the fiber-waveguide coupling efficiencies, waveguide losses and detector parameters which are relevant to our experiment, but altering these values does not qualitatively change the following observations. The PGR does not grow indefinitely for small values of $|\kappa|^2$, as one would expect from an idealized model [89]. This is because the 'sinc' term in Eq. (5.1) decreases in magnitude if either P_0 or L increase. (Another effect, non-linear absorption, which has been studied elsewhere [90], would also limit the increase of PGR at high Q values.) For small values of $|\kappa|^2$ (i.e., under-coupled regime), the optical propagation length increases, and there are 'nulls' in the PGR (driven by the 'sinc' term). Practically, it may be safer to use larger values of $|\kappa|^2$ (i.e., the slightly over-coupled regime) to reduce the risk that small fabrication imperfections or temperature-dependent fluctuations would catastrophically lower the PGR. For slightly larger values of $|\kappa|^2$, to the right-hand

side of the optimum in Fig. 5.3, there are no nulls, since the argument of the 'sinc' term is small. The circles indicate the values of $|\kappa|^2$ used in our devices. These nulls are obviously much more of a factor if the pump power is increased. The benefit of the lower GVD of the B = 340 nm waveguide (red curve) is evident, compared to the 220 nm tall waveguide (blue curve).

It should be noted that these behaviors are relevant for weak waveguide-resonator coupling or lower values of $|\kappa^2|$, i.e. once the Q factor of the microring exceeds a reasonably high value – around 10^5 for typical GVD of Si waveguides, see Fig. 5.2 – and may not be relevant for lower-Q microrings (see Table 5.1). The PGR scales as the cube of Q and in the search to improve PGR by achieving higher Q, these effects will undoubtedly become critically important.

Critical coupling is another important discussion for a ring resonator, because at critical coupling, maximum amount of input optical pump power is delivered at resonance wavelength. Designing a ring resonator at critical coupling is beneficial because the maximum input optical pump power is delivered to the resonator, and the transmission of the residual pump power past the microring is minimized. Any assistance in extinguishing the pump that can be provided by critical coupling helps filtering, since on-chip silicon photonic filters do not provide as much on-off contrast as off-chip assemblies. In silicon microrings formed using low-GVD waveguides, the value of $|\kappa|^2$ that achieves critical coupling is, in fact, close to the value of $|\kappa|^2$ which optimizes PGR at low pump powers. The critical coupling for two relevant different waveguide heights are shown in Fig. 5.3, through vertical dashed line. Fig. 5.3 also show that our experimentally-fabricated couplers (circles) achieved values of $|\kappa|^2$ that were close to, and slightly above, critical coupling (dashed red and blue lines). Due to fabrication imperfection, it is difficult to obtain the designed κ values, and in fact, through finite-difference time-domain simulation done through Lumerical software, we found that our waveguide-ring gap has an error of 43 nm for the B = 220 nm ring, and 16 nm for the B = 340 nm ring. Tunable directional coupler, in principal, can solve this discrepancy but they tend to be too long for devices like compact microring.

5.2 Pair Generation: Experimental

The micro-resonator was optically pumped in the experimental setup similar to the one described in Chapter 2. Single photons at signal and idler wavelengths were detected using gated InGaAs SPADs with an estimated 15% quantum efficiency, electrically-generated gate width of 2.5 ns and gating repetition frequency 5 MHz [91]. The dark counts of the two SPADs were 70 Hz and 130 Hz. For a representative microring used in this chapter (B = 220 nm, R = 20 μm), the intensity enhancement factor (ratio of the circulating field intensity in the microring to the intensity in the feeder waveguide) was 173. Thus, in the low pump power regime, an input waveguide power of -10 dBm resulted in a circulating field intensity in the microring of about 9.3 MW.cm^{-2}. The associated two-photon absorption in silicon was calculated to be 0.02 dB/cm, i.e. more than one order of magnitude smaller than the reported linear propagation loss.

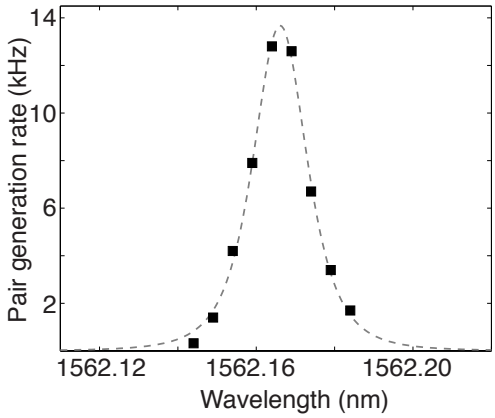

Figure 5.4: Measurements of PGR as the pump wavelength was finely tuned across the resonance (the error bars are smaller than the markers); input pump power was approximately -10 dBm. The dashed line is a squared-Lorentzian fit, consistent with Eq. 5.1 and 5.2

Fig. 5.4 shows the PGR vs pump wavelength for one resonant peak. As one would expect from Eq. 5.1 & 5.2, the PGR peaks when the pump is spectrally aligned to the resonant wavelength of the microring (B = 220 nm, R = 10 μm). The measurement was done using continuous-wave pump with SPADs gated 50 MHz with 2.5 ns gate width. Low input pump power ensured negligible self-phase

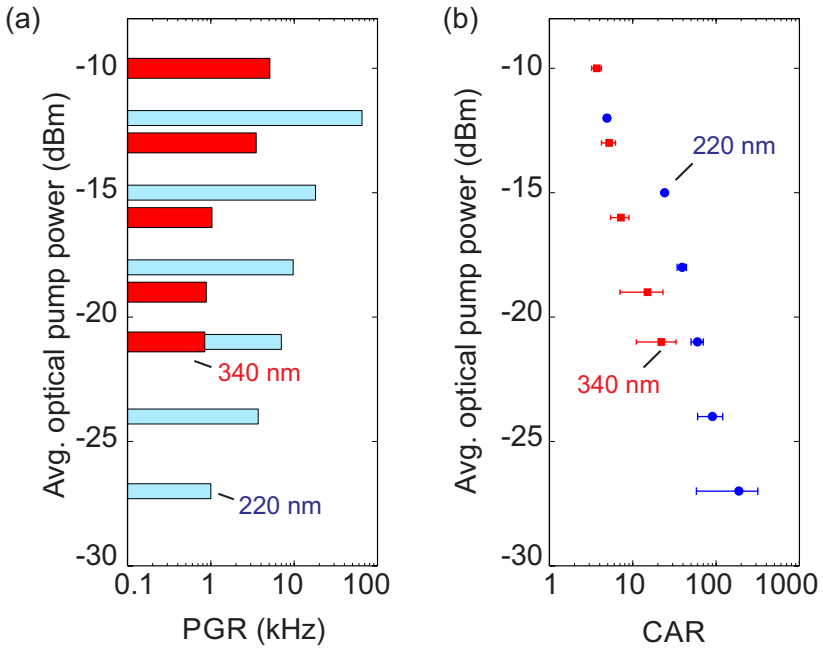

Figure 5.5: (a) Measured PGR using pump pulses of 3 ns duration at a repetition rate of 5 MHz (the error bars are too small to be visible) and (b) CAR versus average optical pump power in the feeder waveguide.

modulation (second term in the sinc[$\cdots$] of Eq. 5.1) and hence, constant value for 'sinc'. Using Eq. (5.1), the dashed line shows a fit of a squared-Lorentzian functional form, since the field generated by SFWM is proportional to the square of the circulating pump field. When pumped with -11 dBm of optical power in the feeder waveguide at $\lambda_p = 1562.16$ nm, the photon pairs were generated at $\lambda_s = 1542.61$ nm and $\lambda_i = 1582.24$ nm with a generation probability of about 2×10^{-4} pairs/detector gate.

Fig. 5.5(a) shows the PGR measurements of R = 20 μm radii devices for B = 220 nm and B = 340 nm. The experimental PGR are calculated from the measured coincidence rates at the detectors after factoring out the chip-to-fiber coupling loss (3 dB), the off-chip filter losses (6 dB for signal and 5 dB for idler) and detector quantum efficiencies (15%). The CAR is plotted in Fig. 5.5(b). The improvement in CAR at lower pump powers (and thus, at lower PGR) has been briefly discussed in Chapter 2, as well as reported and discussed extensively in the literature [23–25, 28, 40]. To find the on-chip "intrinsic" PGR, we further scaled

the PGR by the duty cycle of the SPADs, and it is shown in Fig. 5.6.

5.3 Discussion

The intrinsic PGR values shown in Fig. 5.6 are still several orders of magnitude below what theory predicts. In the ideal case, where the SFWM process is perfectly phase-matched (i.e., 'sinc' is unitary), we calculated that the two microring resonators studied here would result in PGR = 3.6 GHz (B = 340 nm) and PGR = 329 MHz (B = 220 nm) at P_0 = 530 μW. One possible reason for this deviation could be the dependence of coincidence count on the precise value of $|\kappa|^2$, as discussed before.

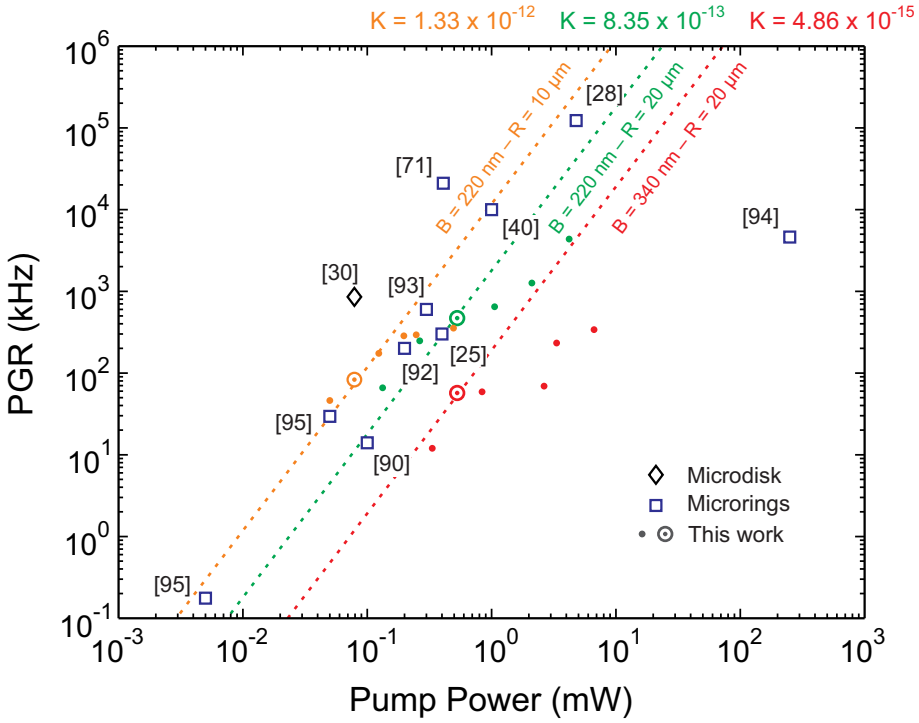

Figure 5.6: Measured on-chip PGR versus average optical pump power (P_0) for the devices presented here (dots), along with the recent experimental reports of Table 5.1 in microrings (squares), and microdisk (diamond). The quadratic dependence of PGR with P_0 is highlighted by the fits PGR = $KQ^3/R^2 \times P_0^2$ of each experimental dataset at low pump power (dashed lines), while saturation occurs at higher pump powers.

Our values of $|\kappa|^2$ (marked 'fab.' in Fig. 5.3) were estimated from the measured linewidth of the resonance, assuming that the waveguide propagation loss

coefficient which was measured on separate test structures (paperclip waveguides) also represents the loss coefficient of the (curved) waveguides in the microring, and there are no additional losses (e.g., in the coupler). If these assumptions are not valid then the estimated value of $|\kappa|^2$ would be different. However, if we assume that our estimation of $|\kappa|^2$ is accurate, then Eq. 5.1 predicts that our microrings should exhibit PGR = 10.8 MHz (B = 340 nm) and PGR = 8.6 MHz (B = 220 nm). These PGR values are already much smaller than the ideal, phase-matched cases which ignore the 'sinc' term in Eq. 5.1. Moreover, as Fig. 5.3 shows, small errors in fabrication can further reduce PGR catastrophically if we happen to fall into one of the nulls of the argument, which are closely spaced at higher pump powers. Thus, in practice, the PGR depends critically on the microring-waveguide coupling coefficient, especially when GVD is non-zero and low $|\kappa|^2$ values are targeted. Reducing the pump power mitigates these impairments somewhat, but also results in a less bright pair source.

Based on Eq. 5.1 in the low-loss approximation, we also fitted the experimental data at low optical power following $\mathrm{PGR} = \mathrm{K}Q^3/\mathrm{R}^2 \times \mathrm{P}_0^2$. The quadratic behavior was seen to hold for in-coupled pump power up to $\approx$ 100 μW (R = 10 μm) and $\approx$ 500 μW (R = 20 μm), above which the PGR saturated. In general, pair generation in microrings operating at high pump power is hampered by nonlinear effects triggered by high circulating power (e.g., two-photon absorption, free-carrier absorption/dispersion, thermal shift). Fig. 5.6 also confirms the dependence of PGR on the microring radius R. Generally, microring resonators with smaller radii are more efficient at generating pairs, as has already been discussed in Ref. [92].

The *p-i-n* junction diode fabricated across the waveguide ridge, as shown in Fig. 5.1, was done for the purposes of sweeping out optically-generated free-carriers and thus improving the PGR, following the report of Ref. [28]. However, despite careful study, we were unable to prove this effect in any of our large ensemble of chips. Instead, the diode performed a different, and very useful, purpose of providing an electronic readout (essentially, a Ge-free photodiode) for aligning the pump laser to the microring – discussed in the next chapter.

Table 5.1: Recent results of photon pair generation using silicon microring resonators, including recent microdisk result

Ref.	Dimensions[(a)]	Radius	Q	GVD	PGR	⟨Pump power⟩	CAR
Clemmen et al. [25]	500×200 nm	6.8 μm	4.5×10^4	-0.7 $ps^2.m^{-1}$	300 kHz	400 μW	30
Azzini et al. [92]	500×220 nm	5 μm	7.90×10^3	-	200 kHz	200 μW	250
Engin et al. [28]	$450 \times 220 \times 50$ nm	11 μm	3.75×10^4	-	123 MHz	4.8 mW	37[(b)]
Harris et al. [93]	500×220 nm	15 μm	4×10^4	-	600 kHz	300 μW	50
Silverstone et al. [94]	500×220 nm	15 μm	9.2×10^3	-	4.6 MHz	150 μW[(b)]	10
Guo et al. [90]	$450 \times 220 \times 60$ nm	21 μm	8.1×10^4	-	14 kHz	100 μW	180
Grassani et al. [40]	500×220 nm	10 μm	1.5×10^4	-	10 MHz	1 mW	65
Wakabayashi et al. [71]	400×220 nm	7 μm	2×10^4	-	21 MHz	410 μW	352
Gentry et al. [95]	$1080 \times$ sub-100 nm	22 μm	3.1×10^4	-	165 Hz	5 μW	37
					29 kHz	50 μW	55
This work	$650 \times 340 \times 70$ nm	20 μm	2.5×10^5	+0.14 $ps^2.m^{-1}$	57 kHz	8 μW[(c)]	22
This work	$650 \times 220 \times 70$ nm	20 μm	9.5×10^4	+1.33 $ps^2.m^{-1}$	470 kHz	8 μW[(c)]	60
This work	$650 \times 220 \times 70$ nm	10 μm	9.6×10^4	+1.33 $ps^2.m^{-1}$	83 kHz	79 μW	65
Jiang et al. [30]	[Micro-disk]	5 μm	5×10^5	-	855 kHz	79 μW	274

[(a)] With references to Fig. 5.1(b): $A \times B \times C$. [(b)] Peak power = 0.25 W. [(c)] Peak power = 530 μW.

5.4 Summary

Table 5.1 summarizes the advancement in the state-of-the-art in photon pair generation using silicon microring resonators at wavelengths near 1.55 μm. With these few-microwatt pump power pair-generation results, silicon microring resonators now approaching a performance regime previously only attainable using microdisk resonators [30], compared to which microrings have some advantages such as a cleaner mode spectrum, CMOS-compatible fabrication and waveguide coupling instead of suspended-fiber coupling. In this chapter, we found that compact silicon microrings with a radius of about 10 μm (or less, as long as the loss can be kept low), which are slightly over-coupled to the feeder waveguide and are operated at low pump power will come closest to the theoretical performance predictions. In fact, since these devices can be pumped with only a few tens of microwatts of average pump power to achieve hundreds-of-kilohertz rate (on-chip) PGR, it may even be possible to use on-chip microlasers to realize a fully-integrated chip-scale source of photon pairs.

Chapter 5 contains material, reproduced in part with permission, from Marc Savanier, Ranjeet Kumar, and Shayan Mookherjea, "Photon pair generation from compact silicon microring resonators using microwatt-level pump powers" Optics Express Vol. 24, Iss. 4, pp. 3313–3328 (2016). Copyright 2016, Optical Society of America. The dissertation author was one of the primary author of this paper.

Chapter 6

Optimization of Photon Pair Generation through PIN Diode

Silicon devices are prone to be affected with the change in ambient temperature due to high thermo-optic coefficient. In fact, in resonant devices such as microring resonator, self-heating can also be a problem. Resonators with high Q utilizes input pump power more efficiently and even a low optical power can heat the ring enough to have a red-shift in the transmission spectrum. Hence, the device must therefore be monitored, so that the pump wavelength can be adjusted when the temperature varies. Some of the work in this direction includes the use of on-chip Germanium [96] or AlGaInAs [97] photodetector for power monitoring, but in both of these cases, extra processing steps were required and that increases the cost and complexity of the device. In this chapter, we will discuss the incorporation of *p-i-n* junction diode in the silicon waveguide cross-section, as shown in Fig. 6.1, which can be conveniently fabricated in a silicon-only process. The current generated in the reverse-biased diode in the microring resonator is proportional to the circulating optical intensity of the pump field, implying this is not a two-photon absorption but is conjectured to be due to a phototransition of an electron from the valence band to a mid-bandgap state, and transitioning to the conduction band assisted by the electric field [98]. Reverse bias (typically, -1 V) results in a generated current of about 1 μA when the microring is generating photon pairs at a suitable operating point. Such a current is easily measurable

by low-noise integrated or off-chip electronics and is adequate for monitoring the resonance of the microring. This all-silicon "photodetector-in-a-microring" can be compared to the defect-based Si photodetector [99]; both schemes share the goals of monitoring the resonance without the use of III-V materials or germanium, but this scheme does not introduce lattice damage to the waveguides (which resulted in an additional propagation loss of 45 dB/cm [99], which would not be acceptable for photon pair-generation), and yet, achieves a higher measured photocurrent by a factor of 10. For monitoring without a built-in diode, an externally-biased conductance measurement of a microring resonator through capacitively-coupled metal contact pads has been recently reported [100].

6.1 Device Characterization

Device

The cross-section of the device is shown in Fig. 6.1(a). The p doped region was formed by implanting Boron (33 keV, 1×10^{15} cm^{-2}) and the n doped region was formed by implanting Phosphorous (90 keV, 1×10^{15} cm^{-2}). The edge of the implanted regions was 900 nm from the edge of the ridge. Additional shallow implants of Boron and Phosphorous were used below the metal (Aluminum) contacts. This waveguide cross-section supports two TE and one TM polarization but due to bending loss from the microring, only lowest order of TE polarization survives in the microring. Due to this, the transmission spectrum shows a clean, single-family set of resonance peaks, as shown in Fig. 6.1(c). The loaded quality factor (Q_L) was calculated to be 1.42×10^5, and based on the discussion from previous chapter the intrinsic (unloaded, loss-limited) quality factor (Q_U) was estimated to be 6.2×10^5. Also from the previous chapter, the propagation loss was estimated to be -0.74 dB/cm at 1550 nm.

Diode Characterization

The I-V relationship of the diode with no light in the waveguide but with some ambient illumination though microscope illuminator is plotted in Fig. 6.1(d).

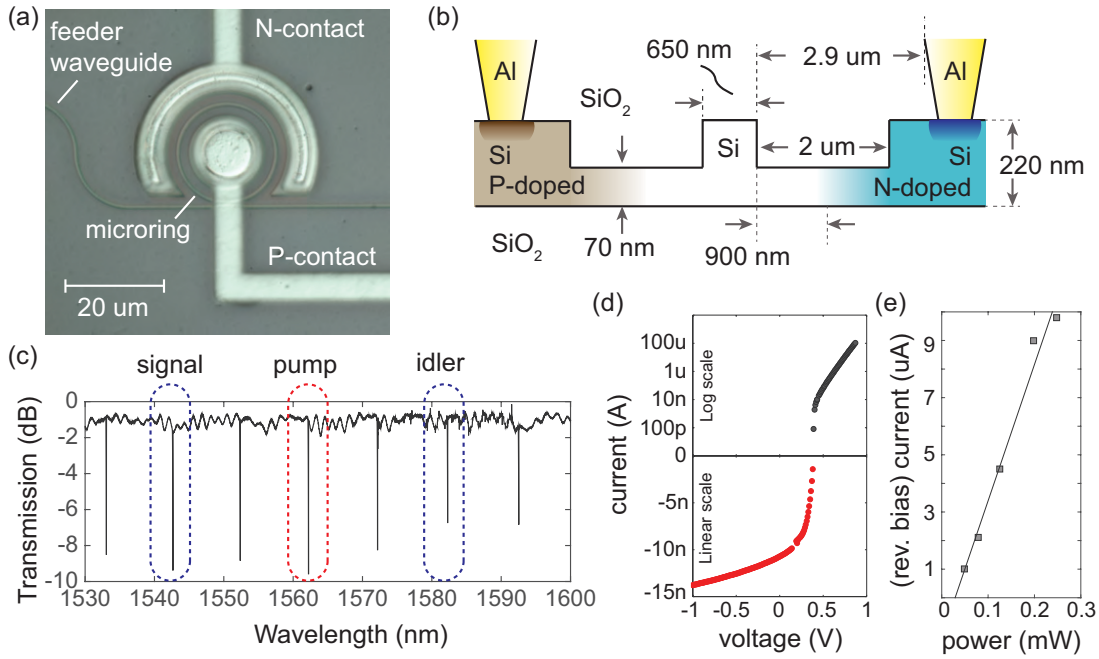

Figure 6.1: (a) Optical microscope image of a silicon microring, side-coupled to a waveguide, and with a *p-i-n* junction across the waveguide cross-section. (b) Schematic of the waveguide cross-section. (c) Optical transmission spectrum (arbitrary normalization); the dotted boxes indicate which resonances are used for the input pump and for the generated photon pair. (d) *I-V* measurement without light in the waveguide (under microscope illumination). (e) The magnitude of the reverse-biased current measured when light was guided in the feeder waveguide, and coupled into the microring, as a function of the optical power in the waveguide.

The ambient light helped generate small photo-current in the reverse-biased regime. Through fitting a measurement of dV/dI versus I, the contact resistance was inferred to be 44 Ω and diode ideality factor to be 1.81 – indicating that in the high forward-bias regime, the current was dominated by recombination in the depletion region (as expected). In an ideal "dark" reverse-biased junction, all mobile carriers should be removed from the junction volume; however, thermal excitation promotes electrons across the bandgap. In the reverse-biased condition, given the heavily-doped neutral regions (i.e., low carrier mobility in that region), the current is expected to be dominated by the carrier generation in the depletion region, with an estimated current density $J_R \sim qn_iW_d/\tau_g \sim 3$ mA.cm^{-2} where q is the electronic charge, n_i is the intrinsic carrier density of Si, W_d is the depletion width, and

τ_g is the generation carrier lifetime, estimated to be approximately 100 ps from carrier modeling using Silvaco software. Based on the microring geometry, the reverse-biased current (I_R) was estimated to be $\approx$ 440 pA. Though not shown in Fig. 6.1(d), I_R = 380 pA was measured at 25 °C at a bias voltage of -2 V, showing a good agreement with the calculation. $I_R \approx 15$ nA in Fig. 6.1(d) is due to halogen light from microscope. When continuous-wave laser light was guided in the waveguide, I_R was in the micro-ampere range as shown in Fig. 6.1(e). The effective responsivity at the wavelength of 1562 nm was 1.2×10^{-4} A.W^{-1}, referenced to the circulating optical power in the microring (consistent with the responsivity 1×10^{-4} A.W^{-1} measured at 1545 nm in an un-implanted silicon waveguide with p and n doped regions across it [98]). This responsivity is suitable for the reverse-biased junction current to be a suitable practical quantity to measure, with ample dynamic range headroom above the noise floor (either when dark or under normal room lighting), for the purpose of stabilizing photon pair generation.

6.2 Photon Pair Generation

The microring resonator was optically pumped using continuous-wave light in a setup similar to previous chapter, along with an addition of a current measurement on the reverse-biased diode. At a temperature of 30°C, when pumped with -11 dBm of optical power in the waveguide at λ_p = 1562.16 nm, the photon pairs were generated at λ_s = 1542.61 nm and λ_i = 1582.24 nm with a generation probability of about 2×10^{-4} pairs/detector gate. With increasing temperature, the resonance wavelengths red-shifted by about 0.077 nm.K^{-1}, and the free-spectral range changed by less than 0.001 nm.K^{-1} over the range of temperatures considered in these measurements. Due to full-width at half-maximum of the current versus wavelength, the minimum resolvable wavelength shift was about 11 pm. Single photons at signal and idler wavelengths were detected using gated InGaAs SPADs with an estimated 15% quantum efficiency, electrically-generated gate width of 2.5 ns and gating repetition frequency 5 MHz.

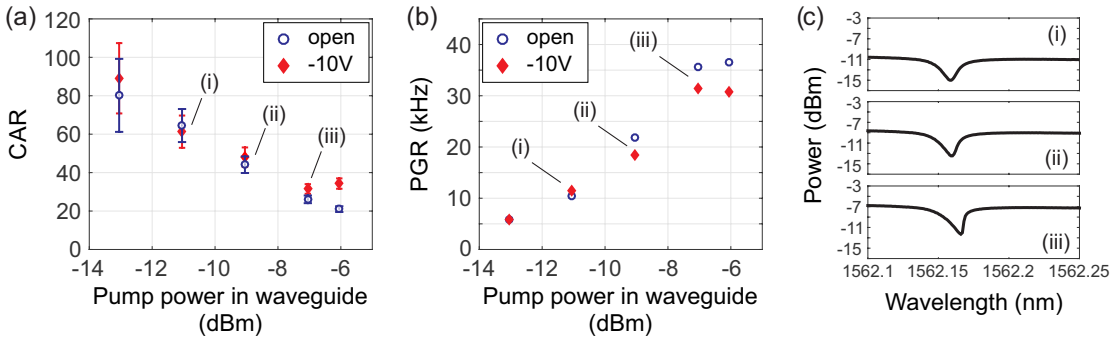

Figure 6.2: The (a) CAR versus optical pump power in the feeder waveguide and (b) PGR versus optical pump power in the feeder waveguide. (c) The panels labeled (i)–(iii) correspond to similar labels in panels (a) and (b), and show selected transmission lineshapes of the microring resonance, deforming from the Lorentzian profile with increasing optical pump power. These measurements were carried out at 30°C.

CAR versus pump power in waveguide is plotted in Fig. 6.2(b), and as expected the value of CAR decreased monotonically with increasing pump power. Sweeping out the free carriers through the reverse-bias voltage across the diode improved the CAR by a modest amount in most of the cases. Uncertainties in CAR come from fluctuations in the measured coincidence and accidental counts, and represent one standard deviation values. Based on the discussion presented in Ref. [101, Fig. 4], carrier sweepout in thin-slab diodes is rapidly screened when the intensity rises above a threshold. The onset of saturation at an optical intensity of 10^8 W.cm^{-2} in Ref. [101, Fig. 4] corresponds to a waveguide power of -6.3 dBm (235 μW) in this experiment, given the intensity resonant enhancement (425×) of the microring resonator. Therefore, application of a reverse-bias voltage is not expected to be too helpful in a high-quality silicon microring: carrier screening lessens its usefulness when the pair generation rate increases.

The pair generation rate (PGR) versus pump power is plotted in Fig. 6.2(b), after factoring out the chip-to-fiber coupling loss (3 dB), off-chip filter losses (6 dB for signal and 5 dB for idler) and detector quantum efficiencies (15%) – the error bars are smaller than the markers. The slight reduction in PGR with reverse bias voltage is probably caused by the spectral shift and slight change in the depth of resonance lineshape. The expected deformation of the lineshape caused by the

refractive index shifts due to heating from the continuous-wave pump beam circulating in the microring was also observed, as shown in Fig. 6.2(c) [102]. Though it was still possible to generate photon pairs with CAR > 10 in this regime, it is generally preferable to operate at a lower pump power to prevent instability.

When operating at a pump power of -6 dBm (250 μW) in the waveguide, the PGR, accounting for the off-chip losses and the SPAD detection efficiencies, was approximately 30 kHz. If we further scale PGR by the SPAD gating duty cycle, we estimate that an internal PGR of 240 kHz can be sustained by the silicon microring, which is similar, to within an order-of-magnitude, to other reports of silicon microrings [40, 72]. The calculated PGR will be raised further (by 21$\times$ to about 5 MHz) if we assume that the lower-bound limitation on detector timing is not the InGaAs SPAD gate width, but the photon lifetime (approximately 120 ps).

6.3 Optimization of Photon Pair Generation

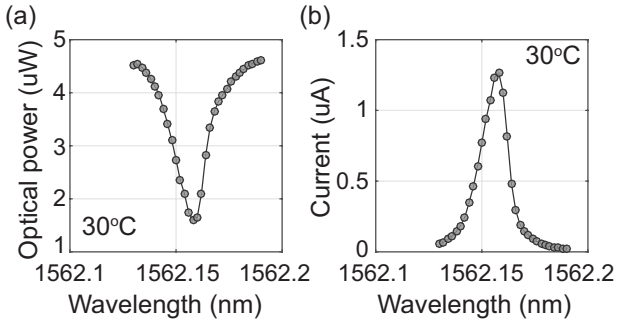

Figure 6.3: Measurements of the (a) optical transmission and (b) reverse-biased photocurrent at a fixed pump power of -11 dBm (80 μW) in the feeder waveguide and at 30°C.

Figs. 6.3(a) and (b) show measurements simultaneously made of optical transmission of the pump past the microring, using an off-chip InGaAs photodetector synchronized with the stepped wavelength scan of the tunable pump laser diode, and the electronic current from the reverse-biased diode across the microring. Here, a reverse-bias voltage of -1 V was applied and the temperature was set to 30°C. The two lineshapes were seen to closely correspond (including deviations

from a symmetric Lorentzian lineshape), for this and all other measured cases including at different power levels. The depth of the transmission resonance, relative to the baseline, reflects how much of the available pump power was delivered into the microring, whereas the peak in the current also reflects how much optical pump power circulates in the microring.

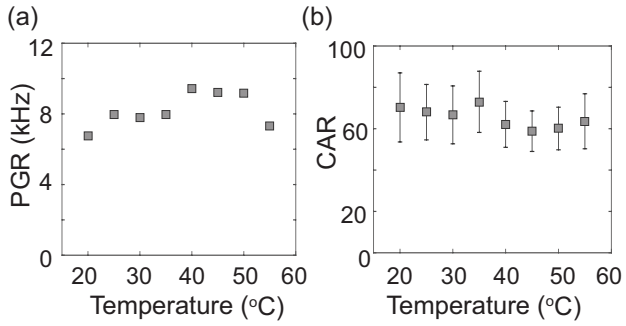

Figure 6.4: Using the reverse-biased current to find the optimal wavelength in each case, the (a) PGR and, (b) CAR were optimized at various different temperature settings, as indicated by the TEC resistance setting, converted to the indicated temperature readout by calibration.

We measured the pair generation properties of the microring at a range of different temperature settings, ranging from 20°C to 55°C on the TEC module (calibrated using a Steinhart-Hart equation). At each temperature setting, the appropriate pump wavelength was determined by finding the peak of the electronic diode current (at a reverse bias of -1V). Figs. 6.4(a) and (b) show that the pump wavelength could be successfully positioned to achieve favorable PGR and CAR over a wide temperature range. These experiments were run "open-loop", i.e., without continuous measurement-and-feedback stabilization of the pump wavelength. The required wavelength tuning range is well within the capabilities of distributed-feedback laser diodes [103]: 2.7 nm of pump wavelength variation compensated for a temperature change of 30°C. Without compensation, even 0.5°C change in temperature would reduce the CAR and PGR to nearly zero, given the wavelength sensitivity (about 0.077 nm.K^{-1}) and the linewidth of the microring resonance (0.018 nm). Minor variations in the trends in Figs. 6.4(a) and (b) may be attributed to small variations in the fiber-chip coupling, or gradual laser polar-

ization drifts over the long time taken to acquire the data (10 minutes per point), which are common when testing unpackaged chips.

6.4 Summary

In summary, these results show that a reverse-biased photodiode in a microring pair-generation device serves mainly to provide a measurement suitable for determining the optimum pump wavelength when the temperature varies and the resonance wavelength shifts. For a typical low-loss silicon microring, the current is approximately a few micro-amperes, which can be easily measured. Commercial laser diodes incorporate monitoring photodiodes as an essential component of a laser module; we believe that the reverse-biased diode in the silicon microring pair-generation device may serve a similar important role in monitoring and therefore, stabilizing, the non-classical light source without requiring a different material like germanium or InGaAs in the fabrication process.

Chapter 6 contains material, reproduced in part with permission, from Marc Savanier, Ranjeet Kumar, and Shayan Mookherjea, "Optimizing photon-pair generation electronically using a *p-i-n* diode incorporated in a silicon microring resonator" Applied Physics Letters Vol. 107, 131101 (2015). Copyright 2015, AIP Publishing LLC. The dissertation author was one of the primary author of this paper.

Appendix A

Coupled Resonator Optical Waveguide

The transmission spectrum of a CROW consisting of N coupled resonators can be written as a superposition of individually-weighted Lorentzian lineshapes, as shown in Fig. A.1,

$$\mathcal{T}(\omega) = \sum_{m=1}^{+\infty} \sum_{n=1}^{N} \mathcal{A}_{m,n} \mathcal{L}(\omega | \Omega_{m,n}; \tau_{m,n}) \tag{A.1}$$

where n indexes the resonators along the linear chain, and m is the azimuthal mode number, i.e., the number of wavelengths that physically fit along the resonator circumference. The value of m changes by 1 in going from one free spectral range (FSR) to the next.

The physical interpretation underlying Eq. (A.1) is that in each of the N Bloch modes that comprise the passband, the transmission is given by a Lorentzian line shape centered at $\Omega_{m,n}$ and with half-width at half-maximum (HWHM), $1/\tau_{m,n}$, defined as [104]

$$\Omega_{m,n} \approx \Omega_m - \frac{\Omega_m |\kappa|}{m\pi} \cos\left(\frac{n\pi}{N+1}\right) \tag{A.2}$$

$$\frac{1}{\tau_{m,n}} \approx \frac{1}{\tau_i} + \frac{2}{\tau_e} \frac{\sin^2\left(\frac{n\pi}{N+1}\right)}{\sum_{p=1}^{N} \sin^2\left(p\frac{n\pi}{N+1}\right)} \tag{A.3}$$

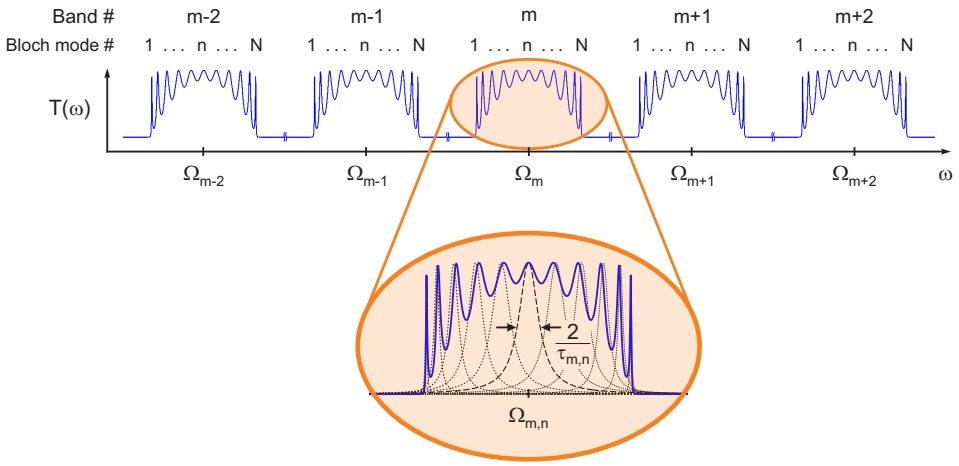

Figure A.1: Multi-peaked transmission spectrum of a CROW. The widths of the resonances are not uniform, and become narrower near the edges of the band.

where $\Omega_m = (mc)/(n_{\text{eff}}R_{\text{eff}})$ is the passband center frequency for the optical mode of effective index n_{eff} circulating in a resonator of effective radius R_{eff}, $|\kappa|$ is the inter-resonator coupling coefficient, $1/\tau_{\text{i}}$ and $1/\tau_{\text{e}}$ are the internal and external dissipation rates, accounting respectively for the optical losses in the resonators, and for the additional losses arising from the input and output coupling. In Eq. (A.1), each Lorentzian is weighted by a factor:

$$\mathcal{A}_{m,n} = \exp(-S_{m,n}\alpha N\pi R_{\text{eff}}) \tag{A.4}$$

where α is the waveguide loss coefficient, and $S_{m,n}$ is the slowing factor, reflecting the fact that light at transmission band edges travels slower, and therefore experiences greater attenuation, than light at the band center. S is defined as the group velocity in the constituent waveguide divided by the group velocity in the coupled-resonator waveguide [39, 105].

Appendix A contains material, reproduced in part with permission, from Ranjeet Kumar, Jun Rong Ong, Marc Savanier, and Shayan Mookherjea, "Controlling the spectrum of photons generated on a silicon nanophotonic chip" Nature Communications Vol. 5, art. 5489 (2014). Copyright 2014. The dissertation author was the primary author of this paper.

Appendix B

Two-Photon Interference (Franson Interferometer)

B.1 Some Mathematical Relations

B.1.1 Coincidence Rate Derivation

Based on the discussion from Chapter 4, after post-selection, $|\Psi_{out}\rangle$ can be written as coherent superposition of $|\Psi_s\rangle_1|\Psi_s\rangle_2$ and $|\Psi_l\rangle_1|\Psi_l\rangle_2$:

$$|\Psi\rangle_{out} \approx \frac{1}{\sqrt{2}}\left[|\Psi_s\rangle_1|\Psi_s\rangle_2 + |\Psi_l\rangle_1|\Psi_l\rangle_2\right] \tag{B.1}$$

and due to relative phase ($\Delta\Phi$) between the interfering $|\Psi_s\rangle_1|\Psi_s\rangle_2$ and $|\Psi_l\rangle_1|\Psi_l\rangle_2$, we can write:

$$|\Psi_l\rangle_1|\Psi_l\rangle_2 = |\Psi_s\rangle_1|\Psi_s\rangle_2 \mathrm{e}^{i\Delta\Phi} \tag{B.2}$$

Now, using Eq. B.2, Eq. B.1 can be rewritten as:

$$\begin{aligned} |\Psi\rangle_{out} &\approx \frac{1}{\sqrt{2}}\left[|\Psi_s\rangle_1|\Psi_s\rangle_2 + |\Psi_s\rangle_1|\Psi_s\rangle_2 \mathrm{e}^{i\Delta\Phi}\right] \\ &\approx \frac{1}{\sqrt{2}}\left[1 + \mathrm{e}^{i\Delta\Phi}\right]|\Psi_s\rangle_1|\Psi_s\rangle_2 \end{aligned} \tag{B.3}$$

It should be noted that Eq. B.3 is a quantum state, and in order to find the coincidence rate, we need to find $\langle\Psi|\Psi\rangle_{out}$. Using Eq. B.3, $\langle\Psi|\Psi\rangle_{out}$ can be calculated as:

$$\langle\Psi|\Psi\rangle_{out} \approx \langle\Psi_s|\langle\Psi_s|\Psi_s\rangle_1|\Psi_s\rangle_2 \frac{1+\mathrm{e}^{i\Delta\Phi}}{\sqrt{2}} \frac{1+\mathrm{e}^{-i\Delta\Phi}}{\sqrt{2}} \tag{B.4}$$

or

$$\text{Coincidence Rate} \equiv \langle\Psi|\Psi\rangle_{out} \propto \frac{1+\mathrm{e}^{i\Delta\Phi}}{\sqrt{2}} \frac{1+\mathrm{e}^{-i\Delta\Phi}}{\sqrt{2}} \equiv 1+\cos\Delta\Phi \tag{B.5}$$

B.1.2 Phase versus Path Imbalance

The path imbalance (ΔL) between the arms of a Mach-Zehnder Interferometer (MZI) leads to a phase difference between the arms:

$$\Delta\Phi = \frac{2\pi}{\lambda}\Delta\mathrm{L} \tag{B.6}$$

where λ is the wavelength of the light field. Hence, the total phase of the photons can be written as::

$$\Delta\Phi = \frac{2\pi}{\lambda_1}\Delta\mathrm{L}_1 + \frac{2\pi}{\lambda_2}\Delta\mathrm{L}_2 \tag{B.7}$$

‘

here λ_1 and λ_2 are the wavelength of the photons entering interferometer 1 and 2, respectively. $\Delta\mathrm{L}_1$ & $\Delta\mathrm{L}_2$ are the path imbalances of two interferometers. Eq. B.7 can also be rewritten as:

$$\Delta\Phi = \frac{\omega_1 n_1 \Delta\mathrm{L}_1}{c} + \frac{\omega_2 n_2 \Delta\mathrm{L}_2}{c} \tag{B.8}$$

Measurement with Two Interferometers

With two interferometers, one for each photon, we have:

$$\begin{aligned}\Delta\Phi &= \underbrace{\left(\frac{\omega_1+\omega_2}{2c}\right)}_{2\omega_p=\omega_1+\omega_2}[n_1\Delta L_1 + n_2\Delta L_2] + \underbrace{\left(\frac{\omega_1-\omega_2}{2c}\right)}_{\omega_1-\omega_2\approx 0}[n_1\Delta L_1 - n_2\Delta L_2] \\ &= \frac{2\omega_p}{2c}\underbrace{[n_1\Delta L_1 + n_2\Delta L_2]}_{n_1\approx n_2\approx n_p} \\ &= \frac{\omega_p n_p}{c}(\Delta L_1 + \Delta L_2) \end{aligned} \tag{B.9}$$

In this case, the coincidence rate can be written as:

$$\text{Coincidence Rate} \propto \frac{1+e^{i\Delta\Phi}}{\sqrt{2}}\frac{1+e^{-i\Delta\Phi}}{\sqrt{2}} \equiv 1+\cos\left[\frac{\omega_p n_p}{c}(\Delta L_1 + \Delta L_2)\right] \tag{B.10}$$

Measurement with One Interferometer

Now consider the case when instead of two interferometers, there is only one interferometer for both the photons. In that case, ΔL_1 and ΔL_2 are the same and can be written as $\Delta L_1 = \Delta L_2 = \Delta L$. Eq. B.8 can be written as:

$$\begin{aligned}\Delta\Phi &= \frac{\omega_1 n_1 \Delta L}{c} + \frac{\omega_2 n_2 \Delta L}{c} \\ &= \underbrace{\left(\frac{\omega_1+\omega_2}{2c}\right)}_{2\omega_p=\omega_1+\omega_2}[n_1\Delta L + n_2\Delta L] + \underbrace{\left(\frac{\omega_1-\omega_2}{2c}\right)}_{\omega_1-\omega_2\approx 0}[n_1\Delta L - n_2\Delta L] \\ &= \frac{2\omega_p}{2c}\underbrace{[n_1\Delta L + n_2\Delta L]}_{n_1\approx n_2\approx n_p} \\ &= \frac{\omega_p n_p}{c}(2\Delta L) \end{aligned} \tag{B.11}$$

In this case, the coincidence rate can be written as:

$$\text{Coincidence Rate} \propto \frac{1+e^{i\Delta\Phi}}{\sqrt{2}}\frac{1+e^{-i\Delta\Phi}}{\sqrt{2}} \equiv 1+\cos\left[\frac{\omega_p n_p}{c}(2\Delta L)\right] \tag{B.12}$$

B.2 Experimental Details

Based on the discussion presented in Chapter 4, the experimental conditions can be summarized as follows:

- Path dependent indistinguishability requires the following:
  1. $\Delta L \equiv \Delta L_1 - \Delta L_2 \ll$ Two-photon coherence length
  2. Both ΔL_1 (or $\Delta\tau_1$) & ΔL_2 (or $\Delta\tau_2$) $<$ Pump pulse width
- No single photon interference: Both ΔL_1 & $\Delta L_2 \gg$ Single photon coherence length

The experimental setup shown in Fig. 4.1 is designed with the above requirements taken into consideration.

B.2.1 Timing Information

The measurements in Chapter 4 were done using a pump waveform carved by an electro-optic modulator into temporal pulses whose duration was 8 ns nanoseconds, and using gating on the InGaAs SPADs whose duration was 2.5 ns. Under these conditions, the relative alignment of the gate with the pulse can influence the coincidence events, as described in Fig. B.1. The convolution of detector gate with the optical pump pulse gives singles versus delay a trapezoid shape. Due to the time lag ($\Delta\tau$) between the short (S) and long (L) arm of the MZI, a photon traveling along the longer arm arrives at the detector with a lag of $\Delta\tau$, resulting in a shifted trapezoid. In order to reduce the detection noise from the SPADs, the gate width (GW) and optical pump pulse width (PW) had to be kept as short as possible. Here, within the experimental imperfections, $\Delta\tau$ was chosen to be approximately same as the GW (2.5 ns being the minimum value for our SPADs) and the PW was chosen such that the trapezoids for S and L only overlap for the time period of GW, implying PW should be equal to GW + $\Delta\tau$ + GW. PW $> \Delta\tau$ also ensures the indistinguishability of detected photons in $|S_1S_2\rangle + |L_1L_2\rangle$ measurement, otherwise, based on the timing information of the coincidence events it

can be deduced whether the pairs took the short or the long arm, which can give the information about their emission times.

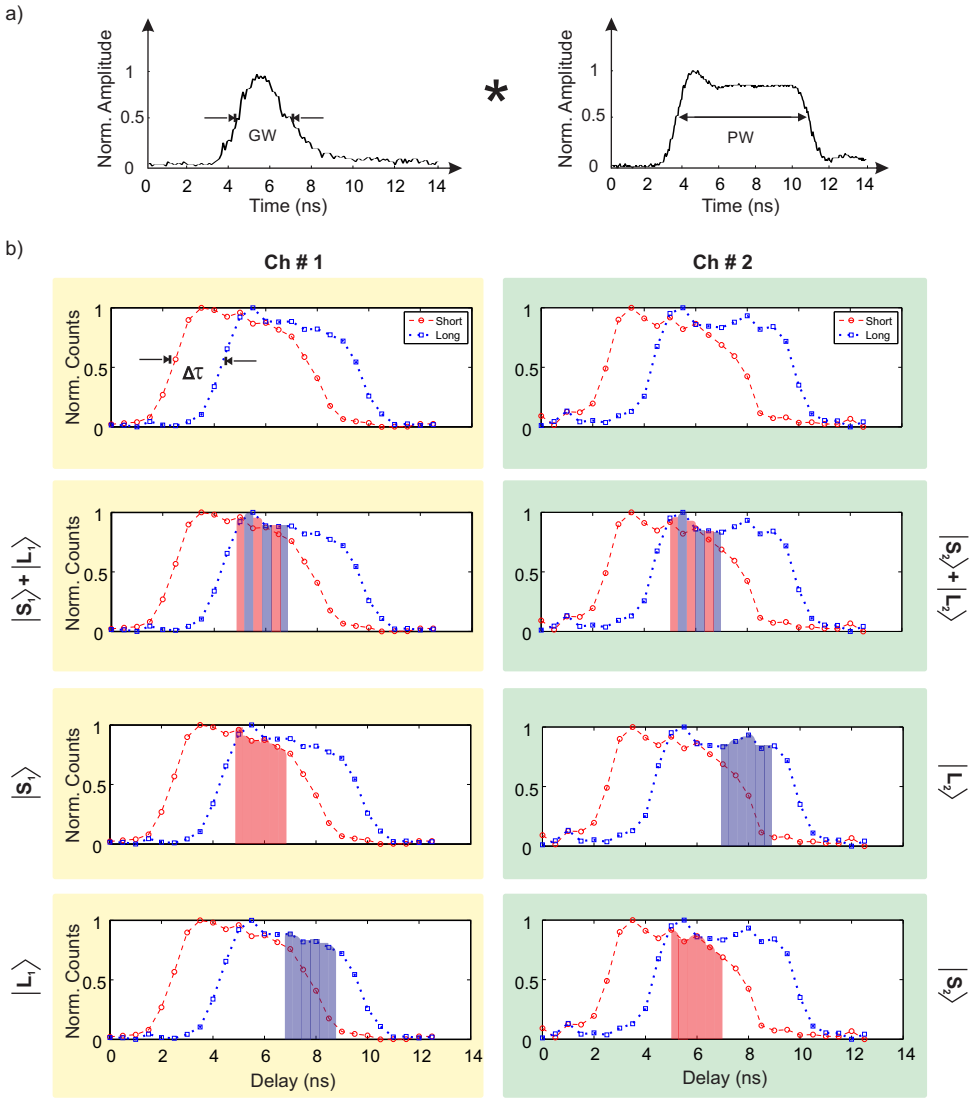

Figure B.1: (a) Detected singles are the result of the convolution of detector gate (left) with the optical pulse width (right), while the gate relative delays varies. (b) Each SPAD can detect photons having taken the short (red) or the long (blue) arm of the MZI. By changing the relative position of the gate within the pump pulse, independently for the two SPADs (CH1: left column, CH2: right column), we can select the events which coincidences are measured by the TCSPC module. Second row is $|S_1S_2\rangle + |L_1L_2\rangle$, third row is $|S_1L_2\rangle$, and fourth row is $|L_1S_2\rangle$.

It is important to note that because the signal-idler photons are generated at the same time, singles coming from different portions of the pump pulse can

not result in a coincidence event. As a result, the first gate configuration shown in Fig. B.1(b) allowed the coincidence measurement associated with $|S_1S_2\rangle + |L_1L_2\rangle$: $|S_1S_2\rangle$ via the trailing edge of the pulse and $|L_1L_2\rangle$ via the leading edge of the pulse. Likewise, second and third configurations lead to the coincidence measurement of $|S_1L_2\rangle$ and $|L_1S_2\rangle$.

B.2.2 Stabilization of the MZI

The MZI used in the experiment was made of commercial off-the-shelf fiber and free-space optical components. Polarization maintaining optical fibers were used in the long arm and free-space components such as collimators and mirrors, along with polarization maintaining optical fibers, were used in the short arm. The phase of the interferometer was controlled using a piezo-actuator in the free-space arm, which was a part of NI-DAQ and Matlab simulink based feedback controller, as shown in Fig. B.2 (also shown in Fig. 4.1). 10% taps from the output of interferometer was used as an "analog input" for the simulink block, and the "analog output" of the PID controller was used as a driving voltage for the piezo-actuator.

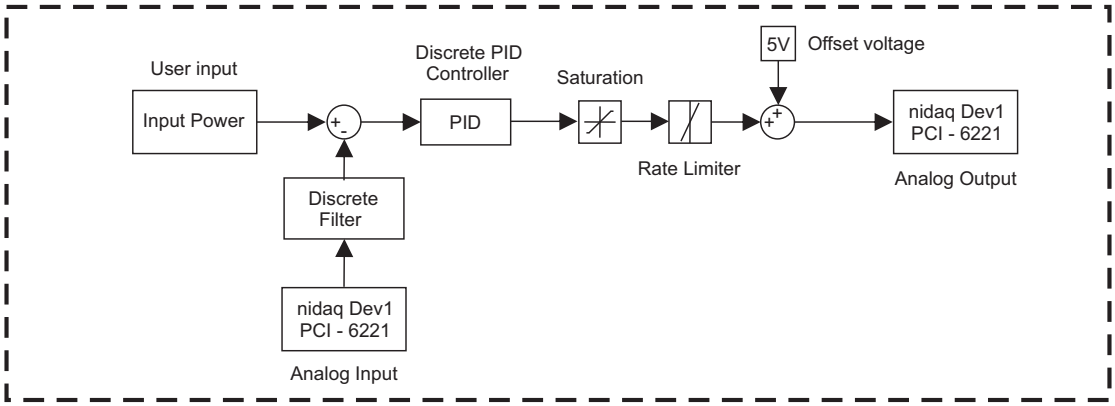

Figure B.2: Matlab simulink block diagram for MZI feedback control.

B.2.3 Estimation of Phase of the MZI

The dependence of the MZI output power P can be described classically through:

$$\mathrm{P} = \left(\frac{\mathrm{P_M} + \mathrm{P_m}}{2}\right) + \left(\frac{\mathrm{P_M} - \mathrm{P_m}}{2}\right)\cos(\phi) \tag{B.13}$$

where $\mathrm{P_M}$ and $\mathrm{P_m}$ are respectively the maximum and minimum values taken by P, and ϕ is the relative phase between the two arms of the MZI. Using Eq. B.13, the phase of the MZI, which changes due to change in the optical path length, can be estimated.

B.2.4 MZI Feedback-Loop Phase Stability

Eq. B.13 can also be written as

$$\mathrm{P_{out}} = \mathrm{IL} \times \frac{\mathrm{P_{in}}}{2} \times [1 + \mathrm{V}\cos(\phi)] \tag{B.14}$$

where IL is the insertion loss in the MZI, $\mathrm{P_{out}}$ and $\mathrm{P_{in}}$ are the output and input powers of the MZI, respectively; V is the classical MZI fringe visibility, and ϕ is the phase of the MZI. Assuming constant IL and V, the differentiation of Eq. B.14, along with standard error propagation theory, leads to:

$$\Delta\phi = \frac{1 + \mathrm{V}\cos(\phi)}{\mathrm{V}\sin(\phi)} \times \left(\frac{\Delta\mathrm{P_{out}}}{\mathrm{P_{out}}} + \frac{\Delta\mathrm{P_{in}}}{\mathrm{P_{in}}}\right) \tag{B.15}$$

Using Eq. B.14, $\cos(\phi)$ and $\sin(\phi)$ can be rearranged as follows

$$\begin{aligned} \cos(\phi) &= \frac{1}{\mathrm{V}}\left(\frac{2}{\mathrm{IL}} \times \frac{\mathrm{P_{out}}}{\mathrm{P_{in}}} - 1\right) \\ \sin(\phi) &= \sqrt{1 - \frac{1}{\mathrm{V}^2}\left(\frac{2}{\mathrm{IL}} \times \frac{\mathrm{P_{out}}}{\mathrm{P_{in}}} - 1\right)^2} \end{aligned} \tag{B.16}$$

Combining Eq. B.15 and Eq. B.16, leads to

$$\Delta\phi = \frac{\frac{2}{\mathrm{IL}} \times \frac{\mathrm{P_{out}}}{\mathrm{P_{in}}}}{\underbrace{\sqrt{\mathrm{V}^2 - \left(\frac{2}{\mathrm{IL}} \times \frac{\mathrm{P_{out}}}{\mathrm{P_{in}}} - 1\right)^2}}_{\text{constant}}} \times \left(\underbrace{\frac{\Delta \mathrm{P_{out}}}{\mathrm{P_{out}}}}_{2\%} + \underbrace{\frac{\Delta \mathrm{P_{in}}}{\mathrm{P_{in}}}}_{1\%} \right) \tag{B.17}$$

Based on the experimental values IL = -7 dB and V = 0.72 for residual pump (classical light). The value of $\Delta\phi$ is estimated to be ± 0.1 radian ($\pm 6.3°$), indicating that the length of the MZI variable arm is stabilized within ± 25 nm relatively to the other arm. The modest value of the visibility V is attributed to the fact that the residual pump available for the MZI stabilization is pulsed. Indeed, V is greater than 0.99 when a CW laser source is used as an input of the MZI (consistent with the observed extinction ratio >25dB).

B.2.5 Estimation of Visibility

The visibility is estimated through the fitting of the measured coincidence rates as a function of the MZI phase, as described in Eq. B.13. The fitting procedure was based on the Levenberg-Marquardt non-linear least-square curve fitting algorithm, and the following model:

$$\mathrm{C}(\phi; \mathrm{A}, \mathrm{B}, \Theta) = \mathrm{A} + \mathrm{B}\cos(\phi + \Theta) \tag{B.18}$$

where ϕ is the phase of the MZI; A, B, and Θ are the fit parameters. Once the data are fitted, the visibility is calculated through the following:

$$\mathrm{V} = \frac{\mathrm{C_{max}} - \mathrm{C_{min}}}{\mathrm{C_{max}} + \mathrm{C_{min}}} = \frac{\mathrm{B}}{\mathrm{A}} \tag{B.19}$$

where $\mathrm{C_{max}}$ and $\mathrm{C_{min}}$ are the maximum and minimum values of the fit function, respectively. So far, the effect of accidental counts has not been taken into account in either the measured coincidence or the fit function. Hence, Eq. B.19 requires a modification based on the effect of accidental counts [26]. Based on the average accidentals A_c, averaged over all the phase values, the expression becomes

$$\mathrm{V_{corr}} = \frac{\mathrm{C_{max}} - \mathrm{C_{min}}}{\mathrm{C_{max}} + \mathrm{C_{min}} - 2 \times A_c} \tag{B.20}$$

From Eq. B.19, it is apparent that $\mathrm{V_{corr}}$ is affected by the uncertainty with which the two independent variables A and B are estimated. Using the standard error propagation, the relative error in visibility can be written as

$$\frac{\Delta \mathrm{V_{corr}}}{\mathrm{V_{corr}}} = \sqrt{\left(\frac{\Delta \mathrm{A}}{\mathrm{A}}\right)^2 + \left(\frac{\Delta \mathrm{B}}{\mathrm{B}}\right)^2} \tag{B.21}$$

Appendix C

Some Useful Definitions

C.1 Group Velocity

$$\begin{aligned} v_g &= \frac{c}{n_g} \\ &= \left(\frac{d\omega}{d\beta}\right)_{\omega_0} \end{aligned} \tag{C.1}$$

where ω is the angular frequency of light, β is the wave-vector of light, and c is the speed of light in vacuum. β is related to the refractive index through the following expression:

$$\beta = n(\omega)\frac{\omega}{c} \tag{C.2}$$

C.2 Phase Velocity

Phase velocity is also related to ω and β through the following relation:

$$\begin{aligned} v_p &= \frac{c}{n(\omega)} \\ &= \frac{\omega}{\beta} \end{aligned} \tag{C.3}$$

C.3 Group Index

Group index can be expressed in the following two forms through dispersion relation:

$$n_g = n + \omega \frac{dn}{d\omega} \tag{C.4}$$

$$n_g = n - \lambda \frac{dn}{d\lambda} \tag{C.5}$$

C.4 Free Spectral Range

Free spectral range (FSR) is defined as the difference in frequency ($\Delta\nu$) between two adjacent resonances. From the resonance condition, we have the following expressions:

$$\begin{aligned} \beta_1 \mathrm{L} &= m2\pi \\ \beta_2 \mathrm{L} &= (m+1)\,2\pi \end{aligned} \tag{C.6}$$

where L is the round trip length of the resonator cavity and m is an integer. From Eq. C.6, we have the following relation:

$$(\beta_2 - \beta_1)\,\mathrm{L} = 2\pi \tag{C.7}$$

or using E. C.2, we have

$$\left(\frac{n_{\omega_2}\omega_2}{c} - \frac{n_{\omega_1}\omega_1}{c}\right)\mathrm{L} = 2\pi \tag{C.8}$$

Since $\omega_2 - \omega_1$ is much smaller than the ω_1 or ω_2, we can do the Taylor expansion of n_{ω_2} as

$$n_{\omega_2} \approx n_{\omega_1} + (\omega_2 - \omega_1)\,\frac{dn}{d\omega}|_{\omega=\omega_1} \tag{C.9}$$

Using Eq. C.9 in Eq. C.8 leads to

$$n_{\omega_1}\,(\omega_2 - \omega_1)\,\frac{\mathrm{L}}{c} + (\omega_2 - \omega_1)\,\frac{dn}{d\omega}|_{\omega=\omega_1}\frac{\omega_2 \mathrm{L}}{c} = 2\pi \tag{C.10}$$

Eq. C.10 can written as

$$\Delta\nu = \nu_2 - \nu_1 = \frac{c/\mathrm{L}}{n_{\omega_1} + \omega_2 \frac{dn}{d\omega}|_{\omega_2}} = \frac{c/\mathrm{L}}{n_{\lambda_1} - \lambda_2 \frac{dn}{d\lambda}|_{\lambda_2}} \tag{C.11}$$

Using Eq. C.5, Eq. C.11 can be written as:

$$\Delta\nu = \frac{c}{n_g \mathrm{L}} \tag{C.12}$$

C.5 Quality Factor

Quality factor of a resonator is related to the bandwidth of its Lorentzian lineshape. For a Lorentzian lineshape, the energy decays exponentially in the resonator.

$$Q = \omega \times \frac{\text{field energy stored by the resonator}}{\text{power dissipated by the resonator}} \tag{C.13}$$

$$Q = \frac{\lambda_0}{\Delta\lambda_{1/2}} = \frac{\Omega}{\Delta\omega_{1/2}} \tag{C.14}$$

where Ω is the resonance frequency of the resonator, λ_0 is the resonance wavelength, and $\Delta\omega_{1/2}$ and $\Delta\lambda_{1/2}$ are the full-widths half-maximum (FWHM) in frequency and wavelength of the lineshape, respectively.

C.6 Finesse

Finesse ($\mathcal{F}$) of a resonator is defined as the ratio of its Free spectral range and full-width half maximum of the lineshape.

$$\mathcal{F} = \frac{\Delta\omega_{FSR}}{\Delta\omega_{1/2}} = \frac{\Delta\lambda_{FSR}}{\Delta\lambda_{1/2}} \tag{C.15}$$

C.7 $\alpha\left[\mathbf{cm}^{-1}\right]$ to $\alpha_{\mathbf{dB}}\left[\mathbf{dBcm}^{-1}\right]$ conversion

From the definition of dB scale, we have the following equation:

$$\begin{aligned} \alpha_{\mathrm{dB}} &= -\frac{10}{\mathrm{L}}\log_{10}\left(\frac{\mathrm{P_O}}{\mathrm{P_I}}\right) \\ &= -\frac{10}{\mathrm{L}}\log_{10}\mathrm{e} \times \log_{\mathrm{e}}\left(\frac{\mathrm{P_O}}{\mathrm{P_I}}\right) \end{aligned} \tag{C.16}$$

where α_{dB} is the dBcm^{-1} loss, $\mathrm{P_I}$ and $\mathrm{P_O}$ are input and output powers, respectively. $\mathrm{P_I}$ and $\mathrm{P_O}$ are also related through the linear loss (α) through following equation:

$$\mathrm{P_O} = \mathrm{P_I}\mathrm{e}^{-\alpha\mathrm{L}} \tag{C.17}$$

or

$$\alpha = -\frac{1}{\mathrm{L}}\log_{\mathrm{e}}\left(\frac{\mathrm{P_O}}{\mathrm{P_I}}\right) \tag{C.18}$$

Now, Eq. C.16 and Eq. C.18 can be combined such that we have the following expression:

$$\alpha_{\mathrm{dB}} = 10\log_{10}\mathrm{e} \times \alpha \tag{C.19}$$

Eq.C.20 can simplified as

$$\alpha_{\mathrm{dB}} \approx 4.343\alpha \tag{C.20}$$

Bibliography

[1] E. Knill, R. Laflamme, and G. J. Milburn, "A scheme for efficient quantum computation with linear optics," *Nature*, vol. 409, no. 6816, pp. 46–52, Jan. 2001.

[2] C. H. Bennett and G. Brassard, "Quantum cyptography: Public key distribution and coin tossing," *Proceedings of IEEE International Conference on Computers, Systems, and Signal Processing - Bangalore*, p. 175, 1984.

[3] B. C. Sanders, "Quantum dynamics of the nonlinear rotator and the effects of continual spin measurement," *Physical Review A*, vol. 40, pp. 2417–2427, Sep 1989.

[4] A. N. Boto, P. Kok, D. S. Abrams, S. L. Braunstein, C. P. Williams, and J. P. Dowling, "Quantum interferometric optical lithography: exploiting entanglement to beat the diffraction limit," *Physical Review Letters*, vol. 85, no. 13, p. 2733, 2000.

[5] A. K. Ekert, "Quantum cryptography based on Bells theorem," *Physical Review Letters*, vol. 67, no. 6, p. 661, 1991.

[6] R. L. Rivest, A. Shamir, and L. M. Adleman, "Cryptographic communications system and method," US Patent 4,405,829, Sep. 20 1983.

[7] S. Kako, C. Santori, K. Hoshino, S. Götzinger, Y. Yamamoto, and Y. Arakawa, "A gallium nitride single-photon source operating at 200 K," *Nature Materials*, vol. 5, no. 11, pp. 887–892, 2006.

[8] S. Strauf, N. G. Stoltz, M. T. Rakher, L. A. Coldren, P. M. Petroff, and D. Bouwmeester, "High-frequency single-photon source with polarization control," *Nature Photonics*, vol. 1, no. 12, pp. 704–708, 2007.

[9] F. Treussart, G. Messin, Y. Dumeige, J.-F. Roch, A. Beveratos, R. Brouri-Tualle, J. Poizat, and P. Grangier, "Experimental open-air quantum key distribution with a single-photon source," *New Journal of Physics*, vol. 6, no. 1, p. 92, 2004.

[10] T. Gaebel, I. Popa, A. Gruber, M. Domhan, F. Jelezko, and J. Wrachtrup, "Stable single-photon source in the near infrared," *New Journal of Physics*, vol. 6, no. 1, p. 98, 2004.

[11] W. Louisell, A. Yariv, and A. Siegman, "Quantum fluctuations and noise in parametric processes. I." *Physical Review*, vol. 124, no. 6, p. 1646, 1961.

[12] D. C. Burnham and D. L. Weinberg, "Observation of simultaneity in parametric production of optical photon pairs," *Physical Review Letters*, vol. 25, no. 2, p. 84, 1970.

[13] H. Takesue, Y. Tokura, H. Fukuda, T. Tsuchizawa, T. Watanabe, K. Yamada, and S.-i. Itabashi, "Entanglement generation using silicon wire waveguide," *Applied Physics Letters*, vol. 91, no. 20, 2007.

[14] J. E. Sharping, M. Fiorentino, and P. Kumar, "Observation of twin-beam-type quantum correlation in optical fiber," *Optics Letters*, vol. 26, no. 6, pp. 367–369, 2001.

[15] C. Hong and L. Mandel, "Experimental realization of a localized one-photon state," *Physical Review Letters*, vol. 56, no. 1, p. 58, 1986.

[16] P. Grangier, G. Roger, and A. Aspect, "Experimental evidence for a photon anticorrelation effect on a beam splitter: a new light on single-photon interferences," *EPL (Europhysics Letters)*, vol. 1, no. 4, p. 173, 1986.

[17] C. H. Bennett, "Quantum cryptography using any two nonorthogonal states," *Physical Review Letters*, vol. 68, no. 21, p. 3121, 1992.

[18] S. Ramelow, L. Ratschbacher, A. Fedrizzi, N. Langford, and A. Zeilinger, "Discrete tunable color entanglement," *Physical Review Letters*, vol. 103, no. 25, p. 253601, 2009.

[19] A. Mair, A. Vaziri, G. Weihs, and A. Zeilinger, "Entanglement of the orbital angular momentum states of photons," *Nature*, vol. 412, no. 6844, pp. 313–316, 2001.

[20] I. Kaminow, T. Li, and A. E. Willner, *Optical Fiber Telecommunications Volume VIA: Components and Subsystems*, 6th ed. Oxford, UK: Academic Press, 2013.

[21] ITU-T Recommendation G.694.2, *Spectral grids for WDM applications: CWDM wavelength grid*. International Telecommunication Union, Dec. 2003.

[22] B. Jalali and S. Fathpour, "Silicon photonics," *Journal of Lightwave Technology*, vol. 24, no. 12, pp. 4600–4615, 2006.

[23] J. E. Sharping, K. F. Lee, M. A. Foster, A. C. Turner, B. S. Schmidt, M. Lipson, A. L. Gaeta, and P. Kumar, "Generation of correlated photons in nanoscale silicon waveguides," *Optics Express*, vol. 14, no. 25, pp. 12 388–12 393, 2006.

[24] K.-i. Harada, H. Takesue, H. Fukuda, T. Tsuchizawa, T. Watanabe, K. Yamada, Y. Tokura, and S.-i. Itabashi, "Generation of high-purity entangled photon pairs using silicon wire waveguide," *Optics Express*, vol. 16, no. 25, pp. 20 368–20 373, 2008.

[25] S. Clemmen, K. P. Huy, W. Bogaerts, R. G. Baets, P. Emplit, and S. Massar, "Continuous wave photon pair generation in silicon-on-insulator waveguides and ring resonators," *Optics Express*, vol. 17, no. 19, pp. 16 558–16 570, 2009.

[26] M. Davanço, J. R. Ong, A. B. Shehata, A. Tosi, I. Agha, S. Assefa, F. Xia, W. M. Green, S. Mookherjea, and K. Srinivasan, "Telecommunications-band heralded single photons from a silicon nanophotonic chip," *Applied Physics Letters*, vol. 100, no. 26, p. 261104, 2012.

[27] S. Azzini, D. Grassani, M. J. Strain, M. Sorel, L. Helt, J. Sipe, M. Liscidini, M. Galli, and D. Bajoni, "Ultra-low power generation of twin photons in a compact silicon ring resonator," *Optics Express*, vol. 20, no. 21, pp. 23 100–23 107, 2012.

[28] E. Engin, D. Bonneau, C. M. Natarajan, A. S. Clark, M. Tanner, R. H. Hadfield, S. N. Dorenbos, V. Zwiller, K. Ohira, N. Suzuki, H. Yoshida, N. Iizuka, M. Ezaki, J. L. O'Brien, and M. G. Thompson, "Photon pair generation in a silicon micro-ring resonator with reverse bias enhancement," *Optics Express*, vol. 21, no. 23, pp. 27 826–27 834, 2013.

[29] R. Kumar, M. Savanier, J. R. Ong, and S. Mookherjea, "Entanglement measurement of a coupled silicon microring photon pair source," *Optics Eexpress*, vol. 23, no. 15, pp. 19 318–19 327, 2015.

[30] W. C. Jiang, X. Lu, J. Zhang, O. Painter, and Q. Lin, "Silicon-chip source of bright photon pairs," *Optics Express*, vol. 23, no. 16, pp. 20 884–20 904, 2015.

[31] M. Savanier, R. Kumar, and S. Mookherjea, "Photon pair generation from compact silicon microring resonators using microwatt-level pump powers," *Optics Express*, vol. 24, no. 4, pp. 3313–3328, 2016.

[32] Q. Lin and G. P. Agrawal, "Silicon waveguides for creating quantum-correlated photon pairs," *Optics Letters*, vol. 31, no. 21, pp. 3140–3142, 2006.

[33] C. Xiong, G. D. Marshall, A. Peruzzo, M. Lobino, A. S. Clark, D.-Y. Choi, S. J. Madden, C. M. Natarajan, M. G. Tanner, R. H. Hadfield, S. N. Dorenbos, T. Zijlstra, V. Zwiller, M. G. Thompson, J. G. Rarity, M. J. Steel, B. Luther-Davies, B. J. Eggleton, and J. L. O'Brien, "Generation of correlated photon pairs in a chalcogenide As_2S_3 waveguide," *Applied Physics Letters*, vol. 98, no. 5, p. 051101, 2011.

[34] I. D. Rukhlenko, M. Premaratne, and G. P. Agrawal, "Effective mode area and its optimization in silicon-nanocrystal waveguides," *Optics Letters*, vol. 37, no. 12, pp. 2295–2297, 2012.

[35] J. R. Ong, M. L. Cooper, G. Gupta, W. M. Green, S. Assefa, F. Xia, and S. Mookherjea, "Low-power continuous-wave four-wave mixing in silicon coupled-resonator optical waveguides," *Optics Letters*, vol. 36, no. 15, pp. 2964–2966, 2011.

[36] N. Matsuda, T. Kato, K.-i. Harada, H. Takesue, E. Kuramochi, H. Taniyama, and M. Notomi, "Slow light enhanced optical nonlinearity in a silicon photonic crystal coupled-resonator optical waveguide," *Optics Express*, vol. 19, no. 21, pp. 19 861–19 874, 2011.

[37] H. Takesue and K. Inoue, "1.5-μm band quantum-correlated photon pair generation in dispersion-shifted fiber: suppression of noise photons by cooling fiber," *Optics Express*, vol. 13, no. 20, pp. 7832–7839, 2005.

[38] S. Mookherjea, "Dispersion characteristics of coupled-resonator optical waveguides," *Optics Letters*, vol. 30, no. 18, pp. 2406–2408, 2005.

[39] J. R. Ong and S. Mookherjea, "Quantum light generation on a silicon chip using waveguides and resonators," *Optics Express*, vol. 21, no. 4, pp. 5171–5181, 2013.

[40] D. Grassani, S. Azzini, M. Liscidini, M. Galli, M. J. Strain, M. Sorel, J. Sipe, and D. Bajoni, "Micrometer-scale integrated silicon source of time-energy entangled photons," *Optica*, vol. 2, pp. 88–94, 2015.

[41] J. Chen, Z. H. Levine, J. Fan, and A. L. Migdall, "Frequency-bin entangled comb of photon pairs from a silicon-on-insulator micro-resonator," *Optics Express*, vol. 19, no. 2, pp. 1470–1483, 2011.

[42] I. Marcikic, H. de Riedmatten, W. Tittel, V. Scarani, H. Zbinden, and N. Gisin, "Time-bin entangled qubits for quantum communication created by femtosecond pulses," *Physical Review A*, vol. 66, no. 6, p. 062308, 2002.

[43] A. B. U'Ren, R. K. Erdmann, M. de la Cruz-Gutierrez, and I. A. Walmsley, "Generation of two-photon states with an arbitrary degree of entanglement

via nonlinear crystal superlattices," *Physical Review Letters*, vol. 97, no. 22, p. 223602, 2006.

[44] C. Law, I. Walmsley, and J. Eberly, "Continuous frequency entanglement: effective finite Hilbert space and entropy control," *Physical Review Letters*, vol. 84, no. 23, p. 5304, 2000.

[45] C. Law and J. Eberly, "Analysis and interpretation of high transverse entanglement in optical parametric down conversion," *Physical Review Letters*, vol. 92, no. 12, p. 127903, 2004.

[46] A. Valencia, A. Ceré, X. Shi, G. Molina-Terriza, and J. Torres, "Shaping the waveform of entangled photons." *Physical Review Letters*, vol. 99, no. 24, p. 243601, 2007.

[47] O. Cohen, J. S. Lundeen, B. J. Smith, G. Puentes, P. J. Mosley, and I. A. Walmsley, "Tailored photon-pair generation in optical fibers," *Physical Review Letters*, vol. 102, no. 12, p. 123603, 2009.

[48] Y.-H. Kim and W. P. Grice, "Measurement of the spectral properties of the two-photon state generated via type II spontaneous parametric downconversion," *Optics Letters*, vol. 30, no. 8, pp. 908–910, 2005.

[49] W. Wasilewski, P. Wasylczyk, P. Kolenderski, K. Banaszek, and C. Radzewicz, "Joint spectrum of photon pairs measured by coincidence Fourier spectroscopy," *Optics Letters*, vol. 31, no. 8, pp. 1130–1132, 2006.

[50] H. S. Poh, C. Y. Lum, I. Marcikic, A. Lamas-Linares, and C. Kurtsiefer, "Joint spectrum mapping of polarization entanglement in spontaneous parametric down-conversion," *Physical Review A*, vol. 75, no. 4, p. 043816, 2007.

[51] M. Avenhaus, A. Eckstein, P. J. Mosley, and C. Silberhorn, "Fiber-assisted single-photon spectrograph," *Optics Letters*, vol. 34, no. 18, pp. 2873–2875, 2009.

[52] S.-Y. Baek and Y.-H. Kim, "Spectral properties of entangled photons generated via type-I frequency-nondegenerate spontaneous parametric down-conversion," *Physical Review A*, vol. 80, no. 3, p. 033814, 2009.

[53] A. Eckstein, G. Boucher, A. Lemaître, P. Filloux, I. Favero, G. Leo, J. E. Sipe, M. Liscidini, and S. Ducci, "High-resolution spectral characterization of two photon states via classical measurements," *Laser and Photonics Reviews*, vol. 8, no. 5, 2014.

[54] G. Harder, V. Ansari, B. Brecht, T. Dirmeier, C. Marquardt, and C. Silberhorn, "An optimized photon pair source for quantum circuits," *Optics Express*, vol. 21, no. 12, pp. 13 975–13 985, 2013.

[55] J. B. Spring, P. S. Salter, B. J. Metcalf, P. C. Humphreys, M. Moore, N. Thomas-Peter, M. Barbieri, X.-M. Jin, N. K. Langford, W. S. Kolthammer, M. J. Booth, and I. A. Walmsley, "On-chip low loss heralded source of pure single photons," *Optics Express*, vol. 21, no. 11, pp. 13 522–13 532, 2013.

[56] T. Lutz, P. Kolenderski, and T. Jennewein, "Demonstration of spectral correlation control in a source of polarization-entangled photon pairs at telecom wavelength," *Optics Letters*, vol. 39, no. 6, pp. 1481–1484, 2014.

[57] G. Patera, C. Navarrete-Benlloch, G. de Valcarcel, and C. Fabre, "Quantum coherent control of highly multipartite continuous-variable entangled states by tailoring parametric interactions," *The European Physical Journal D*, vol. 66, no. 9, 2012.

[58] A. U'Ren, C. Silberhorn, R. Erdmann, W. Grice, I. Walmsley, K. Banaszek, and M. Raymer, "Generation of pure-state single-photon wavepackets by conditional preparation based on spontaneous parametric downconversion," *Laser Physics*, vol. 15, p. 146, 2006.

[59] W. P. Grice, A. B. U'Ren, and I. A. Walmsley, "Eliminating frequency and space-time correlations in multiphoton states," *Physical Review A*, vol. 64, no. 6, p. 063815, 2001.

[60] S. M. Barnett and R. Loudon, "Sum rule for modified spontaneous emission rates," *Physical Review Letters*, vol. 77, no. 12, p. 2444, 1996.

[61] M. L. Cooper, G. Gupta, M. A. Schneider, W. M. Green, S. Assefa, F. Xia, Y. A. Vlasov, and S. Mookherjea, "Statistics of light transport in 235-ring silicon coupled-resonator optical waveguides," *Optics Express*, vol. 18, no. 25, pp. 26 505–26 516, 2010.

[62] J. B. Pors, S. S. R. Oemrawsingh, A. Aiello, M. P. van Exter, E. R. Eliel, G. W. 't Hooft, and J. P. Woerdman, "Shannon dimensionality of quantum channels and its application to photon entanglement," *Physical Review Letters*, vol. 101, p. 120502, 2008.

[63] J. R. Ong, R. Kumar, and S. Mookherjea, "Ultra-high-contrast and tunable-bandwidth filter using cascaded high-order silicon microring filters," *Photonics Technology Letters, IEEE*, vol. 25, no. 16, pp. 1543–1546, 2013.

[64] S. Miki, T. Yamashita, Z. Wang, and H. Terai, "A 64-pixel NbTiN superconducting nanowire single-photon detector array for spatially resolved photon detection," *Optics Express*, vol. 22, no. 7, pp. 7811–7820, 2014.

[65] "Princeton Lightwave 32 x 32 GmAPD Camera," http://www.princetonlightwave.com/mm-products/3d-ladar/gmapd-camera/.

[66] D. S. Biggs and M. Andrews, "Acceleration of iterative image restoration algorithms," *Applied Optics*, vol. 36, no. 8, pp. 1766–1775, 1997.

[67] J. Nunn, L. J. Wright, C. Söller, L. Zhang, I. A. Walmsley, and B. J. Smith, "Large-alphabet time-frequency entangled quantum key distribution by means of time-to-frequency conversion," *Optics Express*, vol. 21, no. 13, pp. 15 959–15 973, 2013.

[68] J. S. Bell, "On the Einstein-Podolsky-Rosen paradox," *Physics*, vol. 1, no. 3, pp. 195–200, 1964.

[69] J. Franson, "Bell inequality for position and time," *Physical Review Letters*, vol. 62, no. 19, p. 2205, 1989.

[70] P. Kwiat, A. Steinberg, and R. Chiao, "High-visibility interference in a Bell-inequality experiment for energy and time," *Physical Review A*, vol. 47, no. 4, p. R2472, 1993.

[71] R. Wakabayashi, M. Fujiwara, K.-i. Yoshino, Y. Nambu, M. Sasaki, and T. Aoki, "Time-bin entangled photon pair generation from Si micro-ring resonator," *Optics Express*, vol. 23, no. 2, pp. 1103–1113, 2015.

[72] J. Suo, S. Dong, W. Zhang, Y. Huang, and J. Peng, "Generation of hyper-entanglement on polarization and energy-time based on a silicon micro-ring cavity," *Optics Express*, vol. 23, no. 4, pp. 3985–3995, 2015.

[73] H. Takesue, N. Matsuda, E. Kuramochi, and M. Notomi, "Entangled photons from on-chip slow light," *Scientific Reports*, vol. 4, p. 3913, 2014.

[74] A. Tosi, M. Sanzaro, N. Calandri, A. Ruggeri, and F. Acerbi, "Low dark count rate and low timing jitter InGaAs/InP single-photon avalanche diode," in *44th European Conference on Solid State Device Research Conference (ESSDERC)*, Sept 2014, pp. 82–85.

[75] R. Kumar, J. R. Ong, J. Recchio, K. Srinivasan, and S. Mookherjea, "Spectrally multiplexed and tunable-wavelength photon pairs at 1.55 μm from a silicon coupled-resonator optical waveguide," *Optics Letters*, vol. 38, no. 16, pp. 2969–2971, 2013.

[76] N. Matsuda, H. Takesue, K. Shimizu, Y. Tokura, E. Kuramochi, and M. Notomi, "Slow light enhanced correlated photon pair generation in photonic-crystal coupled-resonator optical waveguides," *Optics Express*, vol. 21, no. 7, pp. 8596–8604, 2013.

[77] W. C. Jiang, X. Lu, J. Zhang, O. Painter, and Q. Lin, "Ultra-bright photon-pair generation on a silicon chip," in *Frontiers in Optics*, 2012, pp. FW6C–10.

[78] M. J. Collins, C. Xiong, I. H. Rey, T. D. Vo, J. He, S. Shahnia, C. Reardon, T. Krauss, M. Steel, A. S. Clark, and B. J. Eggleton, "Integrated spatial multiplexing of heralded single-photon sources," *Nature Communications*, vol. 4, p. 2582, 2013.

[79] J. F. Clauser and A. Shimony, "Bell's theorem. Experimental tests and implications," *Reports on Progress in Physics*, vol. 41, no. 12, p. 1881, 1978.

[80] R. T. Thew, S. Tanzilli, W. Tittel, H. Zbinden, and N. Gisin, "Experimental investigation of the robustness of partially entangled qubits over 11 km," *Physical Review A*, vol. 66, no. 6, p. 062304, 2002.

[81] R. Kumar, J. R. Ong, M. Savanier, and S. Mookherjea, "Controlling the spectrum of photons generated on a silicon nanophotonic chip," *Nature Communications*, vol. 5, p. 5489, 2014.

[82] D. Bonneau, G. J. Mendoza, J. L. OBrien, and M. G. Thompson, "Effect of loss on multiplexed single-photon sources," *New Journal of Physics*, vol. 17, no. 4, p. 043057, 2015.

[83] A. Yariv, "Universal relations for coupling of optical power between microresonators and dielectric waveguides," *Electronics Letters*, vol. 36, no. 4, pp. 321–322, 2000.

[84] J. Heebner, R. Grover, T. Ibrahim, and T. A. Ibrahim, *Optical microresonators: theory, fabrication, and applications*. Springer Science & Business Media, 2008.

[85] E. Dulkeith, F. Xia, L. Schares, W. M. Green, and Y. A. Vlasov, "Group index and group velocity dispersion in silicon-on-insulator photonic wires," *Optics Express*, vol. 14, no. 9, pp. 3853–3863, 2006.

[86] Y. Vlasov and S. McNab, "Losses in single-mode silicon-on-insulator strip waveguides and bends," *Optics Express*, vol. 12, no. 8, pp. 1622–1631, 2004.

[87] Y. Zhang, T. Baehr-Jones, R. Ding, T. Pinguet, Z. Xuan, and M. Hochberg, "Silicon multi-project wafer platforms for optoelectronic system integration," in *The 9th International Conference on Group IV Photonics (GFP)*, 2012.

[88] J. Niehusmann, A. Vörckel, P. H. Bolivar, T. Wahlbrink, W. Henschel, and H. Kurz, "Ultrahigh-quality-factor silicon-on-insulator microring resonator," *Optics Letters*, vol. 29, no. 24, pp. 2861–2863, 2004.

[89] L. G. Helt, M. Liscidini, and J. E. Sipe, "How does it scale? comparing quantum and classical nonlinear optical processes in integrated devices," *Journal of the Optical Society of America B*, vol. 29, no. 8, pp. 2199–2212, 2012.

[90] Y. Guo, W. Zhang, N. Lv, Q. Zhou, Y. Huang, and J. Peng, "The impact of nonlinear losses in the silicon micro-ring cavities on CW pumping correlated photon pair generation," *Optics Express*, vol. 22, no. 3, pp. 2620–2631, 2014.

[91] A. Tosi, A. Della Frera, A. B. Shehata, and C. Scarcella, "Fully programmable single-photon detection module for InGaAs/InP single-photon avalanche diodes with clean and sub-nanosecond gating transitions," *Review of Scientific Instruments*, vol. 83, no. 1, p. 013104, 2012.

[92] S. Azzini, D. Grassani, M. Galli, L. C. Andreani, M. Sorel, M. J. Strain, L. Helt, J. Sipe, M. Liscidini, and D. Bajoni, "From classical four-wave mixing to parametric fluorescence in silicon microring resonators," *Optics Letters*, vol. 37, no. 18, pp. 3807–3809, 2012.

[93] N. C. Harris, D. Grassani, A. Simbula, M. Pant, M. Galli, T. Baehr-Jones, M. Hochberg, D. Englund, D. Bajoni, and C. Galland, "Integrated source of spectrally filtered correlated photons for large-scale quantum photonic systems," *Physical Review X*, vol. 4, no. 4, p. 041047, 2014.

[94] J. Silverstone, R. Santagati, D. Bonneau, M. Strain, M. Sorel, J. O'Brien, and M. Thompson, "Qubit entanglement between ring-resonator photon-pair sources on a silicon chip," *Nature Communications*, vol. 6, 2015.

[95] C. M. Gentry, J. M. Shainline, M. T. Wade, M. J. Stevens, S. D. Dyer, X. Zeng, F. Pavanello, T. Gerrits, S. W. Nam, R. P. Mirin, and M. A. Popovic, "Quantum-correlated photon pairs generated in a commercial 45 nm complementary metal-oxide semiconductor microelectronic chip," *Optica*, vol. 2, no. 12, pp. 1065–1071, 2015.

[96] J. A. Cox, A. L. Lentine, D. C. Trotter, and A. L. Starbuck, "Control of integrated micro-resonator wavelength via balanced homodyne locking," *Optics Express*, vol. 22, no. 9, pp. 11 279–11 289, 2014.

[97] H. Park, A. W. Fang, R. Jones, O. Cohen, O. Raday, M. N. Sysak, M. J. Paniccia, and J. E. Bowers, "A hybrid AlGaInAs-silicon evanescent waveguide photodetector," *Optics Express*, vol. 15, no. 10, pp. 6044–6052, 2007.

[98] M. Geis, S. Spector, M. Grein, R. Schulein, J. Yoon, D. Lennon, S. Deneault, F. Gan, F. Kaertner, and T. Lyszczarz, "CMOS-compatible all-Si high-speed waveguide photodiodes with high responsivity in near-infrared communication band," *Photonics Technology Letters, IEEE*, vol. 19, no. 3, pp. 152–154, 2007.

[99] J. Doylend, P. Jessop, and A. Knights, "Silicon photonic resonator-enhanced defect-mediated photodiode for sub-bandgap detection," *Optics Express*, vol. 18, no. 14, pp. 14 671–14 678, 2010.

[100] S. Grillanda, M. Carminati, F. Morichetti, P. Ciccarella, A. Annoni, G. Ferrari, M. Strain, M. Sorel, M. Sampietro, and A. Melloni, "Non-invasive monitoring and control in silicon photonics using CMOS integrated electronics," *Optica*, vol. 1, no. 3, pp. 129–136, 2014.

[101] J. R. Ong, R. Kumar, R. Aguinaldo, and S. Mookherjea, "Efficient CW four-wave mixing in silicon-on-insulator micro-rings with active carrier removal," *Photonics Technology Letters, IEEE*, vol. 25, no. 17, pp. 1699–1702, 2013.

[102] G. Priem, P. Dumon, W. Bogaerts, D. Van Thourhout, G. Morthier, and R. Baets, "Optical bistability and pulsating behaviour in Silicon-On-Insulator ring resonator structures," *Optics Express*, vol. 13, no. 23, pp. 9623–9628, 2005.

[103] R. Alferness, U. Koren, L. Buhl, B. Miller, M. Young, T. Koch, G. Raybon, and C. Burrus, "Broadly tunable InGaAsP/InP laser based on a vertical coupler filter with 57-nm tuning range," *Applied Physics Letters*, vol. 60, no. 26, pp. 3209–3211, 1992.

[104] J. K. Poon and A. Yariv, "Active coupled-resonator optical waveguides. I. gain enhancement and noise," *Journal of the Optical Society of America B*, vol. 24, no. 9, pp. 2378–2388, 2007.

[105] A. Melloni, F. Morichetti, and M. Martinelli, "Four-wave mixing and wavelength conversion in coupled-resonator optical waveguides," *Journal of the Optical Society of America B*, vol. 25, no. 12, pp. C87–C97, 2008.